

# **INTRACRANIAL VESSEL WALL IMAGING AT 7.0 TESLA MRI**

**Anja G van der Kolk**

## **Intracranial vessel wall imaging at 7.0 tesla MRI**

PhD thesis, Utrecht University, The Netherlands

Copyright © AG van der Kolk, 2014

The copyright of the articles that have been published or accepted for publication has been transferred to the respective journals.

ISBN: xxx-xx-xxx-xxxx-x

Cover design: Gerda Roeleveld, Alexandra de Rotte and Roy Sanders

Lay-out: Roy Sanders

Printed by: Ipskamp Drukkers

# **INTRACRANIAL VESSEL WALL IMAGING AT 7.0 TESLA MRI**

**Beeldvorming van de intracraniële vaatwanden met 7.0-tesla-MRI**

(met een samenvatting in het Nederlands)

Proefschrift

ter verkrijging van de graad van doctor aan de Universiteit Utrecht op gezag van de rector magnificus, prof.dr. G.J. van der Zwaan, ingevolge het besluit van het college voor promoties in het openbaar te verdedigen op  
dinsdag 22 april 2014 des ochtends te 10.30 uur

door

**Anja Gwendolyn van der Kolk**

geboren op 4 november 1984 te Wageningen

Promotoren: Prof.dr. P.R. Luijten  
Prof.dr. W.P.Th.M. Mali

Copromotoren: Dr. J. Hendrikse  
Dr. J.J.M. Zwanenburg

This research was performed within the framework of CTMM, the Center for Translational Molecular Medicine ([www.ctmm.nl](http://www.ctmm.nl)), project PARISk (grant 01C-202), and supported by the Dutch Heart Foundation.

Financial support by the Dutch Heart Foundation for the publication of this thesis is gratefully acknowledged.

Additional financial support was generously provided by Philips Healthcare and Röntgen Stichting Utrecht.

**Brain, the final frontier...**

These are the voyages of the 7 tesla group  
Its continuing mission, to explore strange new pathology  
To seek out new contrasts and ever higher resolution  
To boldly go where no MRI scanner has gone before...



# CONTENTS

General introduction	9
----------------------	---

## Part 1 – 7T MRI of the brain

Chapter 1: Clinical potential of ultrahigh-field MRI in brain disease	21
---	----

## Part 2 – Intracranial vessel wall imaging at 7T MRI

Chapter 2: Intracranial vessel wall sequence development	57
--	----

Chapter 3: Whole-brain intracranial vessel wall sequences with different image contrasts	75
--	----

Chapter 4: Distribution & natural course of vessel wall lesions in patients with TIA and ischemic stroke	93
--	----

Chapter 5: Comparison of ultrahigh-resolution intracranial vessel wall images with histopathology	109
---	-----

## Part 3 – Safety aspects of 7T MRI

Chapter 6: Safety considerations for radiofrequency heating of peripheral arterial stents	131
---	-----

General discussion	151
--------------------	-----

Summary	161
---------	-----

Nederlandse samenvatting	165
--------------------------	-----

List of publications	169
----------------------	-----

Dankwoord	177
-----------	-----

Biography	183
-----------	-----



# **GENERAL INTRODUCTION**

---

Cerebral (arterial) ischemic stroke – an episode of neurological dysfunction caused by focal cerebral, spinal or retinal infarction<sup>1</sup> – is a major cause of disability and death in the world.<sup>2</sup> When we focus on the general mechanism of ischemic stroke, reversible (transient ischemic attack [TIA]) or irreversible (ischemic stroke) damage to the brain parenchyma occurs when a part of the brain is acutely refrained from blood, and thereby from oxygen and nutrients. A common mechanism underlying this acute lack of blood flow is (temporary) occlusion of the artery feeding that part of the brain. Acute cerebral arterial occlusion can have various causes, including external sources of (thrombo)emboli (hematologic or heart diseases, extracranial [carotid] atherosclerosis) as well as pathology of the intracranial vessel

**“...common mechanism underlying this acute lack of blood flow [to the brain] is (temporary) occlusion of the artery feeding that part of the brain...”**

wall itself (intracranial atherosclerosis, vasculitis). Based on clinical findings, laboratory- and imaging results, a final causal diagnosis is attempted to be made for each individual patient, most often using the TOAST (Trial of org

10172 in acute stroke treatment) classification system (**Table 1**)<sup>3</sup>.

Current clinical treatment options in the acute setting of an ischemic stroke are intravenous tissue plasminogen activator (tPA, ‘thrombolysis’) and endovascular intracranial clot removal, although only a subgroup of patients may be eligible for these treatment options.<sup>4, 5</sup> Long-term options are based on prevention of (recurrent) ischemic stroke. In this regard, an attempt is made to focus on the (probable or possible) cause of the acute arterial occlusion. (Lifelong) antithrombotic medication or oral anticoagulants and lipid-lowering medication are standard treatment for the majority of ischemic stroke patients, and are based on lowering the chance of developing subsequent (thrombo)emboli.<sup>6</sup> Common, more cause-specific treatment options include, among others, oral antiarrhythmic

**Table 1** TOAST classification system<sup>3</sup>

<b>Classification</b>	<b>Description</b>
Large-artery atherosclerosis	>50% stenosis / occlusion major intra- or extracranial brain artery or cortical branch artery, presumably due to atherosclerosis; no cardiac cause
Cardioembolism	Arterial occlusions, presumably due to an embolus arising in the heart
Small-artery occlusion	Lacunar ischemic stroke; no >50% stenosis or cardiac cause
Stroke of other determined etiology	Rare causes (nonatherosclerotic vasculopathies, hematologic diseases)
Stroke of undetermined etiology	No causal diagnosis possible

medication, and atherosclerotic plaque removal (endarterectomy) or endovascular stenting for carotid artery stenosis.<sup>6</sup> Therefore, determining the cause of ischemic stroke is important for subsequent (therapeutic) management of the individual patient.

### **Imaging the cause of ischemic stroke**

Although some specific causes of ischemic stroke can be identified using clinical findings, stroke risk factors and laboratory results (e.g., hematologic diseases), most will need additional imaging studies to be recognized as such. For this purpose, several imaging techniques are available. An electrocardiogram (ECG), transthoracic echocardiogram or transesophageal echocardiogram (atrial fibrillation, atrial thrombus) can be used to confirm or exclude a cardiac cause of embolism. Intra- and extracranial arteries can be assessed for >50% luminal stenosis or occlusion using (transcranial) ultrasound (US), computed tomography angiography (CTA), magnetic resonance angiography (MRA) or intra-arterial digital subtraction angiography (DSA). Furthermore, extracranial carotid atherosclerotic plaques can be assessed using MRI, enabling plaque characterization and identifying possible plaques with an increased risk of causing (recurrent) ischemic events ('vulnerable plaques' or culprit lesions with a thin fibrous cap and/or intraplaque hemorrhage).<sup>7</sup> CT or MRI of the brain parenchyma can show specific patterns of ischemia, favoring either pathology of the (intra- or extracranial) arterial vessel wall (cortical or large subcortical ischemic infarcts limited to one flow territory) or external sources of emboli (affecting multiple flow territories)<sup>3</sup>. Small lacunar infarcts in the deep gray matter are thought to be caused by atherosclerosis (lipohyalinosis) of the small perforating arteries. Infarcts at the border of different perfusion territories (borderzone infarcts) may be caused by a severe drop in perfusion pressure in patients with an arterial occlusion.

### **Intracranial atherosclerosis**

Intracranial atherosclerosis is one of the main causes of cerebral ischemic stroke<sup>8,9</sup>, which is reflected in several postmortem studies showing a high prevalence of atherosclerosis of the major intracranial arteries of the circle of Willis (CoW)<sup>10,11</sup>. More importantly, it is associated with a high risk of subsequent ischemic events. In the last decade, it has received less attention as a cause of ischemic stroke than other common causes like carotid artery stenosis, although recent large clinical trials in the USA (WASID, SAMMPRIS) have increased the awareness of the importance of intracranial atherosclerosis as a major cause of stroke, also in the Western world. From these clinical trials, aggressive medical management is currently the preferred treatment method.<sup>12,13</sup>

Before the results were known of these large clinical trials in the Western world, a blind eye was turned to intracranial atherosclerosis relative to the large amount of studies performed in patients with extracranial arterial disease. A reason for this might be that for extracranial carotid artery stenosis, carotid endarterectomy is a long-established surgical treatment option, and endovascular stenting procedures have been introduced in clinical practice more recently, with several clinical trials conducted in this area.<sup>14, 15</sup> For intracranial stenosis, comparable treatment options are not established that well<sup>6</sup>; therefore, the need for detailed information regarding the intracranial arterial status has gained less interest. Second, currently used conventional imaging techniques – US, CTA, MRA and intra-arterial DSA – provide information about the intracranial vessel wall in an indirect way, by visualizing the vessel *lumen* (lumenography)<sup>16, 17</sup> instead of the pathological vessel

**“...conventional imaging techniques [...] visualize the vessel *lumen* instead of the pathological vessel *wall* itself...”**

*wall* itself; therefore, intracranial plaques will only become visible when giving rise to luminal narrowing. From extracranial atherosclerosis it is known that, because of arterial remodeling, lumen diameter can be maintained

despite progressive wall thickening.<sup>16, 18, 19</sup> Lumenography-based methods may therefore underestimate the presence of intracranial arterial wall pathology<sup>16, 19-24</sup>, necessitating an imaging technique directly assessing the intracranial arterial vessel wall.

Due to its superior soft tissue contrast, MRI would be the most suitable technique for imaging the intracranial arterial vessel wall. Because of the superficial position of the common and internal carotid artery, direct vessel wall and atherosclerotic plaque imaging using MRI at these locations is more easily performed. The intracranial arteries are located further away from the skin surface, with the major arteries of the CoW just above the skull base, making it more difficult to directly assess vessel wall and plaque status. Also, their small diameter – ranging from 2-3 mm proximally to < 1 mm more distally – and varying orientation necessitate a high spatial resolution and the availability of 3-dimensional (3D) reconstructions. In order to meet these requirements, a high magnetic field strength of 3 or 7 tesla (T) will be necessary to provide a high enough signal-to-noise ratio (SNR). In the last few years, several research groups have attempted to image the intracranial vessel wall, initially using 1.5T to image the vessel wall (enhancement)<sup>25-29</sup>, and thereafter using 3T to visualize both healthy and diseased intracranial vessel walls<sup>30-34</sup>. These studies clearly showed abnormal intracranial vessel walls, but it proved difficult to depict the healthy vessel wall, mainly because of a lack of contrast with surrounding tissues and cerebrospinal fluid (CSF). Visualizing the healthy vessel wall, however, is

essential for differentiation between healthy and diseased vessel wall. Also, in these previously published studies, coverage was limited to the specific atherosclerotic lesion that had previously been identified using a lumenography technique. Therefore, smaller plaques not causing luminal stenosis may have been missed. Finally, these studies mainly used an MRI sequence with one image contrast weighting. The use of multiple image contrast weightings may be better for characterizing atherosclerotic plaques, similar to plaque characterization of the internal carotid artery, where the vulnerable plaque can be identified by means of characteristics assessable using several image contrast weightings.

**“...smaller plaques not causing luminal stenosis may have been missed...”**

### **IVI study & thesis outline**

In December 2009, the prospective case-control Intracranial Vessel wall Imaging (IVI) study commenced at the University Medical Center Utrecht (UMCU). The goal of this study was to develop an intracranial vessel wall sequence at 7T MRI, that can be applied *in vivo* in patients with recent cerebral ischemic events to assess the healthy intracranial vessel wall, and the presence (and characterization) of intracranial atherosclerosis. Within this study, a total of 50 patients with cerebral ischemic stroke of the anterior cerebral flow territory (supplied by the carotid artery) and 50 patients with a TIA of the anterior flow territory are being prospectively included. Until January 2014, a total of 40 patients with ischemic stroke and 30 patients with TIA have been included in this study. This thesis describes the technical developments of 7T vessel wall imaging that were the basis of the intracranial vessel wall imaging performed in the IVI study. These studies are truly translational with technical developments of a 7T intracranial vessel wall sequence, directly applied in patients with an ischemic stroke or TIA due to various causes, including intracranial atherosclerosis and vasculitis. In **Part 1 (Chapter 1)**, the rationale behind the use of 7T MRI for brain (vessel) imaging will be explained, as well as reviewing its current applications and possible future directions. **Part 2** describes the development of the first intracranial vessel wall sequence at 7T MRI (**Chapter 2**), as well as its improvement to include whole-brain scanning (**Chapter 3**); it evaluates the location and change over time of vessel wall lesions found in Chapter 2 and Chapter 3 (**Chapter 4**); and it shows a preliminary attempt at validating 7T vessel wall imaging with its gold standard, histology (**Chapter 5**). **Part 3 (Chapter 6)** will shed light on the safety aspects of using the 7T MRI scanner in patients in clinical practice. Finally, in the **General discussion**, an overview of all chapters will be given, as well as future prospects of intracranial vessel wall imaging.

## REFERENCE LIST

- (1) Sacco RL, Kasner SE, Broderick JP et al. An updated definition of stroke for the 21st century: a statement for healthcare professionals from the American Heart Association/American Stroke Association. *Stroke* 2013;44(7):2064-89.
- (2) Go AS, Mozaffarian D, Roger VL et al. Heart disease and stroke statistics--2013 update: a report from the American Heart Association. *Circulation* 2013;127(1):e6-e245.
- (3) Adams HP, Jr., Bendixen BH, Kappelle LJ et al. Classification of subtype of acute ischemic stroke. Definitions for use in a multicenter clinical trial. TOAST. Trial of org 10172 in acute stroke treatment. *Stroke* 1993;24(1):35-41.
- (4) Bivard A, Lin L, Parsons MW. Review of stroke thrombolytics. *J Stroke* 2013;15(2):90-8.
- (5) Tansy AP, Liebeskind DS. The goldilocks dilemma in acute ischemic stroke. *Front Neurol* 2013;4(164):1-3.
- (6) Furie KL, Kasner SE, Adams RJ et al. Guidelines for the prevention of stroke in patients with stroke or transient ischemic attack: a guideline for healthcare professionals from the american heart association/american stroke association. *Stroke* 2011;42(1):227-76.
- (7) den Hartog AG, Bovens SM, Koning W et al. Current status of clinical magnetic resonance imaging for plaque characterisation in patients with carotid artery stenosis. *Eur J Vasc Endovasc Surg* 2013;45(1):7-21.
- (8) Sacco RL, Kargman DE, Gu Q, Zamanillo MC. Race-ethnicity and determinants of intracranial atherosclerotic cerebral infarction. The Northern Manhattan Stroke Study. *Stroke* 1995;26(1):14-20.
- (9) Gorelick PB, Wong KS, Bae HJ, Pandey DK. Large artery intracranial occlusive disease: a large worldwide burden but a relatively neglected frontier. *Stroke* 2008;39(8):2396-9.
- (10) Mazighi M, Labreuche J, Gongora-Rivera F, Duyckaerts C, Hauw JJ, Amarenco P. Autopsy prevalence of intracranial atherosclerosis in patients with fatal stroke. *Stroke* 2008;39(4):1142-7.
- (11) Vink A, Schoneveld AH, Poppen M, de Kleijn DP, Borst C, Pasterkamp G. Morphometric and immunohistochemical characterization of the intimal layer throughout the arterial system of elderly humans. *J Anat* 2002;200(Pt 1):97-103.
- (12) Kasner SE, Lynn MJ, Chimowitz MI et al. Warfarin vs aspirin for symptomatic intracranial stenosis: subgroup analyses from WASID. *Neurology* 2006;67(7):1275-8.
- (13) Derdeyn CP, Chimowitz MI, Lynn MJ et al. Aggressive medical treatment with or without stenting in high-risk patients with intracranial artery stenosis (SAMMPRIS): the final results of a randomised trial. *Lancet*, published online before print October 25, 2013; doi: 10.1016/S0140-6736(13)62038-3.
- (14) Ederle J, Dobson J, Featherstone RL et al. Carotid artery stenting compared with endarterectomy in patients with symptomatic carotid stenosis (International Carotid Stenting Study): an interim analysis of a randomised controlled trial. *Lancet* 2010;375(9719):985-97.
- (15) Halliday A, Bulbulia R, Gray W et al. Status update and interim results from the asymptomatic carotid surgery trial-2 (ACST-2). *Eur J Vasc Endovasc Surg* 2013;46(5):510-8.

- (16) Bash S, Villablanca JP, Jahan R et al. Intracranial vascular stenosis and occlusive disease: evaluation with CT angiography, MR angiography, and digital subtraction angiography. *AJNR Am J Neuroradiol* 2005;26(5):1012-21.
- (17) Miyazawa N, Akiyama I, Yamagata Z. Analysis of incidence and risk factors for progression in patients with intracranial steno-occlusive lesions by serial magnetic resonance angiography. *Clin Neurol Neurosurg* 2007;109(8):680-5.
- (18) Glagov S, Weisenberg E, Zarins CK, Stankunavicius R, Kolettis GJ. Compensatory enlargement of human atherosclerotic coronary arteries. *N Engl J Med* 1987;316(22):1371-5.
- (19) Kiechl S, Willeit J. The natural course of atherosclerosis. Part II: vascular remodeling. Bruneck Study Group. *Arterioscler Thromb Vasc Biol* 1999;19(6):1491-8.
- (20) Stiel GM, Stiel LS, Schofer J, Donath K, Mathey DG. Impact of compensatory enlargement of atherosclerotic coronary arteries on angiographic assessment of coronary artery disease. *Circulation* 1989;80(6):1603-9.
- (21) Chimowitz MI, Lynn MJ, Howlett-Smith H et al. Comparison of warfarin and aspirin for symptomatic intracranial arterial stenosis. *N Engl J Med* 2005;352(13):1305-16.
- (22) Kasner SE, Chimowitz MI, Lynn MJ et al. Predictors of ischemic stroke in the territory of a symptomatic intracranial arterial stenosis. *Circulation* 2006;113(4):555-63.
- (23) Nguyen-Huynh MN, Wintermark M, English J et al. How accurate is CT angiography in evaluating intracranial atherosclerotic disease? *Stroke* 2008;39(4):1184-8.
- (24) Muhlenbruch G, Das M, Mommertz G et al. Comparison of dual-source CT angiography and MR angiography in preoperative evaluation of intra- and extracranial vessels: a pilot study. *Eur Radiol* 2010;20(2):469-76.
- (25) Aoki S, Hayashi N, Abe O et al. Radiation-induced arteritis: thickened wall with prominent enhancement on cranial MR images report of five cases and comparison with 18 cases of Moyamoya disease. *Radiology* 2002;223(3):683-8.
- (26) Aoki S, Shirouzu I, Sasaki Y et al. Enhancement of the intracranial arterial wall at MR imaging: relationship to cerebral atherosclerosis. *Radiology* 1995;194(2):477-81.
- (27) Lam WW, Wong KS, So NM, Yeung TK, Gao S. Plaque volume measurement by magnetic resonance imaging as an index of remodeling of middle cerebral artery: correlation with transcranial color Doppler and magnetic resonance angiography. *Cerebrovasc Dis* 2004;17(2-3):166-9.
- (28) Klein IF, Lavallee PC, Touboul PJ, Schouman-Claeys E, Amarenco P. In vivo middle cerebral artery plaque imaging by high-resolution MRI. *Neurology* 2006;67(2):327-9.
- (29) Kuker W, Gaertner S, Nagele T et al. Vessel wall contrast enhancement: a diagnostic sign of cerebral vasculitis. *Cerebrovasc Dis* 2008;26(1):23-9.
- (30) Niizuma K, Shimizu H, Takada S, Tominaga T. Middle cerebral artery plaque imaging using 3-tesla high-resolution MRI. *J Clin Neurosci* 2008;15(10):1137-41.

- (31) Swartz RH, Bhuta SS, Farb RI et al. Intracranial arterial wall imaging using high-resolution 3-tesla contrast-enhanced MRI. *Neurology* 2009;72(7):627-34.
- (32) Ryu CW, Jahng GH, Kim EJ, Choi WS, Yang DM. High resolution wall and lumen MRI of the middle cerebral arteries at 3 tesla. *Cerebrovasc Dis* 2009;27(5):433-42.
- (33) Li ML, Xu WH, Song L et al. Atherosclerosis of middle cerebral artery: evaluation with high-resolution MR imaging at 3T. *Atherosclerosis* 2009;204(2):447-52.
- (34) Xu WH, Li ML, Gao S et al. In vivo high-resolution MR imaging of symptomatic and asymptomatic middle cerebral artery atherosclerotic stenosis. *Atherosclerosis* 2010;212(2):507-11.





# Part 1

## 7T MRI OF THE BRAIN

---

**Adapted from:**

**Van der Kolk AG**, Hendrikse J, Luijten PR. *The clinical potential of ultrahigh-field MRI for anatomy, pathogenesis, diagnosis and treatment planning in brain disease.* Neuroimaging Clin N Am 2012;22(2):343-62, with permission.

# Chapter 1

## CLINICAL POTENTIAL OF ULTRAHIGH-FIELD MRI IN BRAIN DISEASE

---

Anja G van der Kolk, MD; Jeroen Hendrikse, MD PhD; Peter R Lijten, PhD

*From the Department of Radiology, University Medical Center Utrecht, The Netherlands*

# Key points

- » Main advantages of ultrahigh-field magnetic resonance imaging (MRI) of the brain:
  - Higher signal-to-noise ratio (SNR)
  - Higher contrast-to-noise ratio (CNR)
- » These features provide higher lesion conspicuity, higher spatial resolution, or faster imaging.
- » Insight into normal anatomy, pathogenesis, diagnosis, and treatment can be gained for various disease categories.
- » Considerations for choosing sequences for clinical application:
  - Pursue highest spatial resolution possible
  - Make use of new contrasts
  - $T_2^*$ -weighted imaging
  - Phase imaging
- » In a patient with suspected brain disease not seen on conventional MRI, and no contraindications, ultrahigh-field MRI can be considered.
- » Metallic implants are the most important limitation, hampering full application of ultrahigh-field MRI in the (acute) clinical setting.
- » (Neuro)radiologists should be trained for assessment of ultrahigh-field MR images.

## INTRODUCTION

Since the emergence of nuclear magnetic resonance in medicine in the 1908s, the technique has seen an evolution not surpassed by many other medical developments. From a field strength of less than 0.5 tesla (T) in the beginning, MRI has evolved technically to a widespread use of 3T magnetic resonance imaging (MRI) scanners in current clinical practice. There is abundant scientific literature on new sequences and applications of MRI for better diagnosis and treatment of patients. Although the larger randomized trials are mostly based on MRI data from more conventional field strengths like 1.5 and 3 tesla (T), there is a clear trend towards human MRI applications at higher and higher field strengths and the first studies at 11.7T can be expected shortly, something few in the past would have believed possible.<sup>1</sup>

With all these fascinating new developments within MRI, it is sometimes difficult to decipher what is still clinical MRI and what has gone beyond clinical medicine: what is, or will be clinically relevant,<sup>2,3</sup> and what is not? This question is important in modern (cost-contained) health care, if a decision has to be made whether to buy a new 1.5T or 3T MRI scanner or even to contemplate acquiring a human 7T platform. For optimal

**“...three main factors: signal-to-noise ratio (SNR), imaging speed and spatial resolution...”**

triaging of patients the question whether a 1.5T, 3T, or, if available, ultrahigh-field MRI scan would provide the best diagnostic information may become challenging. In an effort to give some suggestions and directions as to how to address ultrahigh-field MRI in the clinical setting, we review the current status and clinical applicability of ultrahigh-field MRI of the brain, after a brief technical description of ultrahigh-field MRI itself. In addition, we discuss what diagnostic areas are still relatively unexplored, although several clinical caveats exist. Because the brain is the primary target for ultrahigh-field MRI research, as well as the anatomical area most imaged with MRI in the clinical setting, we focus on imaging of the brain alone, and do not go into detail about ultrahigh-field imaging of other areas of the body. To keep this review compact and synoptic, our focus is on anatomic imaging of the brain rather than including the increased functional and physiologic imaging capabilities that come with increased field strength.

## ULTRAHIGH-FIELD MRI : WHAT IS IT ALL ABOUT?

There are three main factors to be considered that determine the design and applications of MRI: signal-to-noise ratio (SNR), imaging speed and spatial resolution. Changing one of these factors has an effect on the other two factors,

and vice versa. Within limits, one can modify these factors to make MRI sequences with specific advantages. For instance, when a high spatial resolution is desired, either a high SNR or a (very) long scanning time is needed. A short scanning time also requires a high SNR, because in a very short time as much signal as possible is wanted, preferably without additional noise. To get the most out of MRI, a high SNR is mandatory. This is one of the main reasons why ultrahigh-field MRI is so important, because SNR rises approximately linearly with field strength. For a certain contrast, for instance  $T_1$ , this increased SNR can be used to increase the spatial resolution, for identification of smaller pathologic lesions; to decrease scanning time, facilitating imaging of less stable patients and moving organs like the heart; or to attain better lesion conspicuousness.

Apart from a high SNR, a higher magnetic field strength also influences the relaxation times of tissues,  $T_1$  and  $T_2^*$  in particular.<sup>4,5</sup> When increasing from 1.5 to 7T, for instance, the  $T_1$  values for gray and white matter change from 1188 ms and 656 ms to 2132 ms and 1220 ms, respectively. These prolonged relaxation times however still allow for sufficient contrast between the gray and white matter of the brain.<sup>6</sup> They also make exquisite time-of-flight MR angiography (TOF-MRA) possible, with a high contrast-to-noise ratio (CNR). In TOF-MRA, tissues with static spins become saturated when excited several times by radiofrequency (RF) pulses within their  $T_1$  relaxation time. Moving spins, like in flowing blood, that enter the excited volume, have not been saturated yet and are excited for only a limited number of times (depending on the slab volume that was chosen). These spins result in a high signal on TOF-MRA. When the  $T_1$  of tissues becomes longer, like at ultrahigh field, the static spins relax less between pulses, resulting in a lower signal from the static spins (background) and better contrast between flowing blood and suppressed background.<sup>7</sup>

The shortening effects of the ultrahigh magnetic field on  $T_2^*$  relaxation (changes in  $T_2$  are not so pronounced) are derived from the increased magnetic susceptibility effects at higher field. The magnetic susceptibility of a tissue is inherent to that particular tissue, and is the way in which the tissue becomes magnetized when put into a magnetic field. The result is that these tissue-specific magnetic fields have effects on each other, so-called magnetic susceptibility effects, which cause faster tissue relaxation. These magnetic susceptibility effects scale linearly with magnetic field strength, and have both an advantage and a disadvantage. The disadvantage is that they cause more distortion of the local magnetic field in its surroundings, causing, for a given bandwidth, image distortions or local drop-outs as a result of dephasing. This distortion can be seen for instance near air-filled cavities like the sinuses, where the brain just next to the bone of these cavities becomes distorted and unrecognizable. The advantage is that these magnetic

susceptibility effects can be used for generating better tissue contrast. In particular, paramagnetic and diamagnetic substances, having a high magnetic susceptibility, stand out compared with the rest of the tissue. Examples of these substances are deoxyhemoglobin (veins), calcium (calcified tumors, atherosclerotic plaque), blood degradation products like hemosiderin (microbleeds) and iron depositions.

The increased susceptibility effects at ultrahigh-field MRI not only influence the relaxation times of tissues but at microscopic level they also cause increased phase shifts of the individual spins. These shifts can be visualized on so-called phase-images of gradient echo sequences. Although not routinely used on lower field strengths, because of the smaller phase shifts and subsequent small signal changes on phase images, at ultrahigh field these images show enhanced CNR between grey and white matter, for instance between white matter and deep grey nuclei.<sup>8,9</sup> In this way, phase images could pose a new kind of contrast for anatomic differentiation and diagnosis in many disease fields.

Because of the changed relaxation times of tissues, lower-field MRI sequences cannot be directly copied into ultrahigh-field MRI scanners without sometimes serious changes in the many different sequence parameters. For instance, until 2010 a normal fluid-attenuated inversion-recovery (FLAIR) sequence, which cannot be missed in daily clinical routine, was not even possible at ultrahigh magnetic field.<sup>10</sup> Only in the last couple of years have robust clinical sequences, like the already mentioned FLAIR but also standard  $T_1$ -weighted and  $T_2^*$ -weighted sequences,<sup>11,12</sup> been developed for ultrahigh-field MRI, anticipating the question for ultrahigh-field clinical MRI.

The advantages of higher SNR, higher spatial resolution, and changes in the relaxation times at ultrahigh field are discussed in the next sections, including reference to several studies that show the application of these advantages in both clinical and (to a lesser extent) preclinical practice.

## **ANATOMY AND PATHOGENESIS**

Although for clinicians the goal of imaging with MRI is diagnosing the patient's disease, and monitoring treatment and recurrence of this disease, a large area of research with ultrahigh-field MRI has focused on imaging normal anatomy and unraveling the pathogenesis of diseases. This research is not only important for our understanding of disease processes and their locations but can also give us insight into possible new screening protocols and treatment strategies. Specifically, in diseases in which the pathogenesis is not fully understood, or for which there is no effective treatment, ultrahigh-field MRI could make a difference, by acquiring highly detailed images with new contrasts.

## Anatomy

Visualizing the *in vivo* normal anatomy of the brain on MRI is almost as important as visualizing its disease: without an idea of normal structure, one cannot discern normal from pathologic brain. Ultrahigh-field MRI has been used in this field already since its emergence, mainly using the increased spatial resolution for imaging of the small anatomic details not seen on lower field strengths. Most research has been performed on the hippocampal architecture. As discussed later, the hippocampus plays a significant role in the pathogenesis of many disease processes, including dementia and epilepsy. Visualizing the hippocampal substructures could lead to faster diagnosis of these diseases, by early recognition of small pathologic changes.

**“...visualizing normal anatomy of the brain is almost as important as visualizing its disease: without an idea of normal structure, one cannot discern normal from pathology...”**

In 1999, it was already known that several lines of differing signal intensity could be seen on MR images of the hippocampus. Although at that time it was already speculated that these lines represented hippocampal substructures, Wiesmann and colleagues<sup>13</sup> were the first to compare ultrahigh-field MRI of postmortem human hippocampus at 7T with histology. These investigators confirmed that the lines seen on MRI represented different layers of the hippocampal structures.<sup>13</sup> After this discovery, many other investigators visualized the substructures of the hippocampus on different ultrahigh-field strengths, first by using postmortem human hippocampi and temporal lobe blocks with histology comparison,<sup>14, 15</sup> and later by imaging the hippocampus in healthy volunteers at 7T,<sup>16, 17</sup> resulting in a high-resolution computational atlas of the human hippocampus, derived from postmortem 9.4T images.<sup>18</sup> Although not directly useful in clinical practice, these studies form the backbone of current *in vivo* human hippocampal imaging in patients, by showing the possibility and imaging characteristics of ultrahigh-field MRI of the hippocampal area (**Figure 1**), and also by confirming these characteristics with histology, which is often not possible in clinical studies.

The hippocampal cortex and architecture are not the only cortex that has gained interest since the emergence of ultrahigh-field MRI. In 2002, Fatterpekar and colleagues<sup>19</sup> performed a 9.4T MRI study to depict the laminar cytoarchitecture of postmortem cortex specimens and correlated the acquired images with histologic sections. These investigators showed that ultrahigh-field MRI could detect the laminar pattern of the isocortex, allocortex and periallocortex, and suggested a future role for ultrahigh field in the identification of Brodmann areas of the cortex *in vivo*.<sup>19</sup>

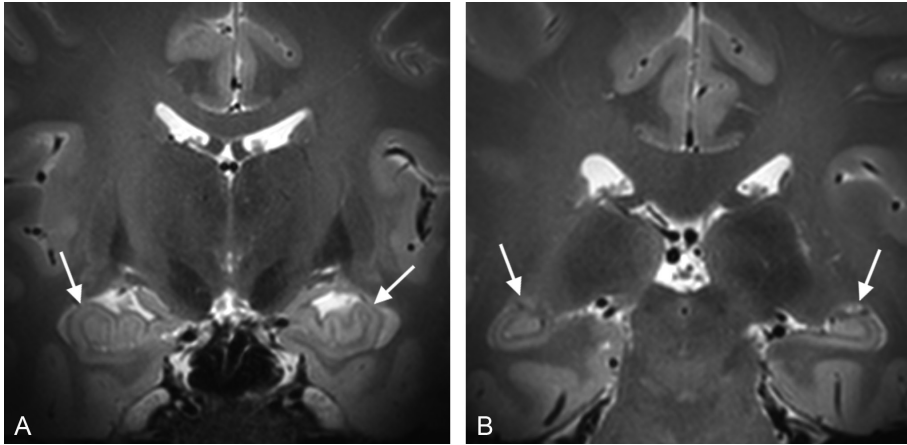


**Figure 1** Coronal 7T MR images of a 30-year-old volunteer showing the body (A) and tail (B) of the hippocampus. Several cortical and subcortical foldings of the hippocampal area can be seen (arrows in A and B), as well as cortical layers. Imaging parameters were repetition time 3158 ms; echo time 271 ms; turbo spin echo factor, 181; number of signal averages, 2; resolution  $0.6 \times 0.7 \times 0.7 \text{ mm}^3$ .

Next to cortical differentiation of small substructures of the hippocampus and cerebral cortex as a whole, another area where small anatomic details are sometimes effective is the arterial vessels. Specifically, the anatomy of the cerebral perforating (lenticulostriate) arteries has received some attention, because they have become associated with small vessel disease (SVD) and microbleeds.<sup>20</sup> The lenticulostriate arteries are the arteries penetrating and feeding the deep brain structures like the basal ganglia. The presence of lacunar infarcts in these areas is believed to be related to the pathologic state of these arteries (SVD). As with cortical disease, diseases of the lenticulostriate arteries can be detected only when imaging characteristics of the nondiseased arteries are known. Zwanenburg and colleagues<sup>21</sup> developed a magnetization-prepared anatomic reference MRA sequence to visualize both perforating arteries and related anatomy, and found its advantage over TOF-MRA in terms of visualizing possible correlation between vascular disease and tissue damage.<sup>21</sup> Cho and colleagues<sup>22</sup> and Kang and colleagues<sup>23</sup> also visualized and analyzed the lenticulostriate arteries with MRA at 7T in healthy volunteers. The results from these studies can be used for further studies investigating the role of diseased lenticulostriate arteries.

### **Pathogenesis**

Although they are sometimes difficult to distinguish, for clinical purposes it is important to recognize studies in which the main results are related to a better understanding of the pathogenesis (or pathophysiology) of disease and studies

in which the main results are (almost) directly applicable in clinical practice. We have tried to make this distinction in this section (about the first kind of studies) and the next section on diagnosis (about the second kind of studies); this does not mean that there is a clear line between the two kinds of studies, and others may classify studies differently. Because the main goal of this review is to create an understanding of the potential of ultrahigh-field MRI in the clinical setting, we believe this distinction is necessary.

### **Multiple sclerosis**

Multiple sclerosis (MS) is one of the best examples of an important, frequently seen disease of which the pathogenesis is still not fully understood. Affecting relatively young patients (20-30 years), this demyelinating disease has a major impact on patients' lives during a long period of time. The pathogenesis of MS is largely unknown, and there is no cure for the demyelinating process; treatment options are limited to medicinal drugs like  $\beta$ -interferon. Several MS lesion types have been found, with possibly different natural courses and therapeutic options.<sup>24</sup> Many studies have therefore used ultrahigh-field MRI to further elucidate the pathophysiologic processes underlying these MS lesions. Most studies have

**“...we have only just begun to image the true underlying process of demyelination...”**

focused on the characterization of only one type of MS lesion, cortical lesions, as a relatively new imaging entity in the pathogenesis of MS,<sup>25</sup> and have specifically tried, using these lesions, to visualize the pathophysiology of

MS *in vivo*. Kangarlu and colleagues<sup>26</sup> in 2007 described several cortical types of MS lesions, by using postmortem 1.5T and 8T MRI and histology comparison, and found that 8T ultrahigh-field MRI could detect more lesions than 1.5T MRI because of better SNR and CNR.<sup>26</sup> Hammond and colleagues<sup>27</sup> showed the heterogeneity in characteristics of MS lesions *in vivo* in 19 patients with MS and found suggestions of pathologic iron content in the basal ganglia; the appearance of peripheral phase rings, which could represent iron-rich macrophages seen at histology; and vessels penetrating MS lesions.<sup>27</sup> The vascular involvement within MS lesions was also found by Ge and colleagues<sup>28</sup> using *in vivo* 7T in two patients with MS, and by Tallantyre and colleagues<sup>29</sup> in 2008, who found that a central vessel (penetrating an MS lesions) was seen more often in perivascular lesions than other MS lesions. Pitt and colleagues<sup>30</sup> showed high accuracy for cortical lesion detection using postmortem  $T_2^*$ -weighted and white-matter-attenuated inversion-recovery  $T_1$ -weighted imaging at 7T. Laule and colleagues<sup>31</sup> measured myelin water fraction using a 32-echo  $T_2$  relaxation 7T experiment on postmortem specimens, visualizing

fine structures such as the myelination of deep cortical layers and the hippocampus.

These studies on the pathogenesis of MS in both postmortem MS specimens and *in vivo* in patients with MS show the heterogeneous imaging findings of the disease. Apart from different lesion types and variable vascular involvement, we have only just begun to image the true underlying process of demyelination. Although there is increasing evidence of a vascular pathogenesis in MS, mostly as a result of ultrahigh-field MRI, it is considered that we might be looking at differing pathogeneses within a heterogeneous disease group, called MS, instead of only one disease and one pathogenesis. The pathogenesis of MS will therefore remain a challenging topic for research into ultrahigh-field MRI.

### **Cerebrovascular diseases**

Most studies on the pathogenesis of cerebrovascular diseases have focused on the effects of hypertension on the brain, for instance altered arterial anatomy and function, thereby gaining insight into hypertension-based disease. Novak and colleagues<sup>32</sup> showed microangiopathy and iron deposits in an asymptomatic hypertensive patient at 8T, suggesting underlying pathogenic effects of hypertension even when patients do not have symptoms.<sup>32</sup> Kang and colleagues<sup>33</sup> also investigated the effect of hypertension on the lenticulostriate arteries (which have already been discussed in the section on anatomy) and showed that in hypertensive patients, the number of visible lenticulostriate arteries was smaller compared with healthy controls.<sup>33</sup> A case report by Biessels and colleagues<sup>34</sup> showed multiple microbleeds at 7T MRI in a patient with a hypertensive cerebral hemorrhage and visualized a direct relationship between some of the microbleeds and a small leaking penetrating artery.<sup>34</sup> The results of these studies show a variable pathophysiology of hypertension-based brain disease, in which microvasculature and microbleeds show a more or less prominent role. In an era when hypertension is a common risk factor for (cerebro)vascular disease, it is important to recognize the underlying pathogenic effects of hypertension in brain disease, not only for diagnostic imaging but also for treatment decisions (e.g., whether or not to treat hypertension aggressively even in asymptomatic patients).

Regarding microbleeds, next to a pathologic substrate of hypertension, they have also been associated with SVD. Imaging of microbleeds seems to depend on the spatial resolution and sensitivity to susceptibility effects of the applied magnetic field; for this reason, studies regarding microbleeds could benefit from ultrahigh field. Conijn and colleagues<sup>35</sup> in 2010 visualized microbleeds at 7T using a  $T_2^*$ -weighted double-echo sequence, and in 2011 found that microbleeds were more conspicuous at 7T than at 1.5T MRI.<sup>36</sup> Although much research has been carried out regarding microbleeds, real pathogenic studies are relatively lacking, which not

only questions what role these microbleeds play in cerebrovascular diseases but also if what we see as numerous hypointense spots are real microbleeds or other sources of a susceptibility effect.

Two studies have focused on ischemic infarcts as pathologic substrate of cerebrovascular diseases. One study by Chakeres and colleagues<sup>37</sup> studied the role of the microvasculature in lacunar infarcts in one patient with T<sub>2</sub>-weighted 8T MRI, compared with 1.5 Tesla MRI, for better characterization of small-vessel cerebrovascular disease associated with lacunar infarctions.<sup>37</sup> Jouvent and colleagues<sup>38</sup> recently studied postmortem specimens of a patient with CADASIL (cerebral autosomal-dominant arteriopathy with subcortical infarcts and leukoencephalopathy) at 7T and compared the results with histology. These investigators showed intracortical infarcts in this disease, and it is not known whether they are caused by different underlying mechanisms.<sup>38</sup> Ultrahigh-field MRI could provide additional pathogenic information currently not accessible by conventional imaging techniques.

### **Vascular malformations**

Of the different vascular malformations, venous cavernomas or cerebral cavernous malformations have gained most attention. Although often incidental findings and clinically silent, these vascular malformations can also present with acute neurologic deficits, hemorrhagic stroke, or seizures. Ultrahigh-field MRI has been used to characterize these malformations, by taking advantage of both the high spatial resolution that can be achieved and the increased susceptibility effects of blood products. Novak and colleagues<sup>39</sup> visualized a venous cavernoma *in vivo* at 8T MRI, compared with 1.5T MRI, and found that at ultrahigh field strength, the cavernoma appeared larger. This finding is of importance, because larger cavernomas tend to cause hemorrhage more often.<sup>39</sup> On the other hand, the greater susceptibility effect at ultrahigh field could have caused an enlargement effect not consistent with reality. Shenkar and colleagues<sup>40</sup> investigated the architecture of cerebral cavernous malformations by using 9.4T or 14.1T proton density-weighted, T<sub>1</sub>-weighted, T<sub>2</sub>-weighted, and T<sub>2</sub>\*-weighted MRI on excised lesions, and compared their results with histology. These investigators acquired more information regarding the biologic state of these lesions, like inflammation, angiogenesis, and production of new caverns in specific regions of the lesions.<sup>40</sup> Both studies give a glimpse of the pathogenesis of these sometimes clinically relevant but often overlooked malformations.

## CLINICAL APPLICATIONS

After an introduction of the varying research subfields in which imaging of the normal anatomy and pathogenesis of diseases have been the primary focus, we now turn to the more directly clinically driven fields of research. There are several disease groups in which ultrahigh-field MRI has already provided additional diagnostic information not previously seen well on lower, conventional MRI field strengths. These disease groups have in common a diagnostic gap of varying size when imaging is concerned. For instance, MS may sometimes be a difficult diagnosis, especially when presented at an older age, because its characteristic lesions on conventional MRI (hyperintense white matter lesions) can be found in many other diseases and aging. Alzheimer disease (AD) is histologically (postmortem) relatively well defined, characterized by senile plaques and amyloid- $\beta$  deposition, but using clinical MRI the *in vivo* diagnosis of dementia in general is still based on hippocampal atrophy, which is not always present in AD, especially in early-onset cases. Although classification of brain tumors has improved with the use of contrast-enhanced MRI, it is still difficult to distinguish between necrosis or tumor recurrence in treated glioblastoma multiforme, and often a biopsy is needed to differentiate between low-grade astrocytoma and gliomatosis cerebri, and between a lymphoma and a glioblastoma. Cryptogenic epilepsy, in which no pathologic cause can be found, still exists. These and other diseases are discussed in the following sections, in which a summary is given of research that has been carried out at ultrahigh field strength in an attempt to improve the diagnostic yield of imaging.

### MS

The typical MR image of a patient with MS is that of a characteristic distribution of hyperintense white matter lesions on the FLAIR sequence, predominantly periventricular around the upper convex of the lateral ventricles, some of them enhancing after contrast administration. Follow-up imaging shows changing lesions, some that enhanced at first no longer enhance, although new lesions have appeared. There are few evidence-based biomarkers that can be used to predict disease course and treatment effect. As seen in the pathogenesis section, there has been new evidence that not only white matter lesions but also cortical lesions are a hallmark for MS. Furthermore, a central vessel can be found in a high percentage of MS and may at an older age distinguish between vascular-based white matter lesions and MS lesions. Mainero and colleagues<sup>41</sup> characterized cortical lesion types at 7T MRI in 16 patients with MS, using  $T_2$ -weighted and  $T_2^*$ -weighted sequences, and compared these types of lesions in relation to clinical subtypes of MS. These investigators found that cortical MS pathology might prove a valuable tool in

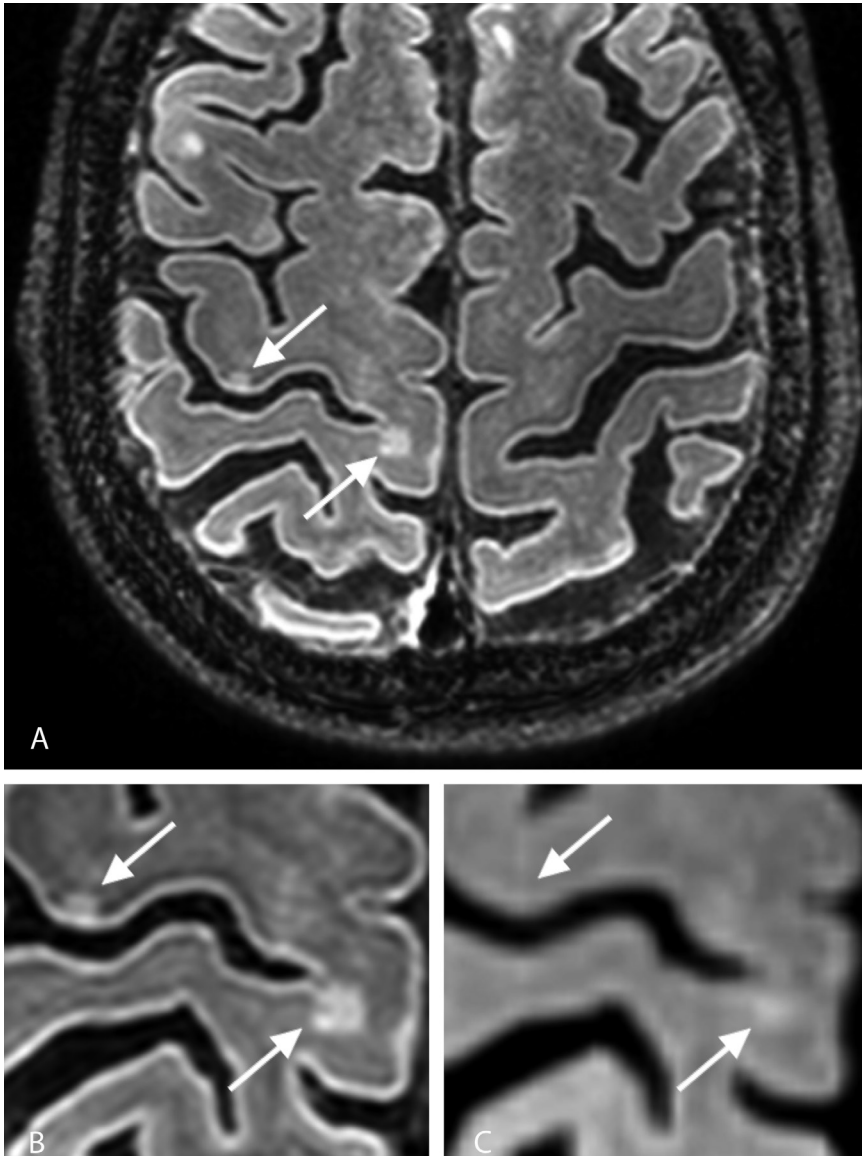


**Figure 2** 63-year-old woman with primary progressive MS with an expanded disability status Score of approximately 6.0. A 7T MRI scan was performed for detection of possible cortical lesions. (A) Axial overview and (B) zoomed-in image of a high parietal cortical MS lesion (*right arrow*) on axial 7T 3D FLAIR sequence. In retrospect, this lesion could also be seen on the 3T 3D FLAIR images, although with lower contrast-to-noise (C). On the other hand, the other cortical lesion (*left arrow*) could not be seen at 3T MRI. Imaging parameters: 7T 3D FLAIR as previously described<sup>10</sup>; 0.8 mm isotropic resolution; 3T FLAIR 1.1 mm isotropic resolution. (Courtesy of W.L. de Graaf, VUmc Amsterdam, the Netherlands. From van der Kolk AG, Hendrikse J, Zwanenburg JJ, et al. Clinical applications of 7T MRI in the brain. *Eur J Radiol* 2013;82(5):708-18; with permission.)

the assessment of the clinical course of MS.<sup>41</sup> Kollia and colleagues<sup>42</sup> also showed cortical lesions in patients with MS, which could be better visualized at 7T than at 1.5T, and found varying aspects of the lesions, confirming the observations of Hammond and colleagues.<sup>27</sup> Tallantyre and colleagues<sup>43</sup> focused on both imaging cortical lesions and imaging the distribution of central vessels within MS lesions.<sup>44</sup> These investigators found that cortical lesions were best detected when more than one imaging sequence was used, for instance 3T FLAIR and 7T magnetization-prepared rapid gradient-echo.<sup>43</sup> Furthermore, by using  $T_2^*$ -weighted imaging at 7T, they showed the potential of this sequence in discriminating lesions consistent with MS and caused by vascular disease.<sup>44</sup> Recently, Tallantyre and colleagues<sup>45</sup> developed this idea by showing that a perivenous location of lesions at 7T  $T_2^*$ -weighted imaging was predictive of the presence of demyelination, and therefore of MS, enabling discrimination between MS lesions and aging-related white matter lesions. As well as  $T_2^*$ -weighted imaging at ultrahigh field, several other imaging sequences were used by de Graaf and colleagues<sup>46</sup> to show the enhanced conspicuousness of cortical and subcortical MS lesions at ultrahigh field compared with 3T MRI, even without use of contrast agents. Recently, Schmierer and colleagues<sup>47</sup> opened up new diagnostic possibilities by showing, with  $T_2$ -weighted 9.4T MRI of postmortem MS specimens, that  $T_1$  may be a predictor of neuronal density and  $T_2$  a predictor of myelin content, when cortical gray matter was assessed quantitatively.

More detailed (also with regard to location) lesion visualization with ultrahigh-field MRI, specifically its association with intralesional vascular structures, could be of importance in the clinical diagnosis of MS. **Figure 2** shows two cortical MS lesions in a patient with MS.

### Cerebrovascular diseases

Two diseases have received most attention for diagnosis with ultrahigh-field MRI, more or less consistent with research performed mainly for pathogenic purposes: ischemic stroke and SVD. Novak and colleagues<sup>48</sup> imaged first one patient with hemorrhagic stroke and subsequently 17 patients<sup>49</sup> with ischemic stroke using both 1.5T and 8T MRI. These investigators showed great anatomic detail of the stroke areas at ultrahigh field and, more specifically, better visualization of microvessels than at lower field strength.<sup>48, 49</sup> Furthermore, additional ischemic infarcts and vascular diseases were found at ultrahigh field that were not apparent at 1.5T.<sup>49</sup> **Figure 3** and **Figure 4** show examples of small cortical and subcortical ischemic lesions in two clinical patients. Kang and colleagues<sup>50</sup> compared the number and configuration of lenticulostriate arteries between chronic stroke patients and healthy controls and found fewer arteries in the stroke group than

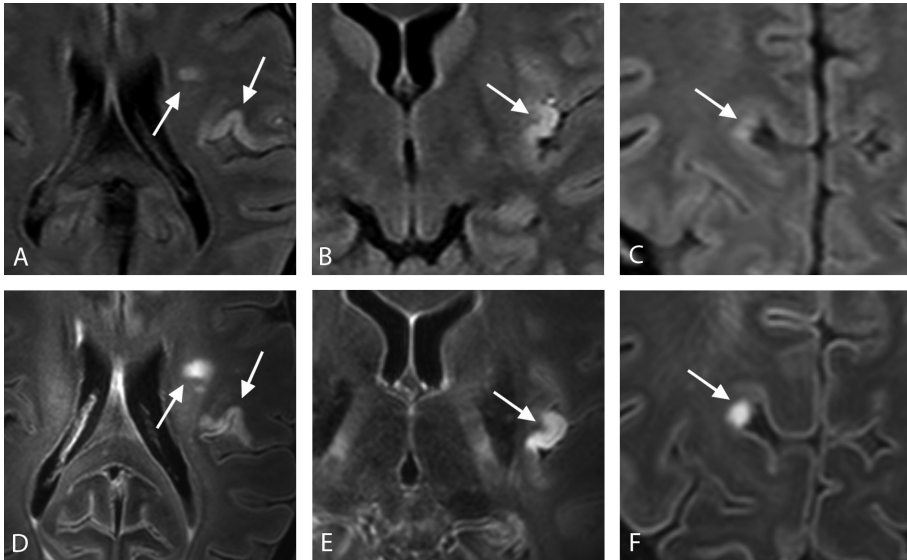


**Figure 3** 40-year-old woman with a history of systemic lupus erythematosus presented with thrombotic thrombocytopenic purpura complicated by transient motor dysphasia. (A-C) Axial standard clinical 1.5T and (D-F) corresponding 7T MRI FLAIR images, showing several small cortical and subcortical hyperintense ischemic lesions (*arrows*). Because of the higher CNR at 7T, lesions were more conspicuous than at lower field strength, and some were seen only in retrospect at 1.5T (*arrow* in C, compared with F). Imaging parameters as previously published<sup>10</sup>; 0.8 mm isotropic resolution. (From van der Kolk AG, Hendrikse J, Zwanenburg JJ, et al. Clinical applications of 7T MRI in the brain. *Eur J Radiol* 2013;82(5):708-18; with permission.)

the controls. Recent work by van der Kolk and colleagues<sup>51</sup> focused on visualizing the intracranial vessel wall itself (**Figure 5**) at 7T instead of lumen visualization, in patients with ischemic stroke or transient ischemic attack (TIA). These investigators found vessel wall lesions in several of these patients, even without causing luminal stenosis, suggesting a possible role of intracranial arterial disease in the diagnostic process and risk assessment of patients with cerebrovascular disease.<sup>51</sup> Based on these studies, ultrahigh-field MRI could play a role in better visualization of even small infarcts, making statements regarding overall vascular ischemic brain disease possible. Furthermore, visualization of lenticulostriate arteries and the intracranial arterial wall could play a role in diagnosing patients with (chronic) ischemic brain disease, like patients with low-grade carotid artery stenosis, silent (lacunar) infarcts, and multiple infarcts for which no cause has been found.

SVD can be diagnosed only indirectly, by identification of white matter lesions and lacunar infarcts, which are believed to be imaging markers for the presence and severity of disease of the small arterial vasculature.<sup>20</sup> As mentioned in the section on anatomy and pathogenesis, microbleeds and disease of the lenticulostriate

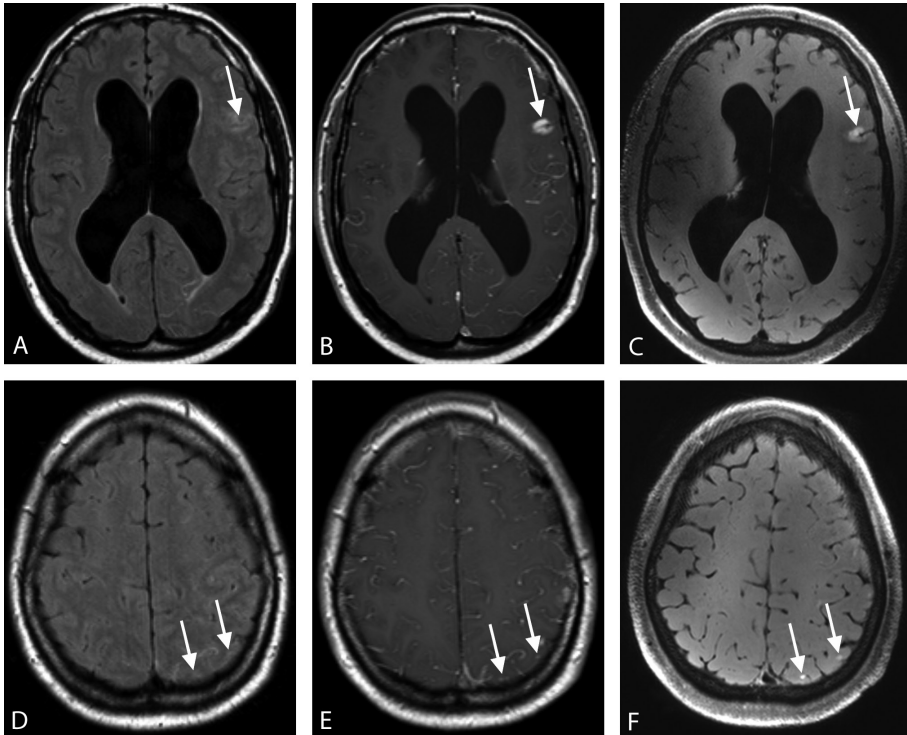


**Figure 4** 50-year-old man with a history of progressive dysphasia, suspected of primary or secondary (sarcoidosis) vasculitis. (A, D) Axial standard clinical 1.5T FLAIR, (B, E) corresponding standard 1.5T contrast-enhanced MRA, and (C, F) corresponding 7T MRI contrast-enhanced inversion-recovery turbo spin echo (TSE) images, showing a relatively large area of cortical enhancement frontoparietally (A-C), and several small occipital foci of subcortical enhancement (D-E), suggestive of small ischemic lesions (arrows). Because of the higher CNR at 7T also small ischemic lesions can be seen (F), which were not visible on the 1.5T MR images (D, E). Imaging parameters: 7T inversion-recovery TSE sequence; repetition time 3952 ms; echo time 38 ms; inversion time 1375 ms; TSE factor, 158; number of signal averages, 2; 0.8 mm isotropic resolution.

arteries have recently been associated with this heterogeneous disease. Only a few studies have investigated the diagnostic importance of these possible disease markers. Liem and colleagues<sup>52</sup> studied the luminal diameters of the lenticulostriate arteries at 7T TOF-MRA in patients with CADASIL and compared them with luminal diameters of healthy controls. These investigators found no difference in luminal diameter between patients with CADASIL and healthy volunteers.<sup>52</sup> Theysohn and colleagues<sup>53</sup> showed a higher sensitivity for detection of microbleeds at 7T compared with 1.5T, although detection of white matter lesions was comparable between the two field strengths. This finding suggests a possible role of ultrahigh-field MRI in the diagnostic workup of patients suspected of SVD. An example of microbleeds in a clinical patient at our institution can be found in **Figure 6**.

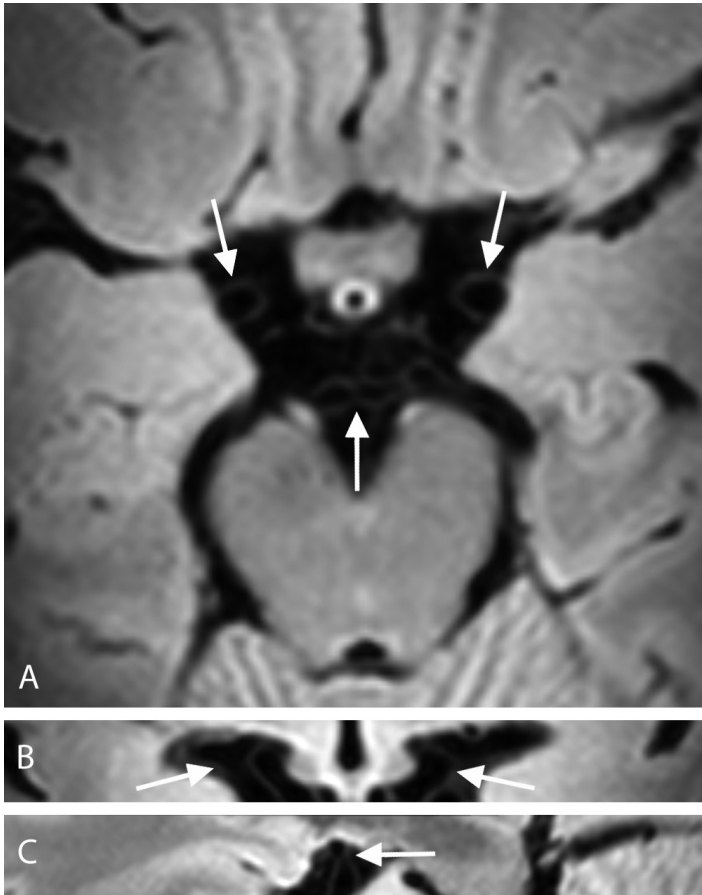


**Figure 5** 51-year-old man presented with transient paresis of the right arm and dysphasia, resolving after 1.5 hours based on a TIA of the left hemisphere. Standard 1.5T MRI revealed two small ischemic lesions on the diffusion-weighted images (not shown). (A) Axial, (B) coronal, and (C) sagittal magnetization-prepared inversion recovery turbo spin echo images, showing healthy intracranial arterial vessel wall of both distal internal carotid arteries (A and B, *upper arrows*), their bifurcation into middle and anterior cerebral artery (B and C, *arrows*), and both P1 segments of the posterior cerebral artery (A, *lower arrow*). Imaging parameters as previously published<sup>51</sup>, 0.8 mm isotropic resolution.

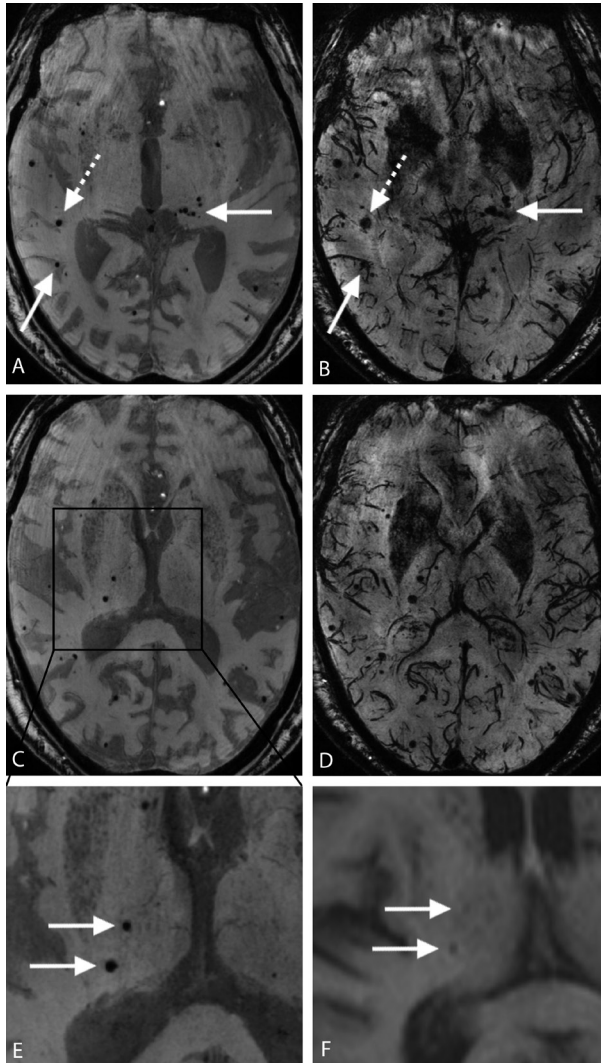


**Figure 6** 77-year-old man with a history of hypertension presented with transient dysphasia based on a TIA of the left hemisphere. (A, C) Axial minimal-intensity projections (minMIPs) over 10 mm thick volumes of the first and (B, D) minMIPs of the second echo of 7T  $T_2^*$ -weighted images, where multiple microbleeds can be found throughout the brain (arrows). Some are less easily distinguished on the second echo minMIPs because of overlapping venous structures (dashed arrows) and artifacts close to the nasal cavity. (E) Zoomed-in image of 7T and (F) of standard clinical 1.5T first echo minMIPs, showing better visualization of the microbleeds because of the increased susceptibility effects at 7T compared with 1.5T MRI. Imaging parameters as previously published<sup>35</sup>. (Courtesy of Dr M.M. Conijn, VUmc Amsterdam, the Netherlands. From van der Kolk AG, Hendrikse J, Zwanenburg JJ, et al. Clinical applications of 7T MRI in the brain. *Eur J Radiol* 2013;82(5):708-18 with permission.)

## Degenerative diseases

As mentioned earlier, most degenerative diseases like AD and Parkinson disease (PD) are histologically well defined, with clear tissue markers like senile plaques and amyloid- $\beta$  in AD and midbrain dopaminergic cell loss with Lewy bodies in PD. However, making a clinical diagnosis of these diseases based on imaging characteristics on MRI is still difficult, and one must rely on subjective and relatively nonspecific measurements of the hippocampal body, or changes in the signal intensity of the substantia nigra. An imaging technique that could visualize the real pathology underlying these degenerative diseases, or at least more specific characteristics currently unknown, would be of utmost clinical importance. Several studies have therefore used ultrahigh-field MRI in an attempt to develop the diagnostic process with regard to these prevalent diseases.

Most studies have used postmortem samples in their pursuit of new imaging markers. Dhenain and colleagues<sup>54</sup> investigated senile plaques in postmortem human AD specimens with 11.7T  $T_2^*$ -weighted MR imaging. These investigators hypothesized that the magnetic susceptibility of senile plaques would be different from that of the surrounding tissue, making them increasingly visible at higher

**“...an imaging technique that could visualize the real pathology underlying degenerative diseases would be of utmost clinical importance...”**

field strengths. They found that senile plaques could not be visualized in this way, suggesting a smaller (or absent) role of susceptibility effects in these plaques.<sup>54</sup> Van Rooden and colleagues<sup>55</sup> also used 7T  $T_2^*$ -weighted

imaging, alongside  $T_2$ -weighted imaging, for depiction of possible differences in cortical aspects of patients with cerebral amyloid deposition. Using human brain specimens with known amyloid- $\beta$  deposition, these investigators found that all specimens, when compared with healthy control specimens, showed hypointense foci or inhomogeneity of the cortex.<sup>55</sup> Kerchner and colleagues<sup>56</sup> showed, again with  $T_2^*$ -weighted imaging at 7T, that CA1 apical neuropil atrophy, a very early site of AD, could be visualized *in vivo* in 14 patients with AD. These studies suggest that  $T_2^*$ -weighted imaging at ultrahigh field could prove beneficial in the diagnosis of several degenerative diseases; however, much still has to be implemented *in vivo* before the technique can be applied clinically.

To our knowledge only two studies have focused on improving PD diagnosis, both within the last two years, so this is a relatively new field of research. Bajaj and colleagues<sup>57</sup> in 2010 used *in vivo*  $T_2^*$ -weighted 7T MRI to measure the relative magnetic susceptibility of the substantia nigra, specifically the pars compacta. These investigators found a difference in magnetic susceptibility of the pars compacta between patients with PD and healthy controls, suggesting an increase

in iron content.<sup>57</sup> Oh and colleagues<sup>58</sup> showed, by using a comparable imaging sequence at 7T, a difference in gross anatomic shape and quantitative so-called undulation values between patients with PD and healthy controls. These studies show two new imaging characteristics that seem to be specific for PD, possibly improving PD detection using MRI in clinical practice.

### **Brain tumors**

The current diagnosis of brain tumors is primarily based on MRI results before and after contrast administration, in which distinction of not only different types of tumors (meningioma vs astrocytoma) but also different grades (World Health Organization [WHO] grade II vs IV astrocytoma) can be made. However, a biopsy is often needed for the diagnosis and subsequent treatment. Furthermore, two of the most difficult diseases to discern regarding tumor treatment are tumor recurrence and necrotic tissue caused by radiation.

Several studies have tried to find new imaging markers to distinguish these different diseases with better precision, with the aim of making biopsy, with its concomitant risks, obsolete. Lupu and colleagues<sup>59</sup> used  $T_2^*$ -weighted imaging at 7T in 11 patients with heterogeneous brain tumors, revealing regions of calcification, microvessels and hemorrhage. These investigators suggested that these regions could provide better characterization of active or necrotic tumors.<sup>59</sup> Neovascularization is one of the hallmarks of high-grade astrocytomas, and imaging the microvasculature could help in distinguishing between low-grade and high-grade tumors, as well as in follow-up of treatment effect. Christoforidis and colleagues<sup>60, 61</sup> and Mönninghoff and colleagues<sup>62</sup> focused on visualizing this microvasculature in patients with astrocytomas of different WHO grades. Christoforidis and colleagues<sup>60</sup> found that  $T_2$ -weighted 8T MRI could identify regions of abnormal microvasculature in a glioblastoma multiforme, like tortuosity and enlargement, that were not visible with conventional techniques like 1.5T MRI or digital subtraction angiography. These investigators confirmed these foci of microvasculature seen on 8T MRI with histology.<sup>61</sup> Mönninghoff and colleagues<sup>62</sup> also found these results in 15 patients with astrocytoma when imaged with  $T_2^*$ -weighted 7T MRI, in whom necrosis was also visualized in more detail than at lower field strength. On the other hand, although more assumed microhemorrhages were seen at 7T MRI within brain metastases of bronchial carcinomas, Mönninghoff and colleagues<sup>63</sup> found the detection of metastases themselves at 7T equal to 1.5T MRI. Delineation of a more rare tumor, a dysplastic cerebellar gangliocytoma, with respect to morphology and microstructure has also been shown to be more conspicuous at ultrahigh-field MRI, especially using  $T_2^*$ -weighted imaging.<sup>64</sup> Regarding differentiation between low-grade and high-grade tumors, imaging of

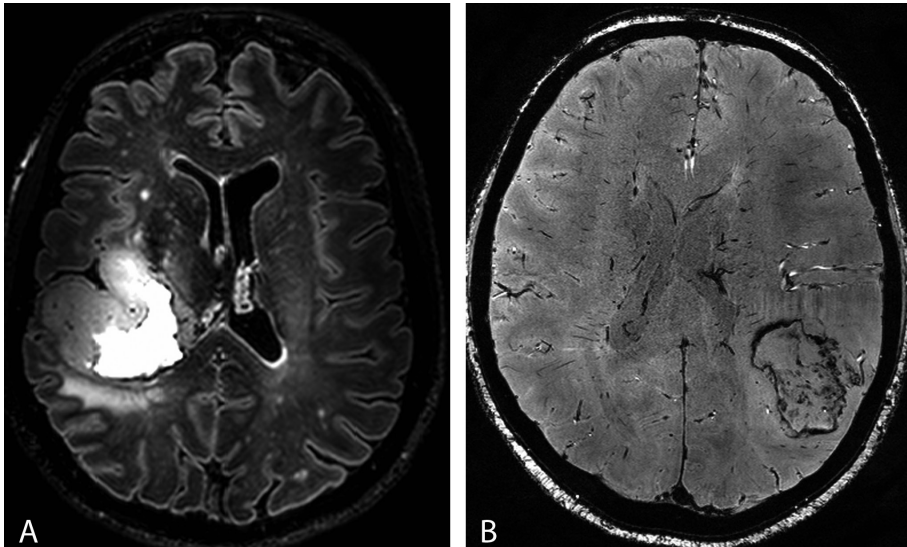


**Figure 7** Two patients with glioblastoma multiforme. (A) A 59-year-old woman presented with an epileptic seizure based on a right-sided, inhomogeneous enhancing temporoparietal glioblastoma multiforme. 7T MR FLAIR image shows described tumor with a central hyperintense area suggestive of necrosis, peritumoral edema, and a slight midline shift. Because of the high CNR at 7T, tumor as well as edema can clearly be distinguished from surrounding normal brain tissue. (B) Axial 7T  $T_2^*$ -weighted first echo image of a 62-year-old woman who presented with emotional and cognitive disturbances based on a left-sided parietal glioblastoma multiforme. The  $T_2^*$ -weighted image (B) shows an irregular lesion, the rim of the lesion showing a high susceptibility effect (hypointensity). Imaging parameters for 7T FLAIR sequence and  $T_2^*$ -weighted sequence as previously published<sup>10,11</sup>. (Courtesy of D.L. Polders and A.L.H.M.W. van Lier, UMC Utrecht, the Netherlands.)

the microvasculature of tumors using  $T_2$ -weighted or  $T_2^*$ -weighted ultrahigh-field MRI seems most promising. For differentiating between tumor recurrence and radiation necrosis, these sequences can also be used, as seen in one study, but studies on this topic are lacking. **Figure 7** gives two examples of tumor imaging at ultrahigh-field 7T MRI.

### Epilepsy

Cryptogenic epilepsies form a substantial amount of epilepsies in daily clinical practice. These epilepsies are believed to arise from brain lesions that are otherwise not found with the available imaging techniques. Because cryptogenic epilepsies can often be resistant to therapy, finding an imaging technique with which lesions not previously seen do appear (whether this may be because of a different energy metabolism or because of a small anatomic malformation), is important, especially when facing surgical treatment. Most studies on this topic have focused on known epilepsy-causing disease, like cavernous malformations and hippocampal sclerosis (HS), cryptogenic epilepsy (unknown cause), and for a more precise

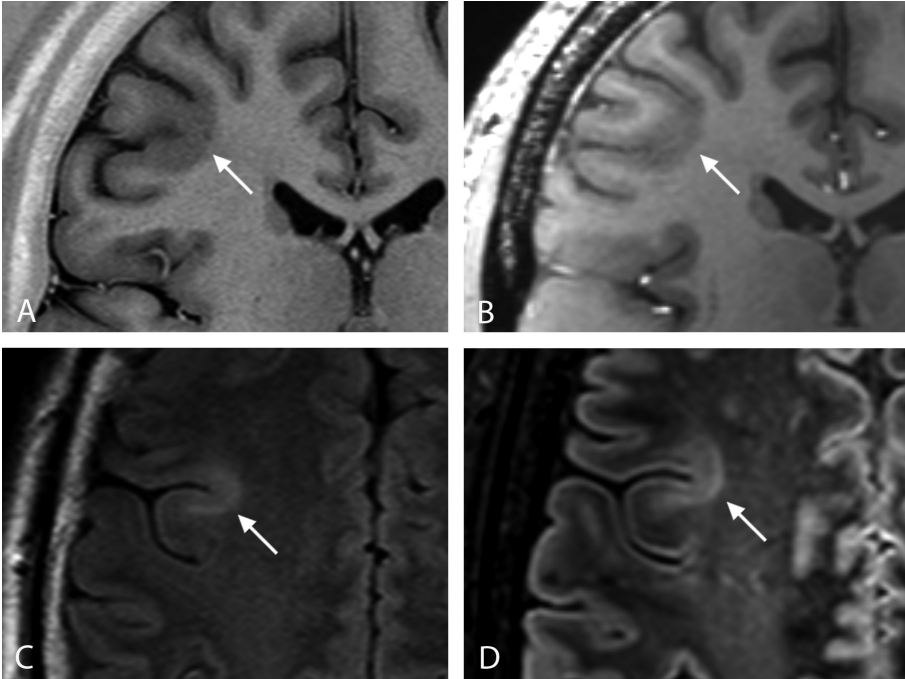


**Figure 8** A 32-year-old man presented with symptomatic therapy-resistant epilepsy characterized by recurrent partial secondary generalized seizures and recurrent status epilepticus. (A) Standard clinical 1.5T  $T_1$ -weighted and (C) FLAIR image, with corresponding images at 7T MRI (B, D). Both imaging sequences at both field strengths could visualize focal cortical dysplasia medially in the right frontal hemisphere (arrows in A-D). However, because of the higher image contrast at 7T, the focal lesion was more pronounced at the 7T FLAIR image (D). Imaging parameters of the 7T FLAIR sequence as previously published<sup>10</sup>; 7T  $T_1$ -weighted sequence: shot interval, 3500 ms; inversion time 1200 ms; repetition time 7.0 ms; echo time 2.9 ms; 0.8 mm isotropic resolution. (Courtesy of Dr C.H. Ferrier, UMC Utrecht, the Netherlands. From van der Kolk AG, Hendrikse J, Zwanenburg JJ, et al. Clinical applications of 7T MRI in the brain. *Eur J Radiol* 2013;82(5):708-18; with permission.)

localization of already known lesions (symptomatic epilepsies, **Figure 8**). Schlamann and colleagues<sup>65</sup> and Damman and colleagues<sup>66</sup> assessed cerebral cavernous malformations (cavernomas) with 7T  $T_2^*$ -weighted imaging and compared these results with images obtained at 1.5T. Schlamann and colleagues<sup>65</sup> assessed 10 patients with known cavernomas, found one additional lesion not seen on lower field strength, and concluded that ultrahigh-field MRI improved the detection of cavernomas, when using  $T_2^*$ -weighted imaging. Damman and colleagues<sup>66</sup> reviewed literature regarding the use of  $T_2^*$ -weighted imaging for cavernomas, and found, in their patient group, the same positive results as did Schlamann and colleagues<sup>65</sup>. Damman and colleagues<sup>66</sup> suggested that because of ultrahigh-field MRI, technical limitations of  $T_2^*$ -weighted imaging could be overcome, paving the way for clinical use of ultrahigh-field  $T_2^*$ -weighted MRI in diagnosing cavernomas.

Two other studies focused on HS associated with temporal lobe epilepsy. Breyer and colleagues<sup>67</sup> assessed the feasibility of multisequence 7T MRI for identification of HS in 6 patients in whom 1.5T had already confirmed HS. These investigators found that the increased susceptibility effects at ultrahigh-field strength increased the CNR within the hippocampus compared with lower field strength, making identification of more detailed structures possible, as well as excellent identification (on all sequences used) of HS.<sup>67</sup> Garbelli and colleagues<sup>68</sup> used surgical specimens of HS to investigate the correlation between ultrahigh-field T<sub>2</sub>-weighted MRI findings at 7T and histology. These investigators found a good correlation between abnormal cortical layering as seen on histology and MRI findings and suggested that ultrahigh field could detect minute intracortical abnormalities not seen at lower fields.<sup>68</sup> These results and those from the cavernoma studies indicate a role of primarily ultrahigh-field T<sub>2</sub>(\*)-weighted MRI in the diagnosis of epileptic lesions.

## TREATMENT PLANNING

This section discusses treatment applications of ultrahigh-field MRI. Treatment applications of MRI in general can be grossly subdivided into (novel) treatment monitoring, in which MRI is used as a diagnostic tool during the treatment course, identifying progression or regression of disease, and treatment planning, mostly localization-based, of which the most illustrative example is the use of MR datasets during neuronavigation-based surgery. High-intensity focused ultrasound, a relatively new noninvasive treatment modality, has to our knowledge not been used in combination with ultrahigh-field MRI, mostly because of its recent occurrence in the therapeutic field and the challenge of using this technique for intracranial disease. Because treatment monitoring is based on diagnosing in time, during the course of treatment, it can be deduced that all diagnostic applications of ultrahigh field reviewed in the section on diagnosis can also apply to monitoring treatment effects. Therefore we focus on the use of ultrahigh-field MRI in planning treatment (although the diagnostic applications reviewed earlier are also relevant).

To our knowledge, only a few studies at ultrahigh-field MRI have investigated its possible use specifically for treatment planning. Mönninghoff and colleagues<sup>69</sup> studied a vertebrobasilar aneurysm with 7T TOF-MRA. They found that ultrahigh-field TOF-MRA could not only identify the aneurysm with more precision but that vessel wall calcifications could also be identified using this sequence, as well as one of the posterior inferior cerebellar arteries arising from the aneurysm, not seen on lower field strength (see **Figure 9** for an example of a small branching artery of an aneurysm patient). These investigators concluded that these findings could help in aiding endovascular and surgical therapies.<sup>69</sup> Two other studies focused on

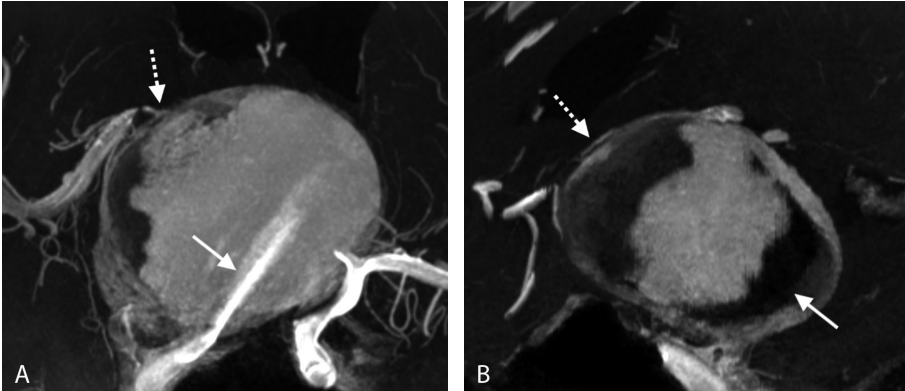


**Figure 9** A 16-year-old boy presented with progressive headache and transient monocular visual field defect based on a giant fusiform aneurysm of the distal internal carotid artery. (A) Coronal minimal-intensity projection over 10 mm thick volume and (B) sagittal image of 7T contrast-enhanced TOF-MRA, showing the giant aneurysm extending from the internal carotid artery. A contrast agent jet can be seen inside the aneurysm (arrow in A), as well as thrombosis of part of the aneurysm (arrow in B). The branching of the middle cerebral artery (dashed arrow in A) as well as of the anterior cerebral artery (dashed arrow in B) can be appreciated. Imaging parameters as previously published<sup>78</sup>; spatial resolution  $0.25 \times 0.30 \times 0.40 \text{ mm}^3$ , 60 mm slab, feet-head coverage 60 mm. (Courtesy of E.H.J. Voormolen, UMC Utrecht, the Netherlands.)

localizing with high precision anatomic structures used in deep brain stimulation in PD. Although most patients with PD are treated with dopamine (or analogous medication), surgical intervention in this disease has been introduced recently, and is already widely used to treat patients with advanced PD. The neurosurgical technique consists of placing a stimulating electrode within one of the target nuclei, like the subthalamic nucleus and globus pallidus, to relieve patient's symptoms, not only of PD, but also of tremor, chronic pain, and depression. The technique depends on placing the electrode at the exact location, which in turn depends on detailed visualization of the target nuclei. Two studies, by Rijkers and colleagues<sup>70</sup> and Cho and colleagues,<sup>71</sup> have used ultrahigh-field MRI for this purpose. Rijkers and colleagues<sup>70</sup> used 9.4T MRI on a postmortem human brain sample to obtain 3-dimensional (3D) reconstructions of the subthalamic nucleus and found a new reference point based on these detailed images, which might be used for targeting the nucleus. Cho and colleagues<sup>71</sup> used *in vivo* 7T MRI to visualize several targets for deep brain stimulation, like the subthalamic nucleus and internal globus pallidus, and compared their results with images obtained at 3T and 1.5T MRI, in both healthy volunteers and one patient with PD. These investigators found ultrahigh-field MRI to be superior in visualizing the stimulation targets compared with lower field strengths, mainly caused by significantly improved tissue contrast.

Based on these preliminary studies on applicability in treatment planning,

ultrahigh-field MRI could have a significant value in the visualization of anatomic structures important during surgery, like target nuclei and small arteries originating from aneurysms. However, this application could well be just the tip of the iceberg for clinical treatment applicability of ultrahigh field.

## LIMITATIONS IN CLINICAL USE

### Technical issues

As discussed earlier, a high magnetic field strength causes larger magnetic susceptibility effects for a given receiver bandwidth, resulting in signal drop-outs and distortion of images. Furthermore, a severe inhomogeneity in the applied transmit field (RF field) is seen at ultrahigh field. Because of this inhomogeneity, the pulse angle achieved varies between different locations in the brain, resulting in a spatially varying SNR.<sup>72</sup> More importantly for clinical imaging is that, depending

on the sequence used, it might lead to deviation of the contrast obtained from different locations in the image.<sup>7</sup>

For instance, when obtaining a  $T_1$ -weighted image, several areas of the brain will show on the image with a

**“...tip of the iceberg for clinical treatment applicability of ultrahigh field...”**

different contrast, sometimes even  $T_2$  contrast instead of  $T_1$  contrast. These effects are most pronounced in the cerebellum and the temporal lobes of the brain, which makes assessment of anatomy and disease in these areas more difficult. By developing improved pulse sequences and new hardware approaches, a more homogeneous transmit field might be attained, reducing the purely technical limitations to a minimum.

### Safety

Apart from causing spatially varying SNR,<sup>72</sup> the inhomogeneous transmit field mentioned earlier also causes specific absorption rate (SAR) restrictions. This finding is in addition to the global SAR (mean SAR over a certain volume) increase, which increases with the square of the applied magnetic field strength. Like SNR, the SAR is also less homogeneously distributed over the brain<sup>73</sup> because of the inhomogeneous transmit field, causing larger differences between areas and high SAR peaks at certain places. These increases in SAR impose stringent limitations on the duty cycle of applied sequences.

Metallic objects are currently a contraindication in the area of ultrahigh-field MRI. Apart from causing image distortions and artifacts for a given bandwidth, more than at lower field strengths, because of the larger susceptibility effects, potential

temperature effects in conducting implant material are another limitation for the use of ultrahigh-field MRI in clinical practice. Although these effects cause strict safety measures also at lower field strengths, at high field strength they may be more pronounced and, from a practical point of view, specific tests to determine safety at ultrahigh field are still in their infancy. Increased concern for safety at ultrahigh field is related to the shorter RF wavelength at higher field strength that matches more easily with metallic objects, possibly causing resonance and heating.<sup>7</sup> Although it is not clear what effect metallic implants have when they are placed in an ultrahigh magnetic field strength, because most studies on this topic have been performed on lower field strengths, safety precautions regarding imaging at 7T state that nothing metallic should enter the bore.<sup>7</sup>

It is easy to see the implications of these metallic safety precautions on the implementation of ultrahigh-field MRI in the clinical setting. Patients generally are older people who have had surgery, after which metallic implants are sometimes left behind. Examples are patients with atherosclerotic-related diseases, who often have clips or stents in the heart, lower extremity vessels or carotid arteries. Although sometimes surgical reports can be checked stating the implantation (or not) or metallic objects (and which metallic objects, and whether they have been tested for safety), in most patients this is not the case, and often patients themselves are not fully informed of the presence and location of metallic implants after surgery.

Even if older people have been healthy their whole lives, they often have dental implants that prohibit scanning at ultrahigh field. To illustrate this problem, in a recent study of patients with ischemic stroke and TIA, 173 of

**“...safety precautions regarding imaging at 7T state that nothing metallic should enter the bore...”**

611 eligible patients had to be excluded because of contraindications for 7T MRI caused by metallic implants (**Chapter 2**).<sup>51</sup> Furthermore, although young and healthy people could in theory readily be scanned at ultrahigh field, even in this group the increased use of (permanent) dental braces poses a challenge for implementing ultrahigh-field MRI in the clinical workup. Decreasing the list of contraindications is therefore mandatory if ultrahigh-field MRI is to be used in clinical practice (**Chapter 6**).

### **Learning curve for the radiologist**

It is not only a question of having the right techniques and sequences at hand, and overcoming limitations that are still hampering ultrahigh-field MRI from being implemented in clinical routine. With the new MRI contrasts and details found at ultrahigh-field MRI, radiologists should learn to interpret them. We cannot just assume that assessment of anatomy and disease at higher-field MR images will

be the same as on lower-field MRI. Ultrahigh-field images should be validated with known pathology as seen on lower field strengths like 1.5T or 3T MRI. With higher anatomic detail comes the chance of finding unexpected lesions, like very small aneurysms or developmental venous anomalies. Furthermore, new artifacts, related to the increased sensitivity for susceptibility and RF inhomogeneities present at ultrahigh-field MRI, can easily lead to false-positive findings. To get the best out of this new MRI application, radiologists need to be trained in assessing these new images.

## DISCUSSION

Using ultrahigh field has many advantages over lower field strengths, because of its higher achievable spatial resolution and increased susceptibility effects. These advantages enables us to see many things in different diseases that have not previously been seen on lower fields, as well as more detailed anatomic structures. However, how do we

**“...how do we know that what we see as disease is accurate?”**

know that what we see as disease is accurate? A few studies have tried to answer this question using postmortem specimens. Yao and colleagues<sup>74</sup> investigated the validity

of  $T_2^*$ -weighted contrast in the detection of iron and found that it was a valid indicator of iron content in iron-rich brain regions. On the other hand, de Reuck and colleagues<sup>75</sup> found that at 7T  $T_2^*$ -weighted imaging, in postmortem brain specimens of patients with dementia, only quantification of cerebral microbleeds in the corticosubcortical regions is reliable. This finding means that we have to be careful with diagnosing pathologic lesions, without having histologic comparison. This last issue can be a challenge, because opinions are varied regarding the use of fixed or non-fixed specimens for MRI and histology correlation. Dashner and colleagues<sup>76</sup> found unfixed specimens to show microvasculature better than fixed specimens, in which no vessels could be found at all. On the other hand, Garbelli and colleagues<sup>68</sup> showed superior MR contrast between cortical layers in completely fixed specimens compared with recently excised samples.

Furthermore, although there is a trend toward higher field strengths, with associated higher spatial resolution, even these ultrahigh-field techniques have a maximum resolution that can be realistically attained. For instance, using 8T MRI, visualization of deoxygenated small vessels was excellent down to a resolution of about 100 $\mu$ m, but these studies were performed using a human cadaver brain, and the question remains whether this high resolution can be achieved *in vivo*.<sup>77</sup> Also,

the additional value of ultrahigh-field MRI in diagnosis and treatment compared with lower field strengths has not been studied extensively.

However, regardless of these critical remarks, it is clear that ultrahigh-field MRI can improve diagnosis by finding disease that has not been found at lower field strengths. For example, in some patients with cryptogenic epilepsy (from our own clinical experience with 7T MRI), we do find lesions when we move to ultrahigh field. This application of ultrahigh-field MRI has such implications for these patients that it is too important to neglect. Another clinical example is that of patients with an aneurysm. One of the questions when planning surgery for an aneurysm is if there are any small branching arteries that arise from the aneurysm itself. If the aneurysm is clipped or coiled and a small important branching artery arises from the aneurysm, it is blocked from flow and can cause an ischemic infarct.

In current practice, ultrahigh-field MRI can officially be used only for clinical research purposes. When it becomes available for human clinical use, choosing sequences will in the beginning be at least partially dependent on which sequences are already available at ultrahigh-field MRI sites. Sequences should be successfully tested in healthy volunteers, so that any technical errors have already been dealt with. Furthermore, the sequences should not be long, because motion artifacts may reduce image quality. Most additional diagnostic value will probably be gained from using either high-resolution 3D sequences or  $T_2^*$ -weighted imaging. When different diseases are considered, it is clear that  $T_2^*$ -weighted imaging is most promising in degenerative diseases and epilepsy. FLAIR imaging has proved to be important in visualizing MS lesions, but can be used for all brain diseases, as is current clinical practice on lower magnetic fields.

## CLINICAL RECOMMENDATIONS

For clinical use, ultrahigh-field 7T MRI has (as a result of increased availability and a vast and increasing amount of clinical studies) the potential to be applied in various disease categories. Data have been obtained at 8 and even 9.4T as well, but these systems have primarily been focused on technological developments and *ex vivo* measurements (e.g. advanced functional MRI studies,  $^{23}\text{Na}$  brain imaging). Apart from unraveling pathogeneses of several disease entities that are not fully understood, like MS, advantages of ultrahigh-field MRI regarding diagnosis and treatment are gained in many cerebral diseases, like degenerative brain diseases, tumors, and epilepsy.

**“...advantages of ultrahigh-field MRI regarding diagnosis and treatment are gained in many cerebral diseases...”**

Choosing ultrahigh-field MRI for clinical diagnostics is dependent on several factors, like approximation of the added value of high-field MRI, the availability of ultrahigh-field sequences, and patient cooperation. Most sequences used at ultrahigh field for clinical diagnosis are sequences with a high spatial resolution, and contrast that is substantially more pronounced at ultrahigh-field strength, namely  $T_2^*$ -weighted and phase imaging. Apart from specific contraindications, ultrahigh-field MRI can be considered in any patient in whom a brain disease is suspected but not found on conventional MR imaging. To facilitate the dissemination of ultrahigh-field MRI in the high-end neuroradiology workflow, (neuro)radiologists should be trained to assess the sometimes distinctly different image contrasts obtained with otherwise conventional sequences.

#### **RECOMMENDED SEQUENCE CHART**

- » In general: high-resolution 3-dimensional (3D) imaging
- » Spatial resolution: < 1 mm isotropic voxels, with reconstructions in multiple directions
- » Specific valuable MRI sequences:
  - 3D fluid-attenuated inversion recovery (FLAIR)
  - 3D  $T_2^*$ -weighted sequences
  - 3D time-of-flight MR angiography (TOF-MRA)

## REFERENCE LIST

- (1) Vaughan T, DelaBarre L, Snyder C et al. 9.4T human MRI: preliminary results. *Magn Reson Med* 2006;56(6):1274-82.
- (2) Cha S, Gore JC. Clinical applications of ultra-high field 7T MRI - moving to FDA/EU approval. *Proc Intl Soc Mag Reson Med* 19 (2011), no abstract available.
- (3) Ladd ME, van Buchem MA, Rinck PA. Hot topics debate "Can 7T go clinical?". *Proc Intl Soc Mag Reson Med* 18 (2010), no abstract available.
- (4) Bottomley PA, Foster TH, Argersinger RE, Pfeifer LM. A review of normal tissue hydrogen NMR relaxation times and relaxation mechanisms from 1-100 MHz: dependence on tissue type, NMR frequency, temperature, species, excision, and age. *Med Phys* 1984;11(4):425-48.
- (5) Li TQ, Yao B, van Gelderen P et al Characterization of T(2)\* heterogeneity in human brain white matter. *Magn Reson Med* 2009;62(6):1652-7.
- (6) Rooney WD, Johnson G, Li X et al. Magnetic field and tissue dependencies of human brain longitudinal 1H<sub>2</sub>O relaxation in vivo. *Magn Reson Med* 2007;57(2):308-18.
- (7) van der Kolk AG, Hendrikse J, Zwanenburg JJ, Visser F, Luijten PR. Clinical applications of 7 tesla MRI in the brain. *Eur J Radiol* 2013;82(5):708-18.
- (8) Abduljalil AM, Schmalbrock P, Novak V, Chakeres DW. Enhanced gray and white matter contrast of phase susceptibility-weighted images in ultra-high-field magnetic resonance imaging. *J Magn Reson Imaging* 2003;18(3):284-90.
- (9) Budde J, Shajan G, Hoffmann J, Ugurbil K, Pohmann R. Human imaging at 9.4 T using T(2)\*-, phase-, and susceptibility-weighted contrast. *Magn Reson Med* 2011;65(2):544-50.
- (10) Visser F, Zwanenburg JJ, Hoogduin JM, Luijten PR. High-resolution magnetization-prepared 3D-FLAIR imaging at 7.0 tesla. *Magn Reson Med* 2010;64(1):194-202.
- (11) Zwanenburg JJ, Versluis MJ, Luijten PR, Petridou N. Fast high resolution whole brain T2\* weighted imaging using echo planar imaging at 7T. *Neuroimage* 2011;56(4):1902-7.
- (12) Van de Moortele PF, Auerbach EJ, Olman C, Yacoub E, Ugurbil K, Moeller S. T1 weighted brain images at 7 tesla unbiased for Proton Density, T2\* contrast and RF coil receive B1 sensitivity with simultaneous vessel visualization. *Neuroimage* 2009;46(2):432-46.
- (13) Wieshmann UC, Symms MR, Mottershead JP et al. Hippocampal layers on high resolution magnetic resonance images: real or imaginary? *J Anat* 1999;195(Pt1):131-5.
- (14) Chakeres DW, Whitaker CD, Dashner RA et al. High-resolution 8 tesla imaging of the formalin-fixed normal human hippocampus. *Clin Anat* 2005;18(2):88-91.
- (15) Augustinack JC, van der Kouwe AJ, Blackwell ML et al. Detection of entorhinal layer II using 7tesla [corrected] magnetic resonance imaging. *Ann Neurol* 2005;57(4):489-94.
- (16) Thomas BP, Welch EB, Niederhauser BD et al. High-resolution 7T MRI of the human hippocampus in vivo. *J Magn Reson Imaging* 2008;28(5):1266-72.

- (17) Theysohn JM, Kraff O, Maderwald S et al. The human hippocampus at 7 T—in vivo MRI. *Hippocampus* 2009;19(1):1-7.
- (18) Yushkevich PA, Avants BB, Pluta J et al. A high-resolution computational atlas of the human hippocampus from postmortem magnetic resonance imaging at 9.4 T. *Neuroimage* 2009;44(2):385-98.
- (19) Fatterpekar GM, Naidich TP, Delman BN et al. Cytoarchitecture of the human cerebral cortex: MR microscopy of excised specimens at 9.4 tesla. *AJNR Am J Neuroradiol* 2002;23(8):1313-21.
- (20) Wardlaw JM. Blood-brain barrier and cerebral small vessel disease. *J Neurol Sci* 2010;299(1-2):66-71.
- (21) Zwanenburg JJ, Hendrikse J, Takahara T, Visser F, Luijten PR. MR angiography of the cerebral perforating arteries with magnetization prepared anatomical reference at 7 T: comparison with time-of-flight. *J Magn Reson Imaging* 2008;28(6):1519-26.
- (22) Cho ZH, Kang CK, Han JY et al. Observation of the lenticulostriate arteries in the human brain in vivo using 7.0 T MR angiography. *Stroke* 2008;39(5):1604-6.
- (23) Kang CK, Park CW, Han JY et al. Imaging and analysis of lenticulostriate arteries using 7.0-tesla magnetic resonance angiography. *Magn Reson Med* 2009;61(1):136-44.
- (24) Lucchinetti C, Bruck W, Parisi J, Scheithauer B, Rodriguez M, Lassmann H. Heterogeneity of multiple sclerosis lesions: implications for the pathogenesis of demyelination. *Ann Neurol* 2000;47(6):707-17.
- (25) Rudick RA, Trapp BD. Gray-matter injury in multiple sclerosis. *N Engl J Med* 2009;361(15):1505-6.
- (26) Kangarlu A, Bourekas EC, Ray-Chaudhury A, Rammohan KW. Cerebral cortical lesions in multiple sclerosis detected by MR imaging at 8 tesla. *AJNR Am J Neuroradiol* 2007;28(2):262-6.
- (27) Hammond KE, Metcalf M, Carvajal L et al. Quantitative in vivo magnetic resonance imaging of multiple sclerosis at 7 tesla with sensitivity to iron. *Ann Neurol* 2008;64(6):707-13.
- (28) Ge Y, Zohrabian VM, Grossman RI. Seven-tesla magnetic resonance imaging: new vision of microvascular abnormalities in multiple sclerosis. *Arch Neurol* 2008;65(6):812-6.
- (29) Tallantyre EC, Brookes MJ, Dixon JE, Morgan PS, Evangelou N, Morris PG. Demonstrating the perivascular distribution of MS lesions in vivo with 7-tesla MRI. *Neurology* 2008;70(22):2076-8.
- (30) Pitt D, Boster A, Pei W et al. Imaging cortical lesions in multiple sclerosis with ultra-high-field magnetic resonance imaging. *Arch Neurol* 2010;67(7):812-8.
- (31) Laule C, Kozlowski P, Leung E, Li DK, Mackay AL, Moore GR. Myelin water imaging of multiple sclerosis at 7 T: correlations with histopathology. *Neuroimage* 2008;40(4):1575-80.
- (32) Novak V, Abduljalil A, Kangarlu A et al. Intracranial ossifications and microangiopathy at 8 tesla MRI. *Magn Reson Imaging* 2001;19(8):1133-7.
- (33) Kang CK, Park CA, Lee H et al. Hypertension correlates with lenticulostriate arteries visualized by 7T magnetic resonance angiography. *Hypertension* 2009;54(5):1050-6.
- (34) Biessels GJ, Zwanenburg JJ, Visser F, Frijns CJ, Luijten PR. Hypertensive cerebral hemorrhage: imaging the leak with 7-T MRI. *Neurology* 2010;75(6):572-3.
- (35) Conijn MM, Geerlings MI, Luijten PR et al. Visualization of cerebral microbleeds with dual-echo T2\*-weighted magnetic resonance imaging at 7.0 T. *J Magn Reson Imaging* 2010;32(1):52-9.

- (36) Conijn MM, Geerlings MI, Biessels GJ et al. Cerebral microbleeds on MR Imaging: comparison between 1.5 and 7T. *AJNR Am J Neuroradiol* 2011;32(6):1043-9.
- (37) Chakeres DW, Abduljalil AM, Novak P, Novak V. Comparison of 1.5 and 8 tesla high-resolution magnetic resonance imaging of lacunar infarcts. *J Comput Assist Tomogr* 2002;26(4):628-32.
- (38) Jouvent E, Poupon C, Gray F et al. Intracortical infarcts in small vessel disease: a combined 7-T postmortem MRI and neuropathological case study in cerebral autosomal-dominant arteriopathy with subcortical infarcts and leukoencephalopathy. *Stroke* 2011;42(3):e27-e30.
- (39) Novak V, Chowdhary A, Abduljalil A, Novak P, Chakeres D. Venous cavernoma at 8 tesla MRI. *Magn Reson Imaging* 2003;21(9):1087-9.
- (40) Shenkar R, Venkatasubramanian PN, Zhao JC, Batjer HH, Wyrwicz AM, Awad IA. Advanced magnetic resonance imaging of cerebral cavernous malformations: part I. High-field imaging of excised human lesions. *Neurosurgery* 2008;63(4):782-9.
- (41) Mainero C, Benner T, Radding A et al. In vivo imaging of cortical pathology in multiple sclerosis using ultra-high field MRI. *Neurology* 2009;73(12):941-8.
- (42) Kollia K, Maderwald S, Putzki N et al. First clinical study on ultra-high-field MR imaging in patients with multiple sclerosis: comparison of 1.5T and 7T. *AJNR Am J Neuroradiol* 2009;30(4):699-702.
- (43) Tallantyre EC, Morgan PS, Dixon JE et al. 3 tesla and 7 tesla MRI of multiple sclerosis cortical lesions. *J Magn Reson Imaging* 2010;32(4):971-7.
- (44) Tallantyre EC, Morgan PS, Dixon JE et al. A comparison of 3T and 7T in the detection of small parenchymal veins within MS lesions. *Invest Radiol* 2009;44(9):491-4.
- (45) Tallantyre EC, Dixon JE, Donaldson I et al. Ultra-high-field imaging distinguishes MS lesions from asymptomatic white matter lesions. *Neurology* 2011;76(6):534-9.
- (46) de Graaf WL, Visser F, Wattjes MP et al. 7 tesla 3D-FLAIR and 3D-DIR: high sensitivity in cortical regions in Multiple Sclerosis. *Proc Intl Soc Mag Reson Med* 18 (2010), abstract no. 409.
- (47) Schmierer K, Parkes HG, So PW et al. High field (9.4 tesla) magnetic resonance imaging of cortical grey matter lesions in multiple sclerosis. *Brain* 2010;133(Pt3):858-67.
- (48) Novak V, Kangarlu A, Abduljalil A et al. Ultra high field MRI at 8 tesla of subacute hemorrhagic stroke. *J Comput Assist Tomogr* 2001;25(3):431-5.
- (49) Novak V, Abduljalil AM, Novak P, Robitaille PM. High-resolution ultrahigh-field MRI of stroke. *Magn Reson Imaging* 2005;23(4):539-48.
- (50) Kang CK, Park CA, Park CW, Lee YB, Cho ZH, Kim YB. Lenticulostriate arteries in chronic stroke patients visualised by 7 T magnetic resonance angiography. *Int J Stroke* 2010;5(5):374-80.
- (51) van der Kolk AG, Zwanenburg JJ, Brundel M et al. Intracranial vessel wall imaging at 7.0 tesla MRI. *Stroke* 2011;42(9):2478-84.
- (52) Liem MK, van der Grond J, Versluis MJ et al. Lenticulostriate arterial lumina are normal in cerebral autosomal-dominant arteriopathy with subcortical infarcts and leukoencephalopathy: a high-field in vivo MRI study. *Stroke* 2010;41(12):2812-6.

## Part 1 – Chapter 1

- (53) Theysohn JM, Kraff O, Maderwald S et al. 7 tesla MRI of microbleeds and white matter lesions as seen in vascular dementia. *J Magn Reson Imaging* 2011;33(4):782-91.
- (54) Dhenain M, Privat N, Duyckaerts C, Jacobs RE. Senile plaques do not induce susceptibility effects in T2\*-weighted MR microscopic images. *NMR Biomed* 2002;15(3):197-203.
- (55) van Rooden S, Maat-Schieman ML, Nabuurs RJ et al. Cerebral amyloidosis: postmortem detection with human 7.0-T MR imaging system. *Radiology* 2009;253(3):788-96.
- (56) Kerchner GA, Hess CP, Hammond-Rosenbluth KE et al. Hippocampal CA1 apical neuropil atrophy in mild Alzheimer disease visualized with 7-T MRI. *Neurology* 2010;75(15):1381-7.
- (57) Bajaj N, Schafer A, Wharton S et al. PATH53 Magnetic susceptibility of substantia nigra in Parkinson's disease: a 7-T in vivo MRI study. *J Neurol Neurosurg Psychiatry* 2010;81(11):e22.
- (58) Oh SH, Kim JM, Park SY et al. Direct visualization of Parkinson's disease by in vivo human brain imaging using 7.0T MRI. *Proc Intl Soc Mag Reson Med* 19 (2011), abstract no. 421.
- (59) Lupo JM, Banerjee S, Hammond KE et al. GRAPPA-based susceptibility-weighted imaging of normal volunteers and patients with brain tumor at 7 T. *Magn Reson Imaging* 2009;27(4):480-8.
- (60) Christoforidis GA, Grecula JC, Newton HB et al. Visualization of microvasculature in glioblastoma multiforme with 8-T high-spatial-resolution MR imaging. *AJNR Am J Neuroradiol* 2002;23(9):1553-6.
- (61) Christoforidis GA, Kangarlu A, Abduljalil AM et al. Susceptibility-based imaging of glioblastoma microvasculature at 8 T: correlation of MR imaging and postmortem pathology. *AJNR Am J Neuroradiol* 2004;25(5):756-60.
- (62) Mönninghoff C, Maderwald S, Theysohn JM et al. Imaging of adult astrocytic brain tumours with 7 T MRI: preliminary results. *Eur Radiol* 2010;20(3):704-13.
- (63) Mönninghoff C, Maderwald S, Theysohn JM et al. Imaging of brain metastases of bronchial carcinomas with 7T MRI - initial results. *Rofo* 2010;182:764-72.
- (64) Mönninghoff C, Kraff O, Schlamann M, Ladd ME, Katsarava Z, Gizewski ER. Assessing a dysplastic cerebellar gangliocytoma (Lhermitte-Duclos disease) with 7T MR imaging. *Korean J Radiol* 2010;11(2):244-8.
- (65) Schlamann M, Maderwald S, Becker W et al. Cerebral cavernous hemangiomas at 7 tesla: initial experience. *Acad Radiol* 2010;17(1):3-6.
- (66) Dammann P, Barth M, Zhu Y et al. Susceptibility weighted magnetic resonance imaging of cerebral cavernous malformations: prospects, drawbacks, and first experience at ultra-high field strength (7-tesla) magnetic resonance imaging. *Neurosurg Focus* 2010;29(3):E5.
- (67) Breyer T, Wanke I, Maderwald S et al. Imaging of patients with hippocampal sclerosis at 7 tesla: initial results. *Acad Radiol* 2010;17(4):421-6.
- (68) Garbelli R, Zucca I, Milesi G et al. Combined 7-T MRI and histopathologic study of normal and dysplastic samples from patients with TLE. *Neurology* 2011;76(13):1177-85.
- (69) Mönninghoff C, Maderwald S, Wanke I. Pre-interventional assessment of a vertebrobasilar aneurysm with 7 tesla time-of-flight MR angiography. *Rofo* 2009 March 1;181(3):266-8.

- (70) Rijkers K, Temel Y, Visser-Vandewalle V et al. The microanatomical environment of the subthalamic nucleus. Technical note. *J Neurosurg* 2007;107(1):198-201.
- (71) Cho ZH, Min HK, Oh SH et al. Direct visualization of deep brain stimulation targets in Parkinson disease with the use of 7-tesla magnetic resonance imaging. *J Neurosurg* 2010;113(3):639-47.
- (72) Vaughan JT, Garwood M, Collins CM et al. 7T vs. 4T: RF power, homogeneity, and signal-to-noise comparison in head images. *Magn Reson Med* 2001;46(1):24-30.
- (73) Collins CM, Liu W, Wang J et al. Temperature and SAR calculations for a human head within volume and surface coils at 64 and 300 MHz. *J Magn Reson Imaging* 2004;19(5):650-6.
- (74) Yao B, Li TQ, Gelderen P, Shmueli K, de Zwart JA, Duyn JH. Susceptibility contrast in high field MRI of human brain as a function of tissue iron content. *Neuroimage* 2009;44(4):1259-66.
- (75) De Reuck J, Auger F, Cordonnier C et al. Comparison of 7.0-T T(2)\*-magnetic resonance imaging of cerebral bleeds in postmortem brain sections of Alzheimer patients with their neuropathological correlates. *Cerebrovasc Dis* 2011;31(5):511-7.
- (76) Dashner RA, Chakeres DW, Kangarlu A, Schmalbrock P, Christoforidis GA, DePhilip RM. MR imaging visualization of the cerebral microvasculature: a comparison of live and postmortem studies at 8 T. *AJNR Am J Neuroradiol* 2003;24(9):1881-4.
- (77) Dashner RA, Kangarlu A, Clark DL, Raychaudhury A, Chakeres DW. Limits of 8-tesla magnetic resonance imaging spatial resolution of the deoxygenated cerebral microvasculature. *J Magn Reson Imaging* 2004;19(3):303-7.
- (78) Hendrikse J, Zwanenburg JJ, Visser F, Takahara T, Luijten P. Noninvasive depiction of the lenticulostriate arteries with time-of-flight MR angiography at 7.0 T. *Cerebrovasc Dis* 2008;26(6):624-9.



# Part 2

## INTRACRANIAL VESSEL WALL IMAGING AT 7T MRI

---

**Adapted from:**

**Van der Kolk AG**, Hendrikse J, Brundel M, Biessels GJ, Smit EJ, Visser F, Lijten PR, Zwambag JJM. ***Multi-sequence whole-brain intracranial vessel wall imaging at 7.0 tesla.*** Eur Radiol 2013;23(11):2996-3004, with permission.

# Chapter 2

## INTRACRANIAL VESSEL WALL SEQUENCE DEVELOPMENT

---

Anja G van der Kolk, MD<sup>1</sup>; Jaco JM Zwanenburg, PhD<sup>1,2</sup>; Manon Brundel, MD<sup>3</sup>;  
Geert-Jan Biessels, MD PhD<sup>3</sup>; Fredy Visser<sup>1,4</sup>; Peter R Lijten, PhD<sup>1</sup>; Jeroen Hendrikse, MD PhD<sup>1</sup>

*From the <sup>1</sup>Department of Radiology, <sup>2</sup>Image Sciences Institute, and <sup>3</sup>Department of Neurology,  
University Medical Center Utrecht, The Netherlands; and <sup>4</sup>Philips Healthcare, Best, The Netherlands*

# Key points

- » Conventional imaging techniques provide *luminal* information on intracranial vessel *wall* pathology.
- » Because of intracranial arterial remodeling, these techniques possibly underestimate the presence of vessel wall disease.
- » The MPR-TSE sequence at 7T MRI can depict intracranial arterial vessel walls in healthy volunteers and patients:
  - Black blood techniques and CSF suppression enable good contrast between wall, blood and CSF
  - 0.8 mm isotropic voxels make reconstructions in every imaging plane possible
- » In 66% of patients with ischemic stroke or TIA, the MPR-TSE sequence showed  $\geq 1$  intracranial vessel wall lesion.
- » Only 27% of these lesions caused a stenosis on TOF-MRA.
- » The 3-dimensional 7T MPR-TSE sequence makes it possible to study the role of intracranial arterial wall pathology in more detail.

## INTRODUCTION

As discussed in the **General introduction** of this thesis, conventional lumenography techniques (intra-arterial digital subtraction angiography, magnetic resonance [MR] angiography) that visualize the vessel lumen may underestimate the presence of intracranial arterial pathology<sup>1-7</sup> because of arterial remodeling, by which lumen diameter can be maintained despite progressive wall thickening.<sup>8</sup> Second, using conventional MRI techniques, only pathological conditions, such as enhancement of the intracranial vessel wall with vasculitis, can be detected.<sup>9-12</sup> Recent studies at 3 tesla (T), using newly developed intracranial vessel wall MR sequences, clearly showed abnormal intracranial vessel walls; however, it proved difficult to depict the healthy vessel wall – necessary for differentiating healthy from diseased vessels –, mainly because of lack of contrast with surrounding tissues and cerebrospinal fluid (CSF).<sup>13-17</sup> In the study described in this chapter, an MRI method was developed to image the vessel wall of intracranial arteries, also in the absence of disease. The MRI sequence was developed at a magnetic field strength of 7T to allow for high-resolution imaging with sufficient sensitivity, and was tested in a pilot study with healthy volunteers and patients from the IVI study (**General introduction**), with an increased chance of having intracranial vessel wall pathology.

**“...conventional lumenography techniques that visualize the vessel lumen may underestimate the presence of intracranial arterial pathology...”**

## MATERIALS & METHODS

### Intracranial vessel wall sequence

Imaging was performed on a 7T whole-body MRI scanner (Philips Healthcare, Cleveland, OH, USA) with a 16-channel receive coil and volume transmit/receive coil for transmission (Nova Medical, Wilmington, MA, USA). We developed a volumetric (3-dimensional) inversion recovery turbo spin echo (TSE) sequence, in which the inversion pulse was used to null the CSF for contrast with the vessel wall. Black blood was obtained because of flow between excitation and refocusing in the TSE train. A dedicated refocusing train with low and varying refocusing pulse angles was applied. The pulse angles for the train were calculated according to the approach described by Busse and colleagues,<sup>18</sup> which is optimized to obtain a constant signal response during the readout train and, hence, a sharp point-spread function, with low refocusing angles. The angles were computed, given the echo-spacing of 4.7 ms and train length of 116 echoes, and using a  $T_1/T_2$  of 2500/50 ms, a minimum refocusing angle of 15 degrees, and a maximum angle of 90 degrees.

Low refocusing angles lead to a high flow sensitivity, which contributed to the black blood appearance. Furthermore, the low refocusing angles yielded a limited specific absorption rate of the refocusing train. Because of the varying orientation of the vessels and branches of the circle of Willis (CoW), isotropic voxels were used to ensure quality of vessel wall depiction independent of vessel orientation. Finally, to improve the signal-to-noise ratio of the vessel wall, magnetization preparation was applied before the inversion pulse, leading to saturation of tissues with short  $T_2$  compared to the  $T_2$  of CSF.<sup>19</sup> This yields saturation recovery instead of inversion recovery for these tissues and, hence, more signal at the moment of acquisition. For this magnetization preparation inversion recovery (MPIR) TSE sequence, the following scan parameters were used: field of view 220 x 180 x 13 mm<sup>3</sup> in transverse orientation, acquired resolution 0.8 x 0.8 x 0.8 mm<sup>3</sup> (0.5  $\mu$ L), echo train length (TSE factor) of 116 (including 4 startup cycles), repetition time 6050 ms, inversion time 1770 ms, echo time 23 ms, magnetization preparation mixing time 250 ms, no SENSE was applied, and 2 averages were acquired to avoid free induction decay (FID) artifacts. The scan duration was  $\approx$  12 minutes. For possible depiction of lesion activity, we administered 0.1 mL/kg of a gadolinium-containing contrast agent (Gadobutrol, Gadovist 1.0 mmol/mL, Bayer Schering Pharma, Newbury, UK) to all patients and obtained vessel wall information before and  $\approx$  5 minutes after contrast administration.

### **Angiography sequence**

For confirmation of the observed vessels seen on the MPIR-TSE images, a 3-dimensional (3D) time-of-flight MR angiography (TOF-MRA) by means of fast field echo sequence was added to the scan protocol with the following parameters: field of view 180 x 180 x 110 mm<sup>3</sup> in transverse orientation, acquired resolution 0.4 x 0.5 x 0.6 mm<sup>3</sup>, repetition time 22 ms, echo time 2.5 ms, flip angle 25 degrees, receiver bandwidth 202 Hz/pixel, and scan duration  $\approx$  10 minutes.

### **Offline processing & assessment**

MPIR-TSE images were analyzed on an offline workstation (Philips) by two observers who sought to identify the vessel walls of the major arteries of the CoW and its branches. The 3D format with isotropic resolution allowed multiple reformatting depending on local vessel orientation, which was used for assessment of both vessel wall and possible vessel wall lesions. TOF-MRA data were used to identify the observed vessels on the MPIR-TSE images. For assessment of contrast enhancement of the (local) vessel wall, the postcontrast MPIR-TSE scans were registered to the precontrast scans using rigid mutual information registration<sup>20</sup> with partial volume interpolation (32 bins, sampling factors  $x=4, y=4, z=1$ ). After coregistering,

precontrast and postcontrast registered images were subtracted to obtain only those areas with contrast enhancement. After obtaining the subtracted images, both precontrast and postcontrast scans as well as the subtracted images were put in a viewing format that allowed for direct comparison between enhancing areas and concomitant vessel wall anatomy. To see whether normal contrast enhancement had taken place, the infundibulum was assessed for enhancement on the subtracted images.

### **Study population**

Our sequence was tested on healthy volunteers and patients with a high chance of intracranial vessel wall pathology. This prospective study was approved by the Institutional Review Board of our hospital. All subjects gave written informed consent. Healthy volunteers without known cardiovascular disease were recruited by advertisement posters in our hospital in November and December 2009. Hereafter, all consecutive patients presenting with arterial ischemic stroke or transient ischemic attack (TIA) of the anterior cerebral circulation at the neurology ward of our hospital between December 2009 and January 2011 were screened for inclusion in the present study (IVI study, see **General introduction**). Patients who were unable to endure the MRI examination because of their clinical condition, healthy volunteers and patients with contraindications for 7T MRI (claustrophobia, metal objects in or on the body), and patients with a known allergic reaction to gadolinium-containing contrast agents or impaired renal function were excluded.

## **RESULTS**

### **Volunteer studies**

Seven healthy volunteers (three males; mean age, 30 years; range, 20-55 years) without known cardiovascular disease were included in the study and scanned with the MPR-TSE sequence. Vessel wall of the distal internal cerebral artery (ICA), basilar artery, M1 segment of the middle cerebral artery (MCA), A1 segment of the anterior cerebral artery (ACA), and P1 segment of the posterior cerebral artery (PCA) could be visualized along their complete trajectories in all volunteers (**Figure 1**). Also, in most subjects the vessel wall of the smaller A2, M2, and P2 branches of the ACA, MCA, and PCA, respectively, could be identified and tracked along their course on the MPR-TSE images. It was difficult to distinguish the vessel wall of these smaller branches when it was immediately adjacent to brain parenchyma (**Figure 1**). The quality of the vessel wall depiction was independent of the vessel orientation. No signs of gross artifacts from insufficient flow spoiling within the TSE train were observed.

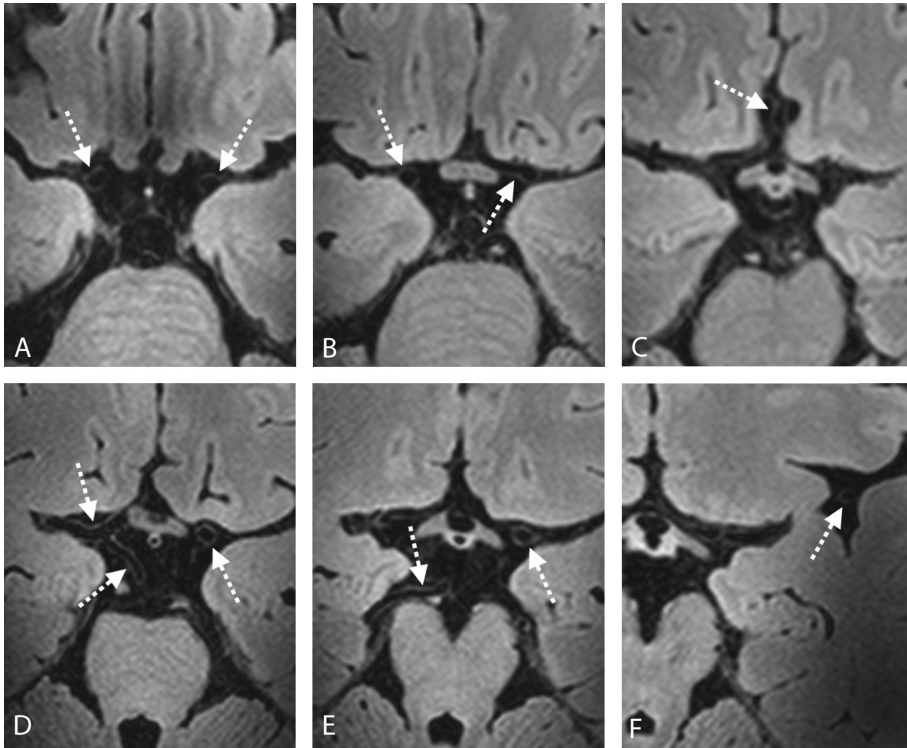


**Figure 1** Healthy volunteers, representative transverse 3-dimensional magnetization preparation inversion recovery (MPIR) turbo spin echo (TSE) images. (A-C) 26-year-old woman; vessel wall of left and right distal internal carotid artery (ICA; *dashed arrows* in A), right middle cerebral artery (MCA; left *dashed arrow* in B), left proximal anterior cerebral artery (ACA; right *dashed arrow* in B), and of right proximal ACA (*dashed arrow* in C) can be seen. (D-F) 55-year-old man; vessel wall of middle cerebral artery - ACA bifurcation (upper left *dashed arrow* in D) and posterior communicating artery (lower left *dashed arrow* in D) can be seen, as well as vessel wall of left distal ICA (right *dashed arrow* in D and E), right proximal posterior cerebral artery (PCA; left *dashed arrow* in E), and M2 segment of the MCA (*dashed arrow* in F).

### Patient studies

Between December 2009 and January 2011, 344 patients with ischemic infarct and 267 patients with TIA of the anterior cerebral circulation were admitted to our hospital, of whom 173 patients were excluded because of MRI contraindications and 226 patients were excluded because of their clinical status. In total, 35 patients (18 men; mean age, 59 years; range, 26-83 years) were included in the study, of whom 16 had experienced an acute ischemic stroke and 19 patients had experienced a TIA. All patients were scanned within one week after symptom onset. In six patients (17%) an underlying pathology other than atherosclerosis was diagnosed clinically (Moyamoya disease, reversible vasoconstriction syndrome, other vasculopathy of unknown cause, fibromuscular dysplasia, ICA dissection [twice]). In four patients

no cause for TIA or stroke was found. In three patients vessel wall MRI examinations were of insufficient quality for vessel wall assessment because of motion artifacts.

Of the 32 remaining patients in whom vessel wall could be assessed, 21 had identifiable vessel wall lesions on the MPIR-TSE sequence in major intracranial arteries (ACA, MCA, or PCA with their respective major branches; **Table**), 10 of the 17 TIA patients (59%) and 11 of the 15 stroke patients (73%). Seven of these twenty-one patients had only one vessel wall lesion; in the remaining fourteen patients, intracranial lesions were detected at multiple locations (**Table**); in four patients two lesions were found, five patients showed three lesions, and in five patients > three lesions were found, totaling 52 lesions. Lesions most often consisted of a small focal or more elongated thickening of the arterial vessel wall (**Figure 2**), sometimes of the whole vessel circumference, and causing luminal stenosis as seen on conventional imaging (time-of-flight MRA) in only 14 of 52 lesions (**Figure 3** and **Figure 4**).

Image subtractions from precontrast and postcontrast MPIR-TSE scans showed enhancement in 11 of the 52 locations of an intracranial lesion (**Table**, **Figure 4**, **Figure 5** and **Figure 6**). In 14 of the 21 patients with an intracranial lesion, a lesion was present in an artery of the flow territory in which the ischemic event had occurred.

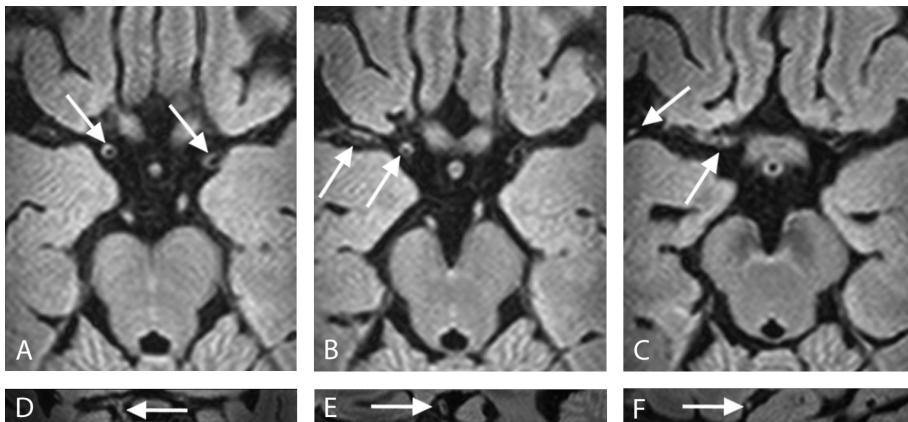


**Figure 2** A 39-year-old woman with a history of right temporal ischemic stroke presented with dysphasia and right-side hemiparesis based on cortical ischemic stroke of the left ACA territory as seen on diffusion-weighted MR images (not shown). Also, tissue loss was found due to ischemia in the flow territory of the right MCA. She was diagnosed with Moyamoya disease. (A-C) Precontrast transverse 3D MPIR-TSE images on different levels showing thickening of distal ICA wall on both sides (arrows in A, right arrow in B), continuing in both right MCA (left arrow in B), its M2 branch (left arrow in C), and the right ACA (right arrow in C). Coronal (D) and two sagittal (E, F) reconstructions also show this thickened vessel wall, extending from right ICA (arrow in D) into both right ACA and MCA (arrow in D and E) and finally M2 (arrow in F).

**TABLE** Patient characteristics, location, and enhancement of atherosclerotic lesions on magnetization preparation inversion recovery turbo spin echo (MPIR-TSE) sequence in 21 patients.

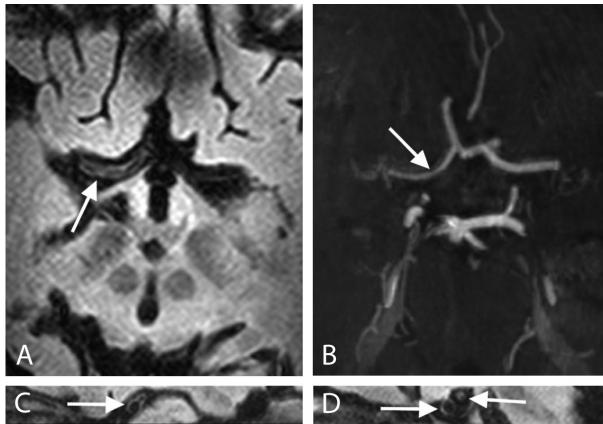
Pat.	Age (y)	Sex (M/F)	Clinical presentation	Diagnosis*	Atherosclerosis on MPIR-TSE	
					Location	CE
2	77	M	Transient monocular visual field defect left eye	Left-side amaurosis fugax	- A1 R - P2 segment R	- A1 R
3	75	F	Dysphasia and hemiparesis, right arm and leg	Ischemic stroke, left MCA territory (TOAST: unknown undetermined causes)	- M1 L - M2 branch L	- M1 L - M2 branch L
5	66	M	Transient dysphasia	TIA, left MCA territory	- M1 L - M2 L - M1 R - P1 R	- M2 L
9	79	M	Dysphasia and right-side facial paresis	Small cortical ischemic stroke, left frontal MCA territory (TOAST: unknown undetermined causes)	- Distal ICA R - Distal ICA L - M1 L	- Distal ICA R
10	83	M	Transient and permanent monocular visual field defect left eye	Retinal infarction and amaurosis fugax	- Distal ICA R - A1 R - M1 L - P1 L	- Distal ICA R
11	39	F	Dysphasia and hemiparesis, right arm and leg	Cortical ischemic stroke, left ACA territory (TOAST: evident other causes, Moyamoya disease)	- Distal ICA R - M1 R - M2 R - A1 R - Distal ICA L - A1 L	No postcontrast scan
12	76	F	Transient dysphasia and hemiparesis, right arm and leg	TIA, left MCA territory	- A1 R - M2 L	- A1 R
16	76	M	Hemiparesis, right arm and face	Ischemic stroke, left MCA territory (TOAST: evident cardioaortic embolism)	- Distal ICA R - M2 L	No enhancement
20	76	M	Mixed aphasia	Ischemic stroke, left MCA territory (TOAST: probable large artery atherosclerosis)	- P2 L	No enhancement
21	74	F	Transient left-side visual extinction, facial paresis, and total neglect	TIA, right MCA territory	- Distal ICA/M1 R - M2 R - M1 L	- M2 R
22	52	M	Transient hemiparesis, left arm and leg	TIA, right MCA territory	- Basilar artery	No enhancement
23	36	M	Transient hemiparesis, left arm and leg	Epilepsy	- A1 R	No enhancement

Table continued I

Pat.	Age (y)	Sex (M/F)	Clinical presentation	Diagnosis*	Atherosclerosis on MPIR-TSE	
					Location	CE
24	70	F	Transient hemiparesis, left arm, leg, and face	TIA, right MCA territory	- Distal ICA/M1 L - Proximal M1 R - Distal M1 R	- Distal ICA / M1 L
26	49	F	Headache and mental changes	Ischemic stroke, several arterial territories (TOAST: evident other causes, reversible vasoconstriction syndrome)	- P1 L	No enhancement
28	74	F	Headache, motor dysphasia	Migraine	- Distal ICA/M1 R - Distal M1 R - ICA/A1 L - P1 L	- Distal ICA / M1 R
29	45	F	Left-side facial and neck hypesthesia	TIA, left MCA territory (unknown vasculopathy)	- Distal ICA/M1 R - M1 L	- Distal ICA / M1 R
30	58	M	Transient hemiparesis, left arm and leg	TIA, right MCA territory	- ICA R	- ICA R
31	62	F	Mixed dysphasia	Ischemic stroke, left MCA territory (TOAST: evident cardioaortic embolism)	- M1 L - Distal basilar artery - P1 R	No enhancement
32	35	F	Permanent monocular visual field defect left eye	Ischemic stroke, right MCA territory (TOAST: unknown undetermined causes)	- A1 R	No enhancement
33	83	M	Transient dysarthria and hemiparesis, left hand and face	TIA, right MCA territory	- ICA L - M2 L - P1-P2 R - Distal basilar artery	No enhancement
35	45	F	Hemiparesis, left face, arm, and leg	Ischemic stroke, right MCA territory (TOAST: evident other causes, fibromuscular dysplasia)	- P1 R	No enhancement

A1 indicates A1 segment of ACA; ACA, anterior cerebral artery; CE, contrast enhancement; ICA, internal carotid artery; L, left; M1, M1 segment of MCA; M2, M2 branch of MCA; MCA, middle cerebral artery; P1, P1 segment of PCA; P2, P2 segment of PCA; Pt., patient; PCA, posterior cerebral artery; R, right; TIA, transient ischemic attack.

\*In case of ischemic stroke, the causative subtype was determined using the Stop Stroke Study Trial of Org 10172 in Acute Stroke Treatment (SSS-TOAST) classification criteria.<sup>24</sup>



**Figure 3** A 83-year-old man presented with left-sided retinal infarction, as well as recent history of several transient ischemic attacks (TIAs) of left MCA territory and multiple episodes of left-sided amaurosis fugax. (A) Transverse 3D MPR-TSE image shows irregularly thickened ACA vessel wall on the contralateral side (*arrow*), corresponding to local luminal narrowing on transverse TOF-MRA (*arrow* in B). (C, D) Sagittal vessel wall image reconstructions showing MCA-ACA bifurcation with narrow proximal ACA (*arrow* in C), narrowing further more distally as compared to MCA (D; *left arrow*; *right arrow* ACA).

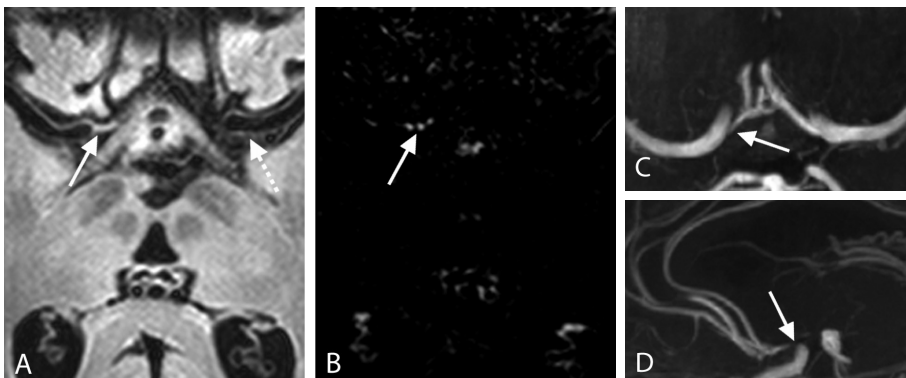


**Figure 4** A 76-year-old woman with a history of right-hemispheric transient ischemic attack (TIA) presented with transient dysphasia and right-side hemiparesis based on a TIA of the left MCA territory. (A, B) Transverse 3D MPR-TSE images before (A) and after (B) contrast administration showing normal MCA vessel wall (*dashed arrow*) and collapsed asymptomatic A1 segment on the right side (*arrow*). Enhancement of collapsed proximal ACA was visible on subtracted image (C). (D-F) TOF-MRA coronal (D), transverse (E), and sagittal (F) images show corresponding filling defect of proximal ACA (*arrow*). The collapsed ACA can also be seen on the coronal (G) and sagittal (H) 3D MPR-TSE reconstructions.

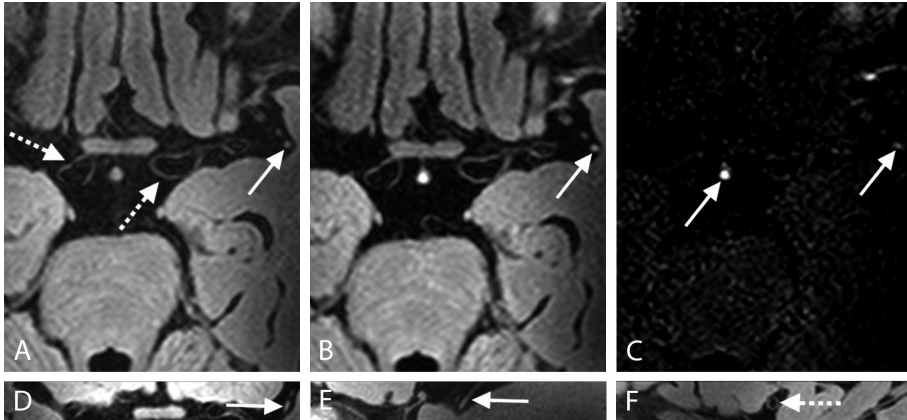


**Figure 5** A 75-year-old woman presented with dysphasia and right-side hemiparesis based on ischemic stroke of the left MCA territory with multiple cortical and subcortical ischemic areas on diffusion-weighted MR images (not shown). Transverse 3D MPR-TSE images before (A) and after contrast administration (B), and its subtraction image (C), showing smooth healthy vessel wall (*dashed arrows* in A and B) and an occluded and enhancing left M2 branch (*arrow*). Dashed arrow (C) shows enhancing infundibulum of pituitary gland as compared to enhancement of M2 branch. (D, E) Coronal and sagittal reconstruction of occluded M2 branch (*arrow*), as compared to healthy vessel wall of the MCA as seen in F (*dashed arrow*, sagittal reconstruction).

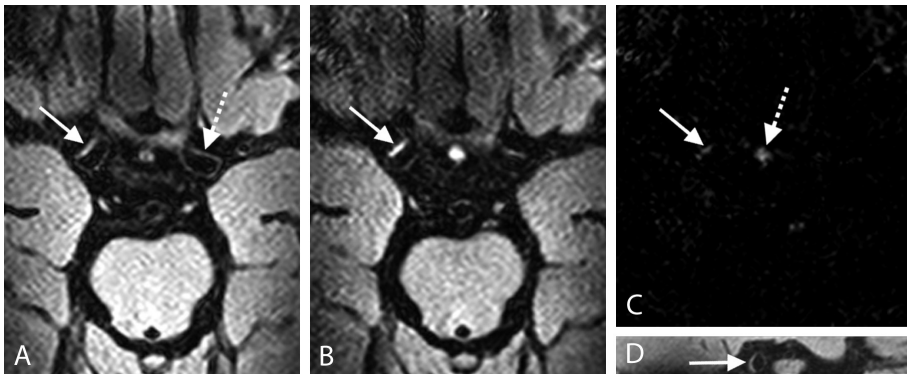


**Figure 6** A 79-year-old man with a history of TIAs of the right hemisphere presented with dysphasia and right-side facial paralysis based on small cortical ischemic stroke of the frontal part of the left MCA territory as seen on diffusion-weighted MR images (not shown). (A-C) Precontrast and postcontrast 3D MPR-TSE images (A, B) with subtraction image (C) showing focal atherosclerotic lesion of right distal ICA just before its bifurcation (*arrow* in A) as compared to healthy contralateral ICA (*dashed arrow* in A), enhancing after contrast administration (*arrow* in B and C). Dashed arrow (C) shows enhancing infundibulum of pituitary gland as compared to lesion enhancement. The lesion can be identified as a crescent-shaped vessel wall thickening on precontrast sagittal reconstruction (*arrow* in D).

## DISCUSSION

In the present study we developed the 3-dimensional MPR-TSE MRI sequence to image intracranial arterial vessel wall of normal nondiseased intracranial arteries and possible pathological arteries. With the use of 7T, we achieved high image resolution and sufficient sensitivity to allow identification of vessel wall of the major arteries of the CoW in all subjects, including healthy controls.

Only a few studies have thus far succeeded in imaging the intracranial arterial vessel wall using MRI<sup>13-17</sup>. Niizuma and colleagues<sup>13</sup> visualized MCA vessel wall with 3T in three patients but not in healthy controls. Swartz and colleagues<sup>14</sup> found enhancement patterns of different diseases such as atherosclerosis and inflammation of the intracranial vessel wall with 3T in a patient group with more complicated pathology, which could have reduced the chance of visualizing

**“...66% of the patients in our study had  $\geq$  one lesion(s) in major intracranial arteries...”**

healthy vessel wall. Ryu and colleagues<sup>15</sup> found multicontrast-weighted black blood 3T MRI to have the potential for characterization of atherosclerotic plaques. Li and colleagues<sup>16</sup> and Xu and colleagues<sup>17</sup> differentiated wall thickening, arterial remodeling, and atherosclerotic plaque with their 3T T<sub>2</sub>-weighted sequence in symptomatic and asymptomatic patients with intracranial MCA stenosis. These investigators used relatively thick slices (2 mm), which had to be planned perpendicular to the vessel, which makes it difficult to image the complete CoW. None of these studies used cerebrospinal fluid suppression to improve contrast between CSF and vessel wall and to avoid possible misinterpretation of CSF signal around a vessel for signal from the vessel wall.

We have used 7T field strength for further development of an intracranial vessel wall sequence. As discussed in **Chapter 1**, 7T yields a higher signal-to-noise ratio compared to lower field strengths, but intracranial vessel wall imaging remains challenging. The vessels of the CoW do not have a single orientation, which prohibits the use of thick slices perpendicular to the vessel orientation, as is normally performed in imaging of the carotid artery wall<sup>21</sup>. Second, inhomogeneity in the radiofrequency transmit field at 7T leads to a reduced flip angle in the occipital and temporal lobes of the brain, making small, more peripherally located arteries more difficult to identify. However, this was not a limiting factor for identifying the vessels of the CoW. Third, no body transmit coil is available with 7T systems, so non-selective inversion as used in dual inversion black blood sequences cannot be used. In the MPR-TSE sequence, we used the intrinsic flow sensitivity of TSE to obtain dark blood attributable to flow between excitation and refocusing in the TSE train.

Our results show the ability of the MPIR-TSE sequence to detect lesions and healthy intracranial vessel wall. Arteries surrounded by CSF, such as the major branches of the CoW, are best visible because of the CSF suppression applied in the sequence. This is especially useful in older individuals because atrophy of the brain causes the arteries to be surrounded by more CSF. The majority (66%) of the patients in our study had  $\geq$  one lesions in major intracranial arteries. Only 27% of the lesions (14/52) caused a stenosis, as seen on conventional TOF-MRA images. Hence, the majority of the lesions probably would have gone undetected by lumenography-based methods. Several patients showed vessel wall lesions in an arterial territory contralateral to the side of neurological symptoms. This indicates that the lesions are not always directly related to the ischemic event. The burden of intracranial lesions probably reflects the presence and severity of more generalized arterial wall pathology<sup>22</sup> in a patient. We believe that the presented method has potential to examine the relationship between intracranial arterial vessel wall pathology and TIA or ischemic stroke, for instance, in clinical longitudinal studies. In this regard, the MPIR-TSE sequence also could be used complementary to the current diagnostic imaging techniques for identifying intracranial vessel wall pathology, like atherosclerosis or Moyamoya disease, in a minimally invasive way.

The current study has some limitations. First, we scanned only a limited number of healthy volunteers. By scanning more subjects with no known cardiovascular diseases, we will be able to better discern pathological vessel wall changes from normal vessel wall and facilitate the need for a reference standard regarding vessel wall thickness. In the older healthy volunteer, vessel wall was more clearly visible than in the younger volunteers (**Figure 1**). With the current data, we are not able to judge whether this is a consequence of normal aging of the vessel wall<sup>23</sup> or asymptomatic vessel wall pathology. Second, for everyday clinical use, 7T MRI is still hampered by strict safety rules (**Chapter 6**), which currently make the MPIR-TSE sequence only applicable to a subgroup of patients. In our study, only some of all eligible patients could be scanned because of these safety rules. We expect that with technical improvements, such as an increase in the number of receive elements in a head coil, the signal-to-noise ratio at lower field strengths may improve to such a level that the resolution needed for vessel wall imaging with MPIR-TSE or other sequences may become feasible at 1.5T and 3T MRI field strengths in the future. Third, we used an MRI sequence with a small coverage (i.e., a transverse slice of 13 mm) and a relatively long acquisition time of  $\approx$  12 minutes. Because of the small coverage, small arterial branches of the large CoW

**“...majority of vessel wall lesions probably would have gone undetected...”**

arteries often could not be tracked completely. Enlarging the coverage results in even longer acquisition times, prolonging the time subjects have to lie completely still. However, the majority of subjects tolerated the acquisition time well, with limited motion artifacts. Moreover, even with the restricted coverage, the large intracerebral arteries arising from the CoW could be assessed completely.

In conclusion, intracranial vessel wall and its pathology can be depicted with MPIR-TSE imaging on 7T MRI in healthy volunteers and in ischemic stroke and TIA patients. This sequence makes it possible to study the role of intracranial arterial wall pathology in stroke and TIA in more detail.

## REFERENCE LIST

- (1) Stiel GM, Stiel LS, Schofer J, Donath K, Mathey DG. Impact of compensatory enlargement of atherosclerotic coronary arteries on angiographic assessment of coronary artery disease. *Circulation* 1989;80(6):1603-9.
- (2) Kiechl S, Willeit J. The natural course of atherosclerosis. Part II: vascular remodeling. Bruneck Study Group. *Arterioscler Thromb Vasc Biol* 1999;19(6):1491-8.
- (3) Chimowitz MI, Lynn MJ, Howlett-Smith H et al. Comparison of warfarin and aspirin for symptomatic intracranial arterial stenosis. *N Engl J Med* 2005;352(13):1305-16.
- (4) Bash S, Villablanca JP, Jahan R et al. Intracranial vascular stenosis and occlusive disease: evaluation with CT angiography, MR angiography, and digital subtraction angiography. *AJNR Am J Neuroradiol* 2005;26(5):1012-21.
- (5) Kasner SE, Chimowitz MI, Lynn MJ et al. Predictors of ischemic stroke in the territory of a symptomatic intracranial arterial stenosis. *Circulation* 2006;113(4):555-63.
- (6) Nguyen-Huynh MN, Wintermark M, English J et al. How accurate is CT angiography in evaluating intracranial atherosclerotic disease? *Stroke* 2008;39(4):1184-8.
- (7) Muhlenbruch G, Das M, Mommertz G et al. Comparison of dual-source CT angiography and MR angiography in preoperative evaluation of intra- and extracranial vessels: a pilot study. *Eur Radiol* 2010;20(2):469-76.
- (8) Glagov S, Weisenberg E, Zarins CK, Stankunavicius R, Kolettis GJ. Compensatory enlargement of human atherosclerotic coronary arteries. *N Engl J Med* 1987;316(22):1371-5.
- (9) Aoki S, Hayashi N, Abe O et al. Radiation-induced arteritis: thickened wall with prominent enhancement on cranial MR images report of five cases and comparison with 18 cases of Moyamoya disease. *Radiology* 2002;223(3):683-8.
- (10) Lam WW, Wong KS, So NM, Yeung TK, Gao S. Plaque volume measurement by magnetic resonance imaging as an index of remodeling of middle cerebral artery: correlation with transcranial color Doppler and magnetic resonance angiography. *Cerebrovasc Dis* 2004;17(2-3):166-9.
- (11) Klein IF, Lavalley PC, Touboul PJ, Schouman-Claeys E, Amarenco P. In vivo middle cerebral artery plaque imaging by high-resolution MRI. *Neurology* 2006;67(2):327-9.
- (12) Kuker W, Gaertner S, Nagele T et al. Vessel wall contrast enhancement: a diagnostic sign of cerebral vasculitis. *Cerebrovasc Dis* 2008;26(1):23-9.
- (13) Niizuma K, Shimizu H, Takada S, Tominaga T. Middle cerebral artery plaque imaging using 3-tesla high-resolution MRI. *J Clin Neurosci* 2008;15(10):1137-41.
- (14) Swartz RH, Bhuta SS, Farb RI et al. Intracranial arterial wall imaging using high-resolution 3-tesla contrast-enhanced MRI. *Neurology* 2009;72(7):627-34.
- (15) Ryu CW, Jahng GH, Kim EJ, Choi WS, Yang DM. High resolution wall and lumen MRI of the middle cerebral arteries at 3 tesla. *Cerebrovasc Dis* 2009;27(5):433-42.

## Part 2 – Chapter 2

- (16) Li ML, Xu WH, Song L et al. Atherosclerosis of middle cerebral artery: evaluation with high-resolution MR imaging at 3T. *Atherosclerosis* 2009;204(2):447-52.
- (17) Xu WH, Li ML, Gao S et al. In vivo high-resolution MR imaging of symptomatic and asymptomatic middle cerebral artery atherosclerotic stenosis. *Atherosclerosis* 2010;212(2):507-11.
- (18) Busse RF, Hariharan H, Vu A, Brittain JH. Fast spin echo sequences with very long echo trains: design of variable refocusing flip angle schedules and generation of clinical T2 contrast. *Magn Reson Med* 2006;55(5):1030-7.
- (19) Visser F, Zwanenburg JJ, Hoogduin JM, Luijten PR. High-resolution magnetization-prepared 3D-FLAIR imaging at 7.0 tesla. *Magn Reson Med* 2010;64(1):194-202.
- (20) Maes F, Collignon A, Vandermeulen D, Marchal G, Suetens P. Multimodality image registration by maximization of mutual information. *IEEE Trans Med Imaging* 1997;16(2):187-98.
- (21) Watanabe Y, Nagayama M. MR plaque imaging of the carotid artery. *Neuroradiology* 2010;52(4):253-74.
- (22) Weintraub HS. Identifying the vulnerable patient with rupture-prone plaque. *Am J Cardiol* 2008;101(12A):3F-10F.
- (23) Homma S, Hirose N, Ishida H, Ishii T, Araki G. Carotid plaque and intima-media thickness assessed by b-mode ultrasonography in subjects ranging from young adults to centenarians. *Stroke* 2001;32(4):830-5.
- (24) Ay H, Furie KL, Singhal A, Smith WS, Sorensen AG, Koroshetz WJ. An evidence-based causative classification system for acute ischemic stroke. *Ann Neurol* 2005;58(5):688-97.



**Adapted from:**

**Van der Kolk AG**, Hendrikse J, Brundel M, Biessels GJ, Smit EJ, Visser F, Lijten PR, Zwaneburg JJM. ***Multi-sequence whole-brain intracranial vessel wall imaging at 7.0 tesla.*** Eur Radiol 2013;23(11):2996-3004, with permission.

# Chapter 3

## WHOLE-BRAIN INTRACRANIAL VESSEL WALL SEQUENCES WITH DIFFERENT IMAGE CONTRASTS

---

Anja G van der Kolk, MD<sup>1</sup>; Jeroen Hendrikse, MD PhD<sup>1</sup>; Manon Brundel, MD<sup>2</sup>;  
Geert J Biessels, MD PhD<sup>2</sup>; Ewoud J Smit, MD PhD<sup>1</sup>; Fredy Visser<sup>1,4</sup>;  
Peter R Luijten, PhD<sup>1</sup>; Jaco JM Zwanenburg, PhD<sup>1,3</sup>

*From the <sup>1</sup>Department of Radiology, <sup>2</sup>Department of Neurology, and <sup>3</sup>Image Sciences Institute, University Medical Center Utrecht, The Netherlands; and <sup>4</sup>Philips Healthcare, Best, The Netherlands*

# Key points

- » Intracranial vessel wall imaging using specific vessel wall MRI sequences improves the diagnosis of cerebrovascular diseases.
- » Conventional 7T MRI vessel wall sequences cannot image the whole cerebral arterial tree because of limited coverage.
- » More distal vessel wall pathology will therefore be missed.
- » Three new whole-brain 7T MRI vessel wall sequences compare favorably with the 7T smaller-coverage sequence, especially in patients.
- » These sequences can demonstrate the entire cerebral arterial tree with different image contrast weightings, enabling (future) lesion characterization.
- » They should help in diagnosis and differentiation of several types of intracranial vessel wall abnormalities.

## INTRODUCTION

Several magnetic resonance imaging (MRI) methods have previously been shown to be able to visualize the intracranial arterial vessel wall<sup>1-8</sup>, using the higher signal-to-noise ratio (SNR) at 3 or 7 tesla (T) to depict wall abnormalities of these small arteries. As was shown in **Chapter 2**<sup>7</sup>, at 7T also normal (non-diseased) vessel walls can be depicted, and, owing to isotropic voxels with sufficient SNR, reconstructions can be made in different planes, enabling extensive assessment of healthy and diseased intracranial vessel wall.<sup>7</sup> In addition, the presented sequence (magnetization preparation inversion recovery turbo spin echo [MPIR-TSE]) had the advantage of actively nulled cerebrospinal fluid (CSF), so that visibility of the vessel wall is not dependent on local CSF flow voids. However, its disadvantage was the limited coverage.<sup>7</sup> Although most vessel wall abnormalities may be present in the basilar artery, distal internal carotid artery and proximal circle of Willis (CoW) branches, more distal lesions (for instance, of M2 or M3 branches of the middle cerebral artery [MCA]) may be missed. Furthermore, the presented sequence was designed to have  $T_1$  image contrast for depiction of intracranial atherosclerosis before and after gadolinium-based contrast medium administration. The presence of a multisequence MRI protocol, including proton density (PD)-,  $T_1$ - and  $T_2$ -weighting, may be better at characterizing intracranial vessel wall abnormalities, similar to plaque characterization of the internal carotid artery.<sup>9,10</sup> In the study described in this chapter, a multisequence (PD-,  $T_1$ - and  $T_2$ -weighting) high-resolution MRI protocol with whole-brain coverage was developed for assessment of intracranial vessel wall lesions, and compared with the 13 mm coverage of the original MPIR-TSE sequence.<sup>7</sup>

**“...a multisequence MRI protocol may better characterize intracranial vessel wall abnormalities, similar to plaque characterization of the internal carotid artery...”**

## MATERIALS AND METHODS

### Study population

This prospective study was approved by the Institutional Review Board of our hospital. All subjects gave written informed consent. Five healthy volunteers (mean age, 26 years; range, 22–34 years) and 17 patients with varying cerebrovascular diseases were included in this study. Of the 17 patients, 8 patients had had a cerebral ischemic infarct, 5 patients had had a transient ischemic attack (TIA), 1 patient was diagnosed with Moyamoya disease, 1 patient had biopsy-proven primary angiitis of the central nervous system (PACNS), 1 patient had cerebral autosomal dominant arteriopathy with subcortical infarcts and leukoencephalopathy

(CADASIL) and 1 patient was clinically diagnosed with arteritis temporalis. The five healthy volunteers underwent unenhanced MRI with the multisequence protocol, including the three whole-brain MPR-TSE sequences and the limited-coverage MPR-TSE sequence. In all patients, the unenhanced whole-brain  $T_1$ -weighted MPR-TSE sequence was performed; in all patients except one, enhanced  $T_1$ -weighted MPR-TSE images were also obtained  $\approx 5$  minutes after administration of 0.1 mL/kg of a gadolinium-containing contrast medium (gadobutrol, Gadovist 1.0 mmol/mL, Bayer Schering Pharma, Newbury, UK), for possible depiction of enhancing vessel walls. In two patients, additional intracranial vessel wall sequences were obtained for clinical purposes (limited-coverage MPR-TSE sequence in both patients, whole-brain coverage  $T_2$ -weighted MPR-TSE sequence in one patient).

### **Intracranial vessel wall sequences**

Imaging was performed on a 7T whole-body system (Philips Healthcare, Cleveland, OH, USA) with a 32-channel receive coil and a volume transmit/receive coil for transmission (Nova Medical, Wilmington, MA, USA). We developed three whole-brain intracranial vessel wall sequences with different image contrast weightings, based on the MPR-TSE method.<sup>7</sup> The MPR-TSE sequence consists of an inversion pulse to null the CSF, a dedicated TSE refocusing train for obtaining black blood and for limiting the specific absorption rate (SAR), isotropic voxels to take into account the varying spatial orientation of the vessels and branches of the CoW, and magnetization preparation (MP) to improve the SNR.<sup>7,11</sup> For this limited-coverage (13 mm) MPR-TSE sequence the following MRI parameters were used<sup>7</sup>: field-of-view (FOV) 220 x 180 x 13 mm<sup>3</sup>, acquired resolution 0.8 x 0.8 x 0.8 mm<sup>3</sup>, TSE factor of 116 (including 4 startup echoes), echo train length 546 ms, repetition time (TR) 6050 ms, inversion time (TI) 1770 ms, echo time (TE) 80 ms (given the used  $T_1$ ,  $T_2$  and variable refocusing flip angle scheme, this corresponds to an equivalent TE of 23 ms in the case where full refocusing angles would be used<sup>12</sup>), number of signal averages (NSA) of 2, MR data acquisition duration  $\approx 12$  minutes. Care was taken to include the whole CoW in the axial plane.

To increase coverage, non-selective short radiofrequency (RF) pulses and sensitivity encoding (SENSE) in two directions were used to obtain a MPR-TSE sequence with 190 mm feet-head whole-brain coverage (**Figure 1**). The imaging parameters were adapted to obtain different image contrast weightings, namely PD-weighting,  $T_1$ -weighting and  $T_2$ -weighting. All sequences had the same variable refocusing flip angle scheme<sup>12</sup>, with low refocusing angles ranging between 12° and 40°, optimized to yield a constant signal response for tissue with a  $T_1/T_2$  of 2000/55 ms for at least half the train length. This allows for a long readout with limited blurring. The following imaging parameters were used for all three image

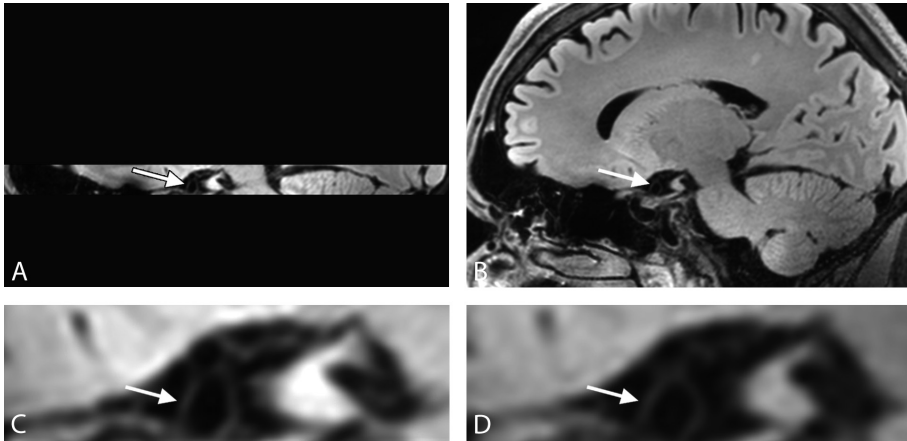


**Figure 1** Comparison of coverage between the 7 tesla (T) 3-dimensional (3D) limited-coverage magnetization preparation inversion recovery turbo spin echo (MPIR-TSE) sequence (A) and the whole-brain MPR-TSE sequence (B). On both sequences, the vessel wall of the distal internal carotid artery (ICA) can be observed (arrows in A and B), which is more clearly illustrated on the zoomed-in images of both sequences (arrow in C for the limited-coverage and arrow in D for the whole-brain MPR-TSE sequence). Note that the vessel lies at the inferior border of the field of view (FOV) of the limited-coverage sequence (A), which illustrates the sensitivity of this sequence to malpositioning of the FOV, or patient motion between the image on which FOV planning is performed and the actual vessel wall sequence.

contrast weightings: FOV 250 x 250 x 190 mm<sup>3</sup> in sagittal orientation, acquired resolution 0.8 x 0.8 x 0.8 mm<sup>3</sup> (0.5  $\mu$ L), flip angle 150° (overtipping was used to compensate for low B<sub>1</sub> values, especially at the periphery of the brain), TSE factor of 168 (including 10 startup echoes) and echo train length 560 ms. For the individual sequences, the following additional imaging parameters were used: PD-weighted MPR-TSE sequence, TR/TI/TE 6000/1900/37 ms (equivalent TE 19 ms<sup>12</sup>), magnetization preparation mixing time (MP) 100 ms, NSA of 2, 2D SENSE factor of 8 (2 in anterior–posterior [AP] direction, 4 in right-left [RL] direction), MR data acquisition duration  $\approx$  12 minutes; T<sub>1</sub>-weighted MPR-TSE sequence, TR/TI/TE 3 952/1375/37 ms (equivalent TE 19 ms<sup>12</sup>), MP 50 ms, NSA of 2, 2D SENSE factor of 6 (2 in AP direction, 3 in RL direction), MR data acquisition duration  $\approx$  11 minutes; and T<sub>2</sub>-weighted MPR-TSE sequence, TR/TI/TE 8000/2200/287 ms (equivalent TE 126 ms<sup>12</sup>), MP 100 ms, NSA of 1, 2D SENSE factor of 6 (2 in AP direction, 3 in RL direction), MR data acquisition duration  $\approx$  11 minutes.

### Image processing and evaluation

Images were processed on an offline workstation (Philips). For analysis, transverse reconstructions 0.8 mm thick with a 0.4 mm overlap were made of all four sequences obtained from the healthy volunteers, using the spatial orientation of

the limited-coverage sequence as standard reference. Also, reconstructed slices of the whole-brain sequences were limited to the maximum amount of slices possible for the limited-coverage sequence, which was 32. In this way, care was taken to obtain exactly the same data sets for further analysis.

Qualitative analysis<sup>13</sup> was performed using a research workstation (iX Viewer; Image Sciences Institute, Utrecht, The Netherlands), by three independent observers (two neuroradiologists with respectively 20 and 5 years of experience, and one medical researcher with limited neuroradiologic experience), who were blinded to sequence information during assessment. First, a side-by-side analysis was performed, in which observers were individually presented with random and blinded pairs of images acquired in the healthy volunteers with the four different vessel wall sequences. All possible pairwise comparisons (six combinations for each of the five volunteers) were presented. Images were scored for overall image quality of the CoW and least image artefacts using a three-point scale (better, equal, or worse). Observers were instructed to choose a preferred image and only score images as equal when they could not make a decision. Second, observers scored all images individually, presented in random order, for overall artifacts (0 = artifacts hampering assessment, 1 = moderate artifacts, but images assessable, 2 = no artifacts) and visibility of the arterial vessel wall (0 = poor, 1 = moderate, 2 = good) of the arteries of the CoW. Also, imaging quality of all separate arterial vessel walls of the branches of the CoW (anterior [ACA], middle [MCA] and posterior [PCA] cerebral arteries with their first and second branches [e.g., M1 and M2 for MCA], basilar artery and distal internal carotid arteries [ICA]) were scored (0 = not visible, 1 = poor, 2 = moderate, 3 = good).

In addition to this qualitative analysis, a signal intensity profile analysis was performed on images of both healthy volunteers and patients, for quantification of the image contrast ratio of the arterial vessel wall relative to the adjacent signal (CSF and blood) on all sequences used. Multiple, parallel signal profiles perpendicular to the vessel wall were automatically drawn within a user-defined region of interest (ROI) on all images, using Matlab (release 2011a, MathWorks, Natick, MA, USA). This ROI was chosen based on accessibility of the region on all images, and was defined as either the right (four volunteers and 11 patients) or left (four patients) distal ICA, or the distal basilar artery when the ICA was not accessible on all images (one volunteer and two patients). Of the multiple signal profiles, the mean highest (vessel wall) and mean lowest (background signal) signals were calculated per sequence.

## Analyses

The side-by-side analysis represents a paired test, in which the observer decides which imaging sequence is considered of superior quality. Observer scores from the side-by-side comparison were expressed as the overall percentage of cases in which one technique was found to be better than, equal to or worse than the other technique. A technique was considered superior to another technique if the overall superiority score was higher than 75%. For the three independent observers, the mean quality assessment scores of each sequence were calculated for artifacts and overall quality, based on the individual sequence scoring. Differences in scores between sequences were evaluated using the results from the assessment of separate arteries. For the signal profile analysis, the ratio of vessel wall and background signal intensity was calculated as a measure of image contrast / vessel wall conspicuity. Differences of signal ratios between the four sequences in healthy volunteers were further analyzed using the Related Samples Friedman's Two-Way Analysis of Variance by Ranks. All statistical tests were performed using statistics software (SPSS version 20.0). A *P* value of < 0.05 was considered to be statistically significant.

## RESULTS

Whole-brain coverage for the PD-,  $T_1$ - and  $T_2$ -weighted vessel wall sequences was successfully obtained in all subjects. Vessel walls of the large vessels of the CoW, as well as their smaller branches (**Figure 2**), were clearly visible on all whole-brain examinations. No major (motion) artifacts that prohibited further evaluation of the results were found.

Results of the qualitative analysis are reported in **Table 1** and **Table 2**. For the side-by-side analysis, all three whole-brain sequences had similar ratings. However, the limited-coverage MPR-TSE sequence was judged to give the best conspicuity of the vessel walls in 64-87% of cases. For the individual sequence scoring, similar results were found (**Table 2**). Ratings for overall image quality were similar among the three whole-brain sequences (**Figure 3** and **Figure 4**), while the limited-coverage MPR-TSE sequence scored better.

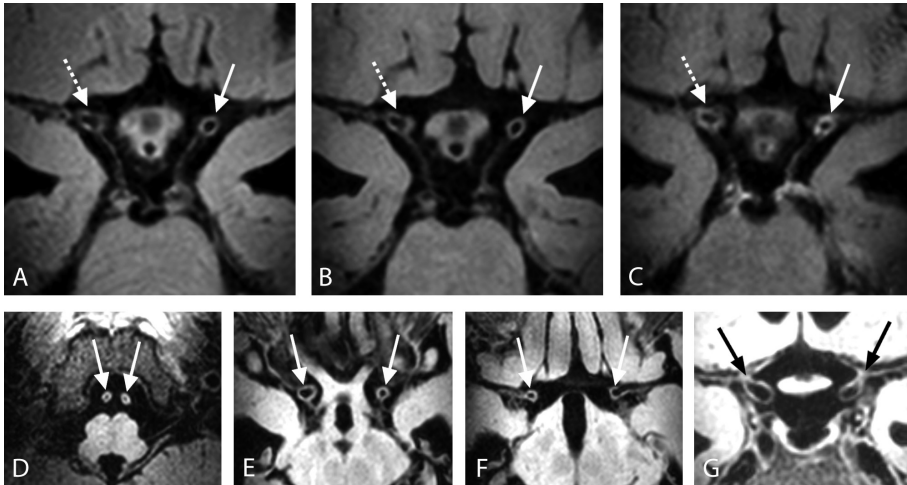


**Figure 2** 7T limited-coverage 3D MPR-TSE (A) and 3D whole-brain T<sub>1</sub>-weighted MPR-TSE images before (B) and after (C-G) contrast medium administration in a 50-year-old patient with cerebral vasculitis. Vessel wall imaging shows diffuse thickening of all intracranial vessel walls, like the distal ICA; *dashed white arrow* in A-C). After contrast medium administration, there is diffuse enhancement of most of the intracranial arteries, including both distal ICAs (*white arrows* in E and G), left (*right white or black arrow* in C, F and G) and right (*left white or black arrow* in F and G) middle cerebral artery (MCA), and vertebral arteries (*white arrows* in D).

**TABLE 1** Side-by-side comparison analysis of the three whole-brain magnetization preparation inversion recovery (MPR) turbo spin echo (TSE) sequences, relative to the limited-coverage MPR-TSE sequence.

Comparison (in percentages*)	PD MPR-TSE	T <sub>1w</sub> MPR-TSE	T <sub>2w</sub> MPR-TSE
Limited-coverage MPR-TSE >	87	87	64
Limited-coverage MPR-TSE =	13	13	36
Limited-coverage MPR-TSE <	0	0	0
PD-weighted MPR-TSE >	-	34	47
PD-weighted MPR-TSE =	-	33	20
PD-weighted MPR-TSE <	-	33	33
T <sub>1</sub> -weighted MPR-TSE >	-	-	29
T <sub>1</sub> -weighted MPR-TSE =	-	-	50
T <sub>1</sub> -weighted MPR-TSE <	-	-	21

MPR-TSE indicates magnetization-preparation inversion recovery turbo spin echo; PD, proton density; T<sub>1w</sub>, T<sub>1</sub>-weighted; T<sub>2w</sub>, T<sub>2</sub>-weighted; >, better; =, equal; <, worse.

\*For each side-by-side comparison, 15 scores were obtained (5 cases x 3 observers), and the percentage (rounded) better than, equal to or worse was calculated per comparison.

**TABLE 2** Qualitative individual sequence scoring for artifacts and circle of Willis (CoW) visibility; quantitative mean MRI signal intensity ratios of all vessel wall sequences compared with the surrounding cerebrospinal fluid / blood.

	Limited-coverage MPIR-TSE	PD MPIR-TSE	T <sub>1</sub> w MPIR-TSE	T <sub>2</sub> w MPIR-TSE
Artifacts, mean(range)*	1.27 (0-2)	1.33 (0-2)	1.40 (1-2)	1.07 (0-2)
Visibility CoW, mean(range)*	1.20 (0-2)	0.60 (0-2)	0.47 (0-1)	0.73 (0-2)
Signal ratio HV, mean(range) †	2.6 (2.0-3.2)	2.2 (1.7-3.1)	2.0 (1.6-2.4)	2.2 (1.7-2.8)
Signal ratio P, mean(range)	2.7 (2.6-2.7) ‡	-	3.2 (1.9-4.5) §	2.3 §

MPIR-TSE indicates magnetization-preparation inversion recovery turbo spin echo; PD, proton density; T<sub>1</sub>w, T<sub>1</sub>-weighted; T<sub>2</sub>w, T<sub>2</sub>-weighted; CoW, circle of Willis; HV, healthy volunteers; P, patients.

\*Based on 15 scores (5 cases x 3 observers)

†Based on the profile measurements in 2 patients (pre-contrast)

‡Based on the profile measurements in 17 patients

§Based on the profile measurements in 1 patient (Moyamoya disease)

¶No statistically significant difference between sequences ( $P = 0.179$ )

Results of the quantitative analyses can be found in **Table 2**. The signal ratios for all three whole-brain sequences were similar, with approximately twice as much signal in the vessel walls compared with their surroundings. For the limited-coverage MRI, this signal ratio between vessel wall and surroundings was 2.6. There was no statistically significant difference in mean ratio between the four different sequences ( $P = 0.179$ ).

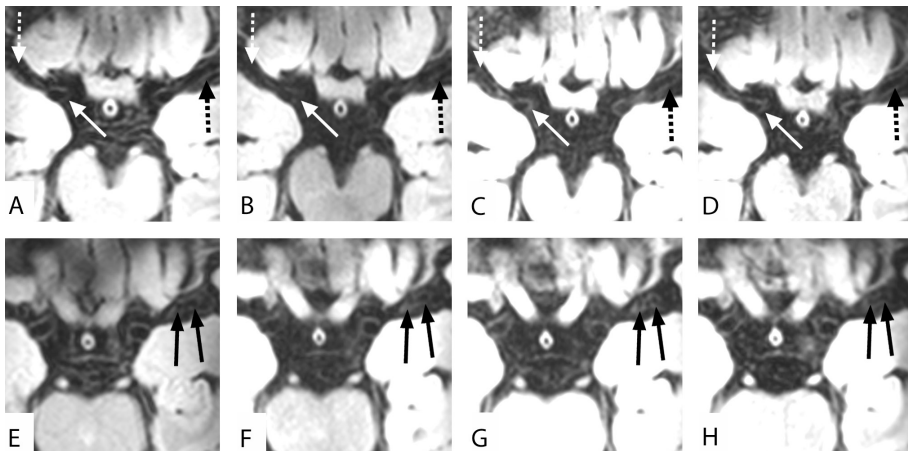


**Figure 3** Qualitative comparison of 7T limited-coverage 3D MPIR-TSE (A, E), whole-brain 3D proton density (PD)-weighted (B, F), T<sub>1</sub>-weighted (C, G) and T<sub>2</sub>-weighted (D, H) MPIR-TSE images of a 25-year-old healthy volunteer, showing vessel wall of the proximal (*white arrow* in A-D) and distal (*dashed white arrow* in A-D) right MCA, and of the distal left MCA (*dashed black arrow* in A-D). The origins of two lenticulostriate arteries emanating from the left MCA can also be appreciated (*black arrows* in E-H).

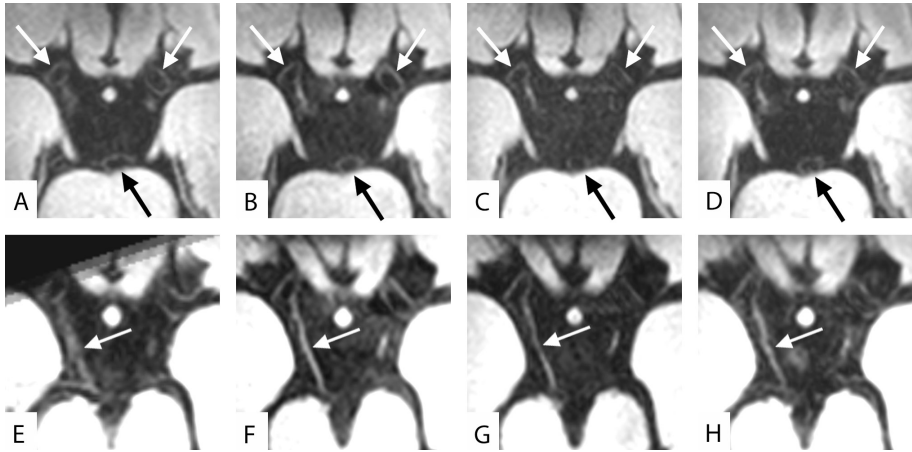


**Figure 4** Qualitative comparison of 7T limited-coverage 3D MPR-TSE (A, E), whole-brain 3D PD-weighted (B, F), T<sub>1</sub>-weighted (C, G) and T<sub>2</sub>-weighted (D, H) MPR-TSE images of a 34-year-old healthy volunteer, showing vessel wall of the left and right distal ICA (*white arrows* in A-D) and basilar artery (*black arrow* in A-D). A hyperintense posterior communicating artery can be seen on the right (*white arrow* in E-H); because of the small diameter of the artery, no lumen can clearly be seen.

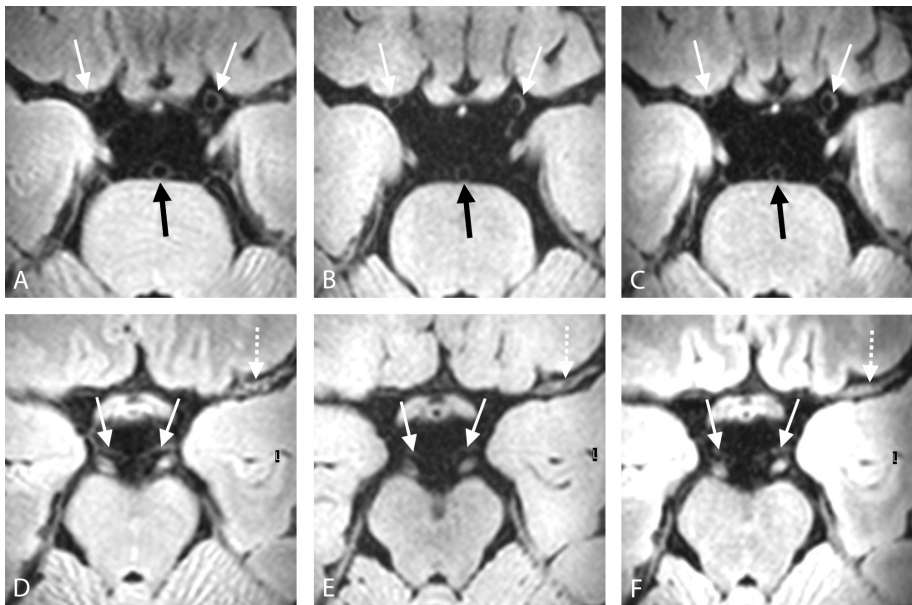


**Figure 5** 7T limited-coverage 3D MPR-TSE (A, D), and whole-brain T<sub>1</sub>-weighted (B, E) and T<sub>2</sub>-weighted (C, F) MPR-TSE images of a 31-year-old patient with Moyamoya disease. On MR imaging, vessel wall of the left distal ICA (*right white arrow* in A-C) is slightly more hyperintense compared with the right distal ICA (*left white arrow* in A-C) and basilar artery (*black arrow* in A-C). Also, both distal ICAs are relatively narrow compared with the basilar artery. More distally, the left MCA is seen to be almost occluded, with thickened vessel wall (*dashed arrow* in D-F). The normal P1 segment of the posterior cerebral artery can also be assessed (*white arrow* in D-F).

In the patients, similar signal ratios were found when compared with ratios in the healthy volunteers, with the exception of the whole-brain coverage  $T_1$ -weighted MPR-TSE sequence, which scored better in patients than in healthy volunteers, and even exceeded the limited-coverage MPR-TSE signal ratio. All sequences gave similar diagnostic information. Additionally, vessel walls of more peripherally located arteries, like A2 and M2 branches and their subdivisions, could be identified in these patients. For instance, in a patient with vasculitis (**Figure 2**) generalized enhancement of vessel walls of the proximal and distal intracranial arteries could be seen on the whole-brain  $T_1$ -weighted MPR-TSE sequence after contrast medium administration, extending far into the A2 segments of the ACA. These segments could not be appreciated on the limited-coverage MPR-TSE sequence owing to the limited FOV.

## DISCUSSION

In this study we evaluated a 7T multisequence MRI protocol for intracranial vessel wall assessment with whole-brain coverage (190mm feet-head coverage), using MPR-TSE with optimized blood and CSF suppression. In five healthy volunteers, vessel walls were clearly visible on all three whole-brain sequences, and we showed the clinical usability of these sequences in 17 patients with intracranial cerebrovascular disease. Although the limited-coverage (13 mm feet-head) MPR-TSE sequence (presented in **Chapter 2**) was scored better than the whole-brain MPR-TSE sequences for vessel wall conspicuity and vessel wall contrast-to-noise ratio (CNR) in the healthy volunteers, this difference was not significant for the quantitative analysis, and could not be seen in patients.

Several studies have shown successful imaging of the intracranial arterial vessel wall, mainly using 3T MRI.<sup>1-6, 14-17</sup> Although a high in-plane spatial resolution was achieved, most sequences presented did not achieve isotropic voxels and, apart from one sequence presented by Turan and colleagues<sup>9</sup>, have only limited coverage with relatively thick slices. For intracranial vessel wall imaging, both isotropic voxels and whole-brain coverage are important for application of sequences in clinical practice. Isotropic voxels have the advantage of enabling image reconstructions in multiple directions. An image reconstructed perpendicular to an intracranial artery may give the best interpretation of vessel wall thickening. Because cerebral arteries do not have a single spatial orientation, non-isotropic voxels will not allow for optimal vessel wall assessment of all intracranial arteries simultaneously in one acquisition with a single orientation. Whole-brain coverage further enables optimal assessment of intracranial arteries by enabling visualization of not only larger intracranial arteries but also the medium-sized or small arteries that are

often affected by cerebral vascular disease, like cerebral vasculitis and CADASIL,<sup>18-20</sup> and are not easily visualized using limited-coverage sequences.<sup>15, 16, 21</sup> Also, in many patients with small cortical infarcts and suspected vasculitis, no arterial vessel wall abnormalities such as enhancement can be found in the larger intracranial arteries.<sup>18</sup> Furthermore, positioning of the FOV for a limited-coverage sequence is operator-dependent, increasing the risk of missing possible arterial vessel wall lesions because the affected artery is not within the imaging volume.

In the present study we demonstrated the ability to increase coverage of the limited-coverage intracranial vessel wall MPR-TSE sequence presented in **Chapter 2**, to obtain isotropic whole-brain-coverage sequences. This increase was obtained by combining 2D SENSE with non-selective, short RF pulses. The non-selective RF pulses allowed for short echo spacing in the TSE train, and hence efficient data sampling, which is illustrated by the fact that the duration of both TSE trains was similar (560 ms for whole-brain-coverage vs 546 ms for the limited-coverage sequence), while the whole-brain coverage sequences had a considerably higher TSE factor (168 versus 116, respectively). Two-dimensional SENSE yielded fast encoding of a large 3D volume, which was facilitated by the use of a 32-channel receive coil that allowed for acceleration factors of 6 to 8. The TSE trains for both the limited-coverage sequence and the sequences with whole-brain coverage had variable reduced refocusing angles to obtain a flat signal response for at least half the train length, thereby avoiding blurring owing to decay over the long TSE train.

The MR sequences with whole-brain coverage could be exploited for assessment of intracranial arterial vessel wall abnormalities of larger as well as smaller intracranial arteries. Although the qualitative analysis showed a predisposition towards the limited-coverage MPR-TSE sequence, it should be noted that, for unbiased scoring, analyzed coverage for the whole-brain sequences conformed to the limited-coverage sequence. Therefore, the advantage of having greater coverage was not taken into account in these analyses. Furthermore, although some image contrast is lost, a clear contrast between vessel wall and surrounding CSF / blood still remains present. This effect can best be appreciated on the images of two of the patients in this study (**Figure 2** and **Figure 5**). Therefore, in our opinion the whole-brain coverage outweighs the less favorable scoring results and slight decrease in contrast ratio of the vessel walls in the healthy volunteers.

Lately, several studies have shown enhancement patterns of arterial vessel walls after ischemic stroke not associated with vasculitis. It has been suggested that these enhancement patterns might be indicative of a more vulnerable state of atherosclerotic plaque.<sup>9, 14, 16</sup> Like MR characterization of atherosclerotic plaques in the carotid artery, it could be deduced that intracranial atherosclerotic lesions

can be characterized correspondingly, for instance by identifying a necrotic core or intraplaque hemorrhage, using different MR image contrast weightings. This could increase our understanding of the exact role of intracranial atherosclerosis in the pathogenesis of ischemic stroke, i.e. as a primarily static obstruction increasing the risk of even small emboli occluding the vessel lumen, or as primarily dynamic plaque prone to plaque rupture and subsequent occlusion. The presented whole-brain MPR-TSE sequence was developed with three different image contrast weightings, enabling more detailed characterization of vessel wall abnormalities.

Our study has limitations. First, for assessment of sequence quality we primarily used a small sample size of young healthy volunteers. It is known that in young volunteers the vessel wall can be less easily distinguished because of limited vessel wall thickness and the absence of (significant) atrophy.<sup>7</sup> This might have influenced both observer scoring and quantitative analysis using signal profiles. Therefore, we included 17 clinical patients for quantitative analysis, which showed better visualization of the intracranial vessel wall on the different vessel wall sequences. Second, all sequences were developed at 7T, in order to achieve whole-brain maximum spatial resolution within reasonable acquisition time. However, current safety rules regarding subject MRI at (ultra)high field strength are very strict when concerning metallic implants, like stents or operation clips, which are often present in patients with cerebrovascular disease. These patient contraindications currently decrease the number of patients who could undergo imaging at 7T. However, we expect that increasing knowledge of and experience with metallic implants at 7T will result in wider clinical applicability (**Chapter 6**). Further, vessel walls of very small arteries, like branches from the A3 or M3 segments of the ACA and MCA, respectively, will not always be distinguishable with the currently used spatial resolution. A 7T sequence with an ultra-high in-plane spatial resolution and, consequently, smaller and focused FOV, might prove to have an additional value in the assessment of portions of these very small branches.

Another limitation may be related to the clinical use of the different whole-brain MRI sequences for assessment of brain tissue. Although TR and TE of all three sequences are consistent with PD-, T<sub>1</sub>- and T<sub>2</sub>-contrast weighting, these weightings are primarily optimized for vessel wall image contrast. As a consequence, contrast between gray and white matter, as can be seen in **Figure 2**, **Figure 3**, **Figure 4**, and **Figure 5**, does not correspond exactly to the expected contrast between these tissues, which might also apply for the signal characteristics of brain abnormalities.

**“...recommend the T<sub>1</sub>-weighted MPR-TSE sequence for patients suspected of cerebral vasculitis, or suspected of dissection of one of the intracranial arteries...”**

Therefore, care should be taken when assessing brain parenchyma on these sequences. Still, as can be seen from the prominent contrast enhancement on the whole-brain  $T_1$ -weighted MPR-TSE sequence (**Figure 2**), this sequence is suitable for imaging enhancing pathologic features, not only of the vessel wall, like vasculitis, but also of other brain abnormalities.

**“...whole-brain assessment of the intracranial arterial vessel wall with multiple different image contrast weightings...”**

Finally, the presented whole-brain sequences will, together and including a postcontrast  $T_1$ -weighted sequence, take  $\approx$  45 minutes of acquisition time, which might be difficult to implement clinically

owing to time constraints. However, by combining one or more whole-brain sequences, intracranial vessel wall imaging protocols can be made that are tailored to the patient-specific clinical question. In this regard, we would recommend the  $T_1$ -weighted MPR-TSE sequence, before and after contrast medium administration, for patients suspected of cerebral vasculitis, or suspected of dissection of one of the intracranial arteries. The  $T_1$ -weighted MPR-TSE sequence alone can be used to screen for possible vessel wall abnormalities other than vasculitis, after which the PD- and  $T_2$ -weighted sequence can be obtained when vessel wall abnormalities are found, to characterize these abnormalities.

In conclusion, with the multisequence whole-brain vessel wall protocol, we have shown the possibility of whole-brain assessment of the intracranial arterial vessel wall with multiple different image contrast weightings. In future, vessel wall imaging using multisequence MRI at 7T may be able to help differentiate several types of intracranial vessel wall abnormalities in the same way that MRI can help assess carotid artery plaques.

## REFERENCE LIST

- (1) Niizuma K, Shimizu H, Takada S, Tominaga T. Middle cerebral artery plaque imaging using 3-tesla high-resolution MRI. *J Clin Neurosci* 2008;15(10):1137-41.
- (2) Li ML, Xu WH, Song L et al. Atherosclerosis of middle cerebral artery: evaluation with high-resolution MR imaging at 3T. *Atherosclerosis* 2009;204(2):447-52.
- (3) Swartz RH, Bhuta SS, Farb RI et al. Intracranial arterial wall imaging using high-resolution 3-tesla contrast-enhanced MRI. *Neurology* 2009;72(7):627-34.
- (4) Ryu CW, Jahng GH, Kim EJ, Choi WS, Yang DM. High resolution wall and lumen MRI of the middle cerebral arteries at 3 tesla. *Cerebrovasc Dis* 2009;27(5):433-42.
- (5) Xu WH, Li ML, Gao S et al. In vivo high-resolution MR imaging of symptomatic and asymptomatic middle cerebral artery atherosclerotic stenosis. *Atherosclerosis* 2010;212(2):507-11.
- (6) Ma N, Jiang WJ, Lou X et al. Arterial remodeling of advanced basilar atherosclerosis: a 3-tesla MRI study. *Neurology* 2010;75(3):253-8.
- (7) van der Kolk AG, Zwanenburg JJ, Brundel M et al. Intracranial vessel wall imaging at 7.0-T MRI. *Stroke* 2011;42(9):2478-84.
- (8) Aoki S, Shirouzu I, Sasaki Y et al. Enhancement of the intracranial arterial wall at MR imaging: relationship to cerebral atherosclerosis. *Radiology* 1995;194(2):477-81.
- (9) Turan TN, Bonilha L, Morgan PS, Adams RJ, Chimowitz MI. Intraplaque hemorrhage in symptomatic intracranial atherosclerotic disease. *J Neuroimaging* 2011 April;21(2):e159-e161.
- (10) Shi M, Wang S, Zhou H, Cheng Y, Feng J, Wu J. Wingspan stenting of symptomatic middle cerebral artery stenosis and perioperative evaluation using high-resolution 3 Tesla MRI. *J Clin Neurosci* 2012;19(6):912-4.
- (11) Visser F, Zwanenburg JJ, Hoogduin JM, Luijten PR. High-resolution magnetization-prepared 3D-FLAIR imaging at 7.0 tesla. *Magn Reson Med* 2010;64(1):194-202.
- (12) Busse RF, Hariharan H, Vu A, Brittain JH. Fast spin echo sequences with very long echo trains: design of variable refocusing flip angle schedules and generation of clinical T2 contrast. *Magn Reson Med* 2006;55(5):1030-7.
- (13) Smit EJ, Vonken EJ, van der Schaaf IC et al. Timing-invariant reconstruction for deriving high-quality CT angiographic data from cerebral CT perfusion data. *Radiology* 2012;263(1):216-25.
- (14) Vergouwen MD, Silver FL, Mandell DM, Mikulis DJ, Swartz RH. Eccentric narrowing and enhancement of symptomatic middle cerebral artery stenoses in patients with recent ischemic stroke. *Arch Neurol* 2011;68(3):338-42.
- (15) Lou X, Ma N, Ma L, Jiang WJ. Contrast-enhanced 3T high-resolution MR imaging in symptomatic atherosclerotic basilar artery stenosis. *AJNR Am J Neuroradiol* 2013;34(3):513-7.
- (16) Skarpathiotakis M, Mandell DM, Swartz RH, Tomlinson G, Mikulis DJ. Intracranial atherosclerotic plaque enhancement in patients with ischemic stroke. *AJNR Am J Neuroradiol* 2013;34(2):299-304.
- (17) Qiao Y, Steinman DA, Qin Q et al. Intracranial arterial wall imaging using three-dimensional high isotropic resolution black blood MRI at 3.0 tesla. *J Magn Reson Imaging* 2011;34(1):22-30.

## Part 2 – Chapter 3

- (18) Scolding NJ. Central nervous system vasculitis. *Semin Immunopathol* 2009;31(4):527-36.
- (19) Pantoni L. Cerebral small vessel disease: from pathogenesis and clinical characteristics to therapeutic challenges. *Lancet Neurol* 2010;9(7):689-701.
- (20) Bousser MG, Biouesse V. Small vessel vasculopathies affecting the central nervous system. *J Neuroophthalmol* 2004;24(1):56-61.
- (21) Kim JM, Jung KH, Sohn CH, Moon J, Han MH, Roh JK. Middle cerebral artery plaque and prediction of the infarction pattern. *Arch Neurol* 2012;69(11):1470-5.



**Adapted from:**

**Van der Kolk AG**, Zwanenburg JJM, Brundel M, Biessels GJ, Visser F, Lijjten PR, Hendrikse J.  
*Distribution and natural course of intracranial vessel wall lesions in patients with ischemic stroke or TIA at 7.0 tesla MRI.* Submitted.

# Chapter 4

## **DISTRIBUTION & NATURAL COURSE OF VESSEL WALL LESIONS IN PATIENTS WITH TIA AND ISCHEMIC STROKE**

---

Anja G van der Kolk, MD<sup>1</sup>; Jaco JM Zwanenburg, PhD<sup>1,2</sup>; Manon Brundel, MD<sup>3</sup>;  
Geert Jan Biessels, MD PhD<sup>3</sup>; Fredy Visser<sup>1,4</sup>; Peter R Luijten, PhD<sup>1</sup>;  
Jeroen Hendrikse, MD PhD<sup>1</sup>

*From the <sup>1</sup>Department of Radiology, <sup>2</sup>Image Sciences Institute, and <sup>3</sup>Department of Neurology, University Medical Center Utrecht, The Netherlands; and <sup>4</sup>Philips Healthcare, Best, The Netherlands.*

# Key points

- » Previous studies using intracranial vessel wall MRI have shown vessel wall lesions in patients with varying cerebrovascular diseases.
- » Vessel wall imaging at 7T can provide information on the preferential location and natural course of these lesions.
- » Predilection locations in patients with ischemic stroke or TIA:
  - distal internal carotid artery
  - M1- and M2 segment of the middle cerebral artery
- » 17% of found lesions (one-third of patients) changed during follow-up, while most remained stable, indicating more generalized atherosclerosis.

## INTRODUCTION

In recent years, important steps have been made from imaging luminal stenosis of intracranial arteries towards imaging of atherosclerotic changes of the intracranial vessel walls with magnetic resonance imaging (MRI).<sup>1-9</sup> Most current intracranial vessel wall MRI sequences, mainly at a 3 tesla (T) field strength, allow characterization of vessel wall lesions, including enhancement, using several image contrast weightings and a high spatial resolution.<sup>1, 3-8</sup> However, they are hampered by a small field of view (FOV), limiting their use to assessment of single, predefined vessel wall lesions. In **Chapter 3**<sup>9</sup>, three 7T MRI sequences were introduced to image the intracranial arterial vessel walls.<sup>2, 9</sup> They have the advantage of larger FOVs compared to 3T sequences, enabling visualization of the main branches of the circle of Willis (CoW)<sup>2</sup> or even the whole brain<sup>9</sup> within one acquisition, enabling an overview of intracranial vessel wall lesions.

**“...limited data exists on the preferential location of intracranial vessel wall lesions that are detectable *in vivo*, or their potential changes over time...”**

Postmortem studies on both patients with fatal ischemic stroke as well as the general population have shown a substantial prevalence of atherosclerotic lesions in all areas of the intracranial arterial tree.<sup>10, 11</sup> The results from **Chapter 2**<sup>2</sup> also showed a high percentage (66%) of patients with ischemic stroke or transient ischemic attack (TIA) and vessel wall lesions in various branches of the CoW.<sup>2</sup> However, limited data exists on the preferential location of these intracranial vessel wall lesions that are detectable *in vivo*. Also, there is limited information on the potential changes of these lesions over time. In the study described in this chapter, distribution and natural course of intracranial vessel wall lesions within the intracranial arterial tree were assessed in patients with recent (transient) cerebral ischemic events, using intracranial arterial vessel wall imaging at 7T MRI one week and approximately one month after symptom onset.

## MATERIALS AND METHODS

### Study population

This study was approved by the Institutional Review Board of our hospital. All patients gave written informed consent. Between December 2009 and October 2012, consecutive patients who presented with arterial ischemic stroke or transient ischemic attack (TIA) of the anterior cerebral circulation at the neurology ward of our institution, were included in the intracranial vessel wall imaging (IVI) study (see **General introduction** NTR2119, [www.trialregister.nl](http://www.trialregister.nl)). Patients who were unable to undergo the MRI exam within one week due to their clinical condition, due to

contraindications for 7T MRI (claustrophobia, metallic objects in or on the body), or with a known allergic reaction to gadolinium contrast media or impaired renal function, were excluded from participation. 7T MR scanning was performed within one week of symptom onset; follow-up imaging was scheduled approximately one month after symptom onset, if patients were still willing to participate. Patient characteristics including age, gender, and general vascular risk factors were collected at baseline.

### MR imaging

Imaging was performed on a 7T whole body system (Philips Healthcare, Cleveland, OH, USA) with either a 16-channel or 32-channel receive coil and volume transmit/receive coil for transmission (Nova Medical, Wilmington, MA, USA). Until mid-July 2011, included patients were scanned with the limited-coverage  $T_1$ -weighted magnetization preparation inversion recovery turbo spin echo (MPIR-TSE) sequence.<sup>2</sup> During study enrollment, a whole-brain  $T_1$ -weighted MPIR-TSE sequence was developed<sup>9</sup>, and was applied in all patients included after mid-July 2011 instead of the limited-coverage MPIR-TSE sequence.

Scan parameters of the limited-coverage MPIR-TSE sequence have been described previously (**Chapter 2**)<sup>2</sup>; briefly, the following parameters were used: FOV 220 x 180 x 13 mm<sup>3</sup> in the transverse plane, acquired resolution 0.8 x 0.8 x 0.8 mm<sup>3</sup>, turbo spin echo (TSE) factor of 60, repetition time (TR) 6050 ms, inversion time (TI) 1770 ms, echo time (TE) 80 ms, equivalent TE 23 ms (the equivalent TE of the refocusing sweep reflects the TE that would yield similar contrast in case of full refocusing angles, for a given  $T_1$  and  $T_2$ ) number of signal averages (NSA) of 2, scan duration  $\approx$  12 minutes. Scan parameters of the whole-brain  $T_1$ -weighted MPIR-TSE sequence have also been described previously<sup>9</sup>; in short, the following scan parameters were used: FOV 250 x 250 x 190 mm<sup>3</sup> in the sagittal plane, acquired resolution 0.8 x 0.8 x 0.8 mm<sup>3</sup>, TSE factor of 158, TR/TI/TE 3952/1375/37 ms, equivalent TE 19 ms, NSA of 2, scan duration  $\approx$  11 minutes.

For confirmation of the vessel walls seen on the MPIR-TSE sequences, a 3-dimensional time-of-flight MR angiogram (TOF-MRA) by means of a fast field echo (FFE) sequence was obtained in all patients as part of the scan protocol. Scan parameters of the TOF-MRA were as follows: FOV 180 x 180 x 110 mm<sup>3</sup> in the transverse plane, acquired resolution 0.4 x 0.5 x 0.6 mm<sup>3</sup>, TR 22 ms, TE 2.5 ms, flip angle 25 degrees, receiver bandwidth 202 Hz/pixel, scan duration  $\approx$  10 minutes.

For possible vessel wall enhancement, 0.1 mL/kg body weight of a gadolinium-containing contrast agent (Gadobutrol, Gadovist 1.0 mmol/mL, Bayer Schering Pharma, Newbury, UK) was administered to all patients, and postcontrast vessel wall imaging was performed approximately 5 minutes after contrast injection.

### Offline processing

Scans were assessed individually on an offline workstation by two experienced observers (AK and JH), who were blinded for clinical data, and blinded for the MPR-TSE scan at the other time point when follow-up data was available. An intracranial vessel wall lesion was defined as either a clear local or more diffuse thickening of the vessel wall, often with hyperintense signal compared to the contralateral healthy vessel wall. For assessment of contrast enhancement of the vessel wall, co-registration by means of rigid registration<sup>12</sup> was performed, after which pre- and postcontrast images were subtracted and the subtraction image was assessed for contrast enhancement.<sup>2</sup> Contrast enhancement of the infundibulum was used to decide whether normal contrast enhancement had taken place. In case of differences between observers' scores, final scores were determined with mutual agreement. In case of differences between the 1-week and 1-month scan, both specific scans were assessed simultaneously to determine real changes versus scoring variability (resembling clinical practice).

## RESULTS

### Study population

Between December 2009 and October 2012, 62 patients were included in the study. Six patients were excluded from analysis: in 4 patients, motion artifacts made the data unsuitable for analysis; 1 patient was scanned with an incorrect version of the whole-brain T<sub>1</sub>-weighted MPR-TSE sequence that was not assessable; and for 1 patient the MPR-TSE sequence was performed after 1 month only. Thus, data from 56 patients were available for analysis (baseline data of 21 patients has been partly published in a technical study evaluating the limited-coverage MPR-TSE sequence<sup>2</sup>). Thirty-seven of these patients (66.1%) were scanned using the 16-channel and 19 patients (33.9%) using the 32-channel receive coil. Thirteen of 56 patients were scanned with the newly developed whole-brain T<sub>1</sub>-weighted MPR-TSE sequence (23.2%).

### Lesion distribution

Baseline imaging was available for 29 patients with initial symptoms of ischemic stroke, and 27 patients with initial symptoms of TIA (mean age, 59 years; range, 26 - 84 years). Mean time between symptom onset and baseline MRI scan was 5 days (range, 0 - 12 days). In 45 of 56 patients (80.4%), a total of 146 intracranial vessel wall lesions were found on the MPR-TSE images (**Table 1**), of which 105 (71.9%) lesions percentage were found in the anterior cerebral circulation and 41 (28.1%) lesions percentage in the posterior circulation. There was a slight predisposition for the right (61 of 105 lesions; 58.1%) as compared to the left anterior circulation

(44 of 105 lesions; 41.9%). Most lesions were located in the intracranial (distal or bifurcation) part of the internal carotid artery (ICA), and the M1- and M2 branches of the middle cerebral artery (MCA; **Table 1** and **Figure 1**). There were no significant differences in lesion distribution between patients with ischemic stroke or TIA.

### Follow-up lesion changes

In 39 of the 56 patients (69.6%), follow-up MPIR-TSE scans were available. In 3 of these patients, the follow-up scans were not assessable due to motion artifacts, leaving 36 patients (20 stroke / 19 TIA) for analysis. Mean time between symptom onset and follow-up MRI scan was 57 days (range, 23 - 207 days). 7 of the 36 patients (19.4%) had no intracranial vessel wall lesions on the 1-week MPIR-TSE images; none of these patients developed lesions during follow-up. In the remaining 29

**Table 1** Intracranial vessel wall lesion location at baseline in 56 patients with ischemic stroke or transient ischemic attack (TIA) of the anterior cerebral circulation

Location	Right*	Left*	Total (n=146)*
Internal carotid artery	29	22	51 (34.9)
<i>Distal intracranial segment</i>	16	7	23 (15.8)
<i>Intracranial bifurcation</i>	13	15	28 (19.2)
Middle cerebral artery	24	19	43 (29.5)
<i>M1 segment</i>	13	10	23 (15.8)
<i>Bifurcation</i>	2	1	3 (2.1)
<i>M2 segment</i>	7	8	15 (10.3)
<i>M3 segment†</i>	2	0	2 (1.4)
Anterior cerebral artery	8	3	11 (7.5)
<i>A1 segment</i>	7	3	10 (6.8)
<i>A2 segment</i>	1	0	1 (0.7)
Anterior communicating artery	-	-	0 (0.0)
Total anterior circulation lesions	61	44	105 (71.9)
Vertebral artery‡	2	6	8 (5.5)
Basilar artery	-	-	4 (2.7)
Basilar artery – bifurcation	-	-	6 (4.1)
Posterior cerebral artery	8	9	17 (11.6)
<i>P1 segment</i>	5	5	10 (6.8)
<i>Bifurcation</i>	3	1	4 (2.7)
<i>P2 segment</i>	0	3	3 (2.1)
Posterior communicating artery	3	3	6 (4.1)
Total posterior circulation lesions	13	18	41 (28.1)

A1 indicates primary branch of anterior cerebral artery (ACA); A2, secondary branch of ACA; M1, primary branch of middle cerebral artery (MCA); M2, secondary branch of MCA; M3, tertiary branch of MCA; P1, primary branch of posterior cerebral artery (PCA); P2, secondary branch of PCA.

\*Number of lesions at location (percentage of lesions)

†Based on a total of 7 stroke patients and 6 TIA patients, respectively, for whom a whole-brain magnetization preparation inversion recovery turbo spin echo (MPIR-TSE) sequence was available and the vertebral arteries and M3 segment of the MCA therefore assessable

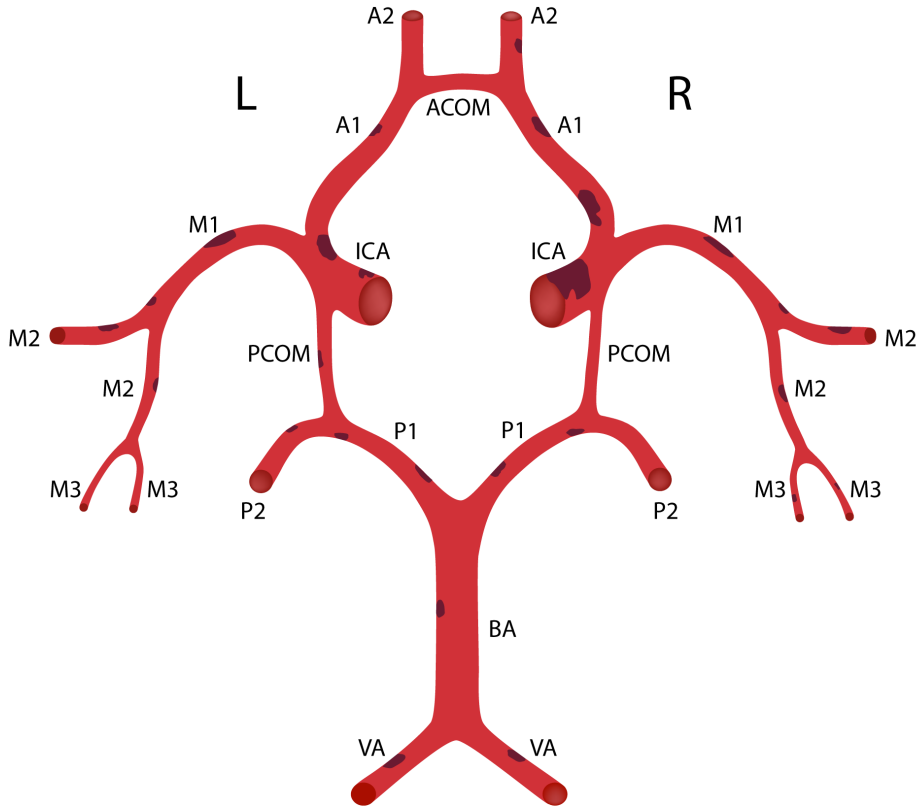


**Figure 1** Schematic drawing of the circle of Willis and its branches, with the burden of intracranial vessel wall lesions in the current study population illustrated by means of plaques; a larger plaque indicates a larger burden of lesions within the specific artery (see also **Table 1**). A1 indicates A1 segment of the anterior cerebral artery (ACA); A2, A2 segment of the ACA; ACOM, anterior communicating artery; BA, basilar artery; ICA, internal carotid artery; L, left; M1, M1 segment of the middle cerebral artery (MCA); M2, M2 segment of the MCA; M3, M3 segment of the MCA; P1, P1 segment of the posterior cerebral artery (PCA); P2, P2 segment of the PCA; PCOM, posterior communicating artery; R, right; VA, vertebral artery.

patients, 14 of a baseline total of 85 lesions (16.5%) in this group changed during follow-up (**Table 2**): 6 lesions resolved (**Figure 2** and **Figure 3**), 3 lesions showed new enhancement, 3 lesions lost enhancement (**Figure 3**), 1 lesion resolved on TOF-MRA, and one lesion showed a combination of the last two factors. The other 71 lesions (83.5%) showed no changes over time (**Figure 4**). On a patient level, 11 of 29 patients (4 stroke, 7 TIA; 30.6%) showed changes in one (8 patients) or more (3 patients) vessel wall lesions (**Table 2**). Two new lesions occurred, one in each of two patients with a TIA.

**Table 2** Overview of 11 patients with changes in intracranial vessel wall lesions during 1–month follow-up

Pt.	Age (y)	Sex (M/F)	FU period (days)	Final diagnosis*	Vessel wall lesions on MPIR-TSE†	
					1 week	1 month
3	75	F	80	Ischemic stroke left MCA territory (TOAST: Unknown 'Undetermined causes')	M1 L Gd+, <b>M2 L Gd+</b> (bif MCA not assessable)	M1 L Gd+, bif MCA L
12	76	F	34	TIA left MCA territory	<b>A1 R Gd+</b> , M2 L	<b>A1 R</b> , M2 L
16	76	M	207	Ischemic stroke left MCA territory (TOAST: Evident 'Cardioaortic embolism')	Dist ICA R, <b>bif ICA R</b> , M2 L (P1 not assessable)	Dist ICA R, <b>bif ICA R Gd+</b> , M2 L, P1 R, P1 L
18	38	F	38	TIA left MCA territory	P1 R, P1 L	P1 R, P1 L, <b>bif ICA R</b>
21	74	F	50	TIA right MCA territory	Bif ICA R, <b>M2 R Gd+</b> , M1 L MRA+	Bif ICA R, <b>M2 R</b> , M1 L (no MRA)
24	70	F	23	TIA right MCA territory	<b>M1 R MRA+</b> , bif MCA R MRA+, bif ICA L Gd+ MRA+	<b>M1 R Gd+ MRA+</b> , bif MCA R MRA+, bif ICA L Gd+ MRA+
26	49	F	53	Ischemic stroke several arterial territories (TOAST: Evident 'Other causes' → reversible vasoconstriction syndrome)	<b>P1 L MRA+</b>	-
29	45	F	56	TIA left MCA territory (Unknown vasculopathy)	<b>Bif ICA R Gd+ MRA+</b> , M1 L	<b>Bif ICA R (no contrast)</b> , M1 L
33	83	M	35	TIA right MCA territory	Bif ICA L Gd+, <b>M2 L</b> , basilaris Gd+, Bif P1P2 R Gd+	Bif ICA L, <b>Bif ICA R</b> , basilaris, Bif P1P2 R (all without contrast)
55	75	F	57	Ischemic stroke right MCA territory (TOAST: Evident 'Large artery atherosclerosis')	Dist ICA R Gd+ MRA+, bif ICA R, <b>M1 R Gd+ MRA+</b> , <b>M2 R Gd+ MRA+</b> , <b>M3 R MRA+</b> , vertebral L Gd+ (no MRA)	Dist ICA R Gd+ MRA+, bif ICA R, <b>M1 R</b> , vertebral L Gd+ (no MRA)
59	65	F	78	TIA left MCA territory	Dist ICA R Gd+, bif ICA R, M1 R, bif ICA L Gd+, M1 L Gd+, <b>M2 L Gd+</b> , <b>vertebral R (no MRA)</b> , vertebral L Gd+ (no MRA), bif P1P2 R Gd+, P1 L MRA+, <b>bif P1P2 L MRA+</b> , <b>bif P1P2 L Gd+ MRA+</b> , P2 L Gd+ MRA+	Dist ICA R Gd+, Bif ICA R, M1 R Gd+, bif ICA L Gd+, M1 L Gd+, <b>vertebral R Gd+ (no MRA)</b> , vertebral L Gd+ (no MRA), bif P1P2 R Gd+, P1 L MRA+, <b>bif P1P2 L MRA+</b> , P2 L Gd+ MRA+

A1 indicates A1 segment of anterior cerebral artery (ACA); bif, bifurcation; F, female; FU, follow-up; ICA, internal carotid artery; L, left; M, male; M1, M1 segment of MCA; M2, M2 branch of MCA; MCA, middle cerebral artery; P1, P1 segment of posterior cerebral artery (PCA); P2, P2 branch of PCA; Pt., patient; R, right; TIA, transient ischemic attack; vertebral, vertebral artery.

\*In case of ischemic stroke, the causative subtype was determined using the Stop Stroke Study Trial of Org 10172 in Acute Stroke Treatment (SSS-TOAST) classification criteria.<sup>19</sup>

†Lesions in **bold** were different between the 1-week and 1-month scans; Gd+ indicates lesions that showed enhancement after gadolinium-based contrast medium administration; MRA+ indicates lesions that were also visible on Time-of-Flight Magnetic Resonance Angiography (TOF-MRA).

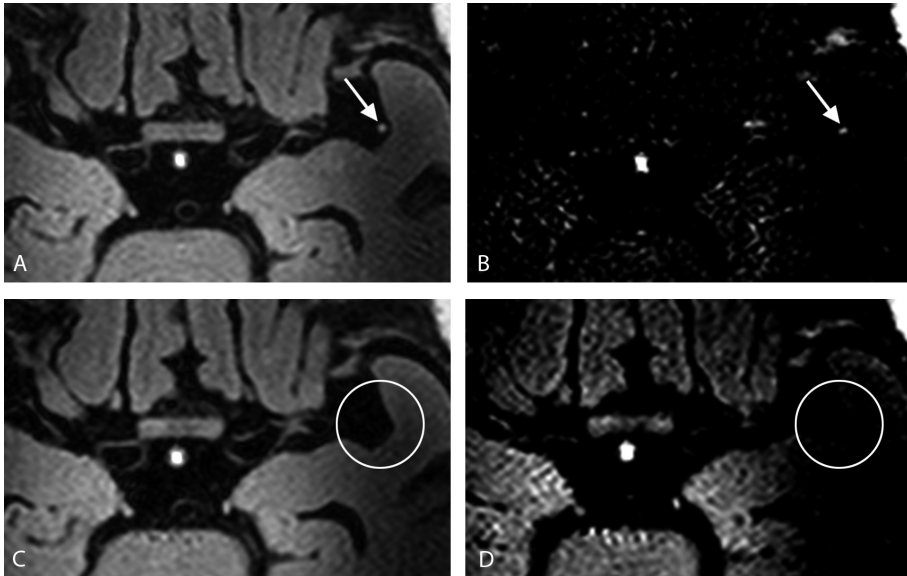


**Figure 2** A 75-year-old woman (no. 3 in **Table 2**) presented with mild-to-moderate aphasia based on ischemic stroke of the left MCA territory (this patient's initial scan has previously been presented as example of the technical capabilities of the 3D Magnetization-Preparation Inversion Recovery Turbo Spin Echo [MPIR-TSE] sequence<sup>2</sup>). (A, D) Transverse 7 tesla (7T) MPR-TSE images after contrast administration within 1 week (A) and during follow-up (C), with corresponding subtraction images (B, D). Within 1 week after symptom onset, a hyperintense lesion in the M2 segment of the left MCA was seen (arrow in A), with enhancement as confirmed on the corresponding subtraction image (arrow in B). At follow-up, 80 days after symptom onset, the lesion within the left M2 segment was neither seen on the contrast-enhanced MPR-TSE image (C) nor on the corresponding subtraction image (D).

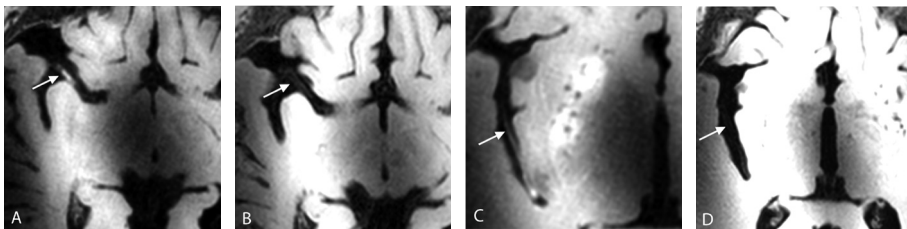


**Figure 3** A 75-year-old woman (no. 55 in **Table 2**) presented with left-side facial paresis and paresis of the left arm and leg based on ischemic stroke of the right MCA territory. (A-D) (A, C) Transverse 7T MPR-TSE images on different levels obtained within 1 week after symptom onset, showing irregular, hyperintense (and enhancing; not shown) lesions in the mid-M1 segment of the right MCA (arrow in A), which could be followed over a long trajectory into the M2 (arrow in C) and M3 segment of the MCA. At follow-up, 57 days after symptom onset, the hyperintense irregular lesion within the mid-M1 segment of the MCA on the MPR-TSE images had disappeared, leaving a slightly irregular, non-enhancing (not shown) vessel wall (arrow in B). Furthermore, resolution of the lesions within the M2- and M3 segment of the MCA has occurred (arrow in D), possibly reflecting the thromboembolic nature of these specific lesions. However, lesions within the distal ICA and ICA-M1 bifurcation remained visible at follow-up (not shown; see **Table 2**), which may suggest underlying atherosclerosis.

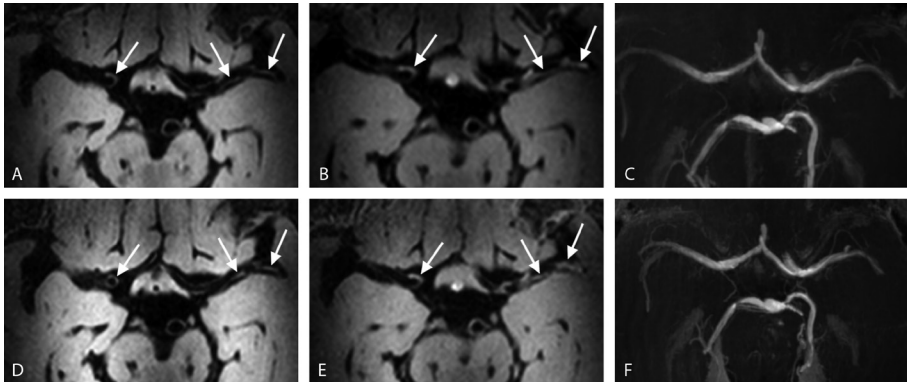


**Figure 4** A 65-year-old woman (no. 59 in **Table 2**) presented with transient mild-to-moderate sensory loss and mild-to-moderate aphasia based on a transient ischemic attack (TIA) of the left MCA territory. (A, B) Transverse 7T MPR-TSE images within 1 week after symptom onset show hyperintense, irregular and enhancing vessel wall lesions before (A) and after (B) contrast administration of the bilateral ICA bifurcation (*left two arrows* in A and B), and the M1- and M2 segment of the MCA on the left side (*right arrows* in A and B). On the corresponding time-of-flight MR angiography (TOF-MRA) image (C), no indication of vessel wall pathology can be seen. At follow-up, 78 days after symptom onset, both the vessel wall lesions on the whole-brain MPR-TSE images (*arrows* in D and E), as well as the absence of stenosis on the TOF-MRA (F), remain unchanged.

## DISCUSSION

In the current study, we assessed the preferential location and changes over time of intracranial arterial vessel wall lesions, as assessed using intracranial vessel wall imaging at 7T MRI. The most important findings are twofold. First, the majority of vessel wall lesions were found in the intracranial ICA (distal / bifurcation) and the M1- and M2 segments of the MCA. Second, a minority of 17% of lesions with follow-up showed a change in either presence or enhancement pattern; on a patient level, this occurred in about one-third of patients.

In our patient population, most lesions were found in either the intracranial (distal / bifurcation) ICA or the M1 segment of the MCA. Previous studies using

lumenography techniques for depiction of intracranial arterial stenosis showed similar results, with between 26-35% of patients with MCA stenosis and 6-26% of patients with intracranial ICA stenosis.<sup>13-16</sup>

**“...suggesting that not only shear stress plays a role in the pathogenesis of intracranial atherosclerosis...”**

The high prevalence of atherosclerotic

lesions in the distal ICA and its bifurcation may be explained by the fact that the vessel walls at these locations are subject to low shear stresses, due to the oscillatory disturbed flow, as has already been shown for arterial bifurcations

in other regions such as the extracranial ICA.<sup>17</sup> However, the second highest prevalence of atherosclerotic lesions was found for the M1- and M2 segment of the MCA, suggesting that not only shear stress plays a role in the pathogenesis of intracranial atherosclerosis.

The majority of intracranial arterial lesions was found in the anterior cerebral circulation relative to the posterior cerebral circulation, which is in accordance with the general distribution of cerebral ischemic infarcts.<sup>18</sup> Still, the percentage of patients with lesions found in the posterior circulation (42.9%) is relatively high when compared to the lower prevalence of ischemic events in the posterior cerebral circulation in general, especially since only patients with anterior cerebral circulation ischemic events were included in this study. It should also be noted that in a large proportion of our studied patients, only the distal basilar artery was visualized due to the limited coverage of our initial MPR-TSE sequence (**Chapter 2** and **Chapter 3**). Therefore, the prevalence of intracranial vessel wall lesions in the posterior cerebral circulation (including the distal vertebral arteries) may be even higher, as was seen in a previous postmortem study.<sup>10</sup>

**“...lesions were found to be relatively stable, indicating a more generalized atherosclerotic process...”**

In the current study, intracranial vessel wall lesions were detected in 80% of the patients with stroke or TIA. The question arises whether these lesions have clinical relevance, i.e. are they (potentially) unstable plaques with a risk of causing subsequent (transient) ischemic events, or indicative of more generalized atherosclerosis? It can be hypothesized that a change in presence and/or enhancement pattern of a vessel wall lesion may be indicative of a more active (culprit) lesion, a disappearing small thromboembolus (see **Figure 3**), or of a disappearing ‘fingerprint’ (remnant) of a thromboembolus that stranded at the specific location. However, because of the high prevalence of these lesions, they could also provide an indication of generalized atherosclerosis, which is often detected in arteries outside the brain, instead of being acute lesions. This latter may be supported by the fact that of all lesions with follow-up in our study, only 17% of lesions showed changes in presence and/or enhancement pattern, suggesting no direct relation with the current ischemic symptoms (non-culprit lesion) of the majority of lesions. However, long-lasting intracranial vessel wall ‘fingerprints’ of thromboembolic material in recanalized arteries cannot be excluded.

Interestingly, most changes in lesion status occurred in the patients with a TIA (7/11 patients). Still, no overall difference was found in lesion status in patients with ischemic stroke or TIA. Future studies with large patient groups are needed

to establish the potential relation between recurrent symptoms and changes over time in the burden and type of intracranial vessel wall lesions.

This study has some limitations. In the first series of patients, an MPIR-TSE sequence with a relatively limited coverage (**Chapter 2**), including only the CoW in the imaging volume, was used. Atherosclerotic lesions in the distal vertebral arteries and more peripherally located branches of the major intracranial arteries could therefore not be assessed for this patient subgroup. As mentioned before, this may have underestimated the atherosclerotic plaque burden, particularly in the posterior cerebral circulation and in the peripheral branches. However, this cannot completely account in the fact that postmortem studies show a much higher prevalence of intracranial atherosclerotic lesions, not only in the posterior

but also in parts of the anterior cerebral circulation<sup>10</sup>, suggesting that many atherosclerotic lesions are still outside the detection limit of our MRI sequences. Further, both the limited-coverage (**Chapter 2**) as well as the

**“...many atherosclerotic lesions are still outside the detection limit of our MRI sequences...”**

whole-brain MPIR-TSE sequence (**Chapter 3**) have a relatively long acquisition time of approximately 11 minutes, with a total of 22 minutes when pre- and postcontrast images are obtained. We feel that in the future, a more limited protocol with either pre- or postcontrast acquisition might be sufficient for evaluation of intracranial atherosclerotic plaque burden. This will also allow for additional sequences with different image contrast weightings (**Chapter 3**), enabling more detailed characterization of the atherosclerotic plaques.<sup>9</sup> Finally, technical comparison studies between 7T and lower field strength intracranial vessel wall MRI need to be performed, to allow for a comparison between the type of atherosclerotic lesions detected at different field strengths, enabling translation of the current findings to more widely available 3T and 1.5T MRI scanners.

In conclusion, the distal ICA and the M1- and M2 segment of the MCA were found to be predilection locations for the occurrence of intracranial vessel wall lesions. Only 17% of lesions (in one-third of patients) with follow-up showed changes in intracranial vessel wall lesion pattern; most lesions were found to be relatively stable, indicating a more generalized atherosclerotic process.

**REFERENCE LIST**

- (1) Park JK, Kim SH, Kim BS, Choi G, Jeong SY, Choi JC. Imaging of intracranial plaques with black-blood double inversion recovery MR imaging and CT. *J Neuroimaging* 2011;21(2):e64-e68.
- (2) van der Kolk AG, Zwanenburg JJ, Brundel M et al. Intracranial vessel wall imaging at 7.0-T MRI. *Stroke* 2011;42(9):2478-84.
- (3) Turan TN, Bonilha L, Morgan PS, Adams RJ, Chimowitz MI. Intraplaque hemorrhage in symptomatic intracranial atherosclerotic disease. *J Neuroimaging* 2011;21(2):e159-e161.
- (4) Xu WH, Li ML, Gao S et al. Plaque distribution of stenotic middle cerebral artery and its clinical relevance. *Stroke* 2011;42(10):2957-9.
- (5) Chung GH, Kwak HS, Hwang SB, Jin GY. High resolution MR imaging in patients with symptomatic middle cerebral artery stenosis. *Eur J Radiol* 2012;81(12):4069-74.
- (6) Kim YS, Lim SH, Oh KW et al. The advantage of high-resolution MRI in evaluating basilar plaques: a comparison study with MRA. *Atherosclerosis* 2012;224(2):411-6.
- (7) Lou X, Ma N, Ma L, Jiang WJ. Contrast-enhanced 3T high-resolution MR imaging in symptomatic atherosclerotic basilar artery stenosis. *AJNR Am J Neuroradiol* 2013;34(3):513-7.
- (8) Skarpathiotakis M, Mandell DM, Swartz RH, Tomlinson G, Mikulis DJ. Intracranial atherosclerotic plaque enhancement in patients with ischemic stroke. *AJNR Am J Neuroradiol* 2013;34(2):299-304.
- (9) van der Kolk AG, Hendrikse J, Brundel M et al. Multi-sequence whole-brain intracranial vessel wall imaging at 7.0 tesla. *Eur Radiol* 2013;23:2996-3004.
- (10) Mazighi M, Labreuche J, Gongora-Rivera F, Duyckaerts C, Hauw JJ, Amarenco P. Autopsy prevalence of intracranial atherosclerosis in patients with fatal stroke. *Stroke* 2008;39(4):1142-7.
- (11) Vink A, Schoneveld AH, Poppen M, de Kleijn DP, Borst C, Pasterkamp G. Morphometric and immunohistochemical characterization of the intimal layer throughout the arterial system of elderly humans. *J Anat* 2002;200(Pt 1):97-103.
- (12) Maes F, Collignon A, Vandermeulen D, Marchal G, Suetens P. Multimodality image registration by maximization of mutual information. *IEEE Trans Med Imaging* 1997;16(2):187-98.
- (13) Chimowitz MI, Kokkinos J, Strong J et al. The warfarin-aspirin symptomatic intracranial disease study. *Neurology* 1995;45(8):1488-93.
- (14) Mazighi M, Tanasescu R, Ducrocq X et al. Prospective study of symptomatic atherothrombotic intracranial stenoses: the GESICA study. *Neurology* 2006;66(8):1187-91.
- (15) Turan TN, Makki AA, Tsappidi S et al. Risk factors associated with severity and location of intracranial arterial stenosis. *Stroke* 2010;41(8):1636-40.
- (16) Pu Y, Liu L, Wang Y et al. Geographic and sex difference in the distribution of intracranial atherosclerosis in China. *Stroke* 2013;44(8):2109-14.
- (17) Cecchi E, Giglioli C, Valente S et al. Role of hemodynamic shear stress in cardiovascular disease. *Atherosclerosis* 2011;214(2):249-56.

## Part 2 – Chapter 4

- (18) Tao WD, Liu M, Fisher M et al. Posterior versus anterior circulation infarction: how different are the neurological deficits? *Stroke* 2012;43(8):2060-5.
- (19) Adams HP, Jr, Bendixen BH, Kappelle LJ et al. Classification of subtype of acute ischemic stroke. Definitions for use in a multicenter clinical trial. TOAST. Trial of Org 10172 in Acute Stroke Treatment. *Stroke* 1993;24(1):35-41.



**Adapted from:**

**Van der Kolk AG**, Zwanenburg JJM, Denswil NP, Vink A, Spliet WGM, Daemen MJAP, Visser F, Klomp DWJ, Lijten PR, Hendrikse J. ***Imaging the intracranial atherosclerotic vessel wall using 7.0 tesla MRI.*** Submitted.

# Chapter 5

## COMPARISON OF ULTRAHIGH-RESOLUTION INTRACRANIAL VESSEL WALL IMAGES WITH HISTOPATHOLOGY

---

Anja G van der Kolk, MD<sup>1</sup>; Jaco JM Zwanenburg, PhD<sup>1,2</sup>; Nerissa P Denswil, MSc<sup>3</sup>; Aryan Vink, MD PhD<sup>4</sup>; Wim GM Spliet, MD<sup>4</sup>; Mat JAP Daemen, MD PhD<sup>3</sup>; Fredy Visser<sup>1,5</sup>; Dennis WJ Klomp, PhD<sup>1</sup>; Peter R Luijten, PhD<sup>1</sup>; Jeroen Hendrikse, MD PhD<sup>1</sup>

*From the <sup>1</sup>Department of Radiology, <sup>2</sup>Image Sciences Institute, and <sup>4</sup>Department of Pathology, University Medical Center Utrecht, the Netherlands; the <sup>3</sup>Department of Pathology, Academic Medical Center Amsterdam, The Netherlands; and <sup>5</sup>Philips Healthcare, Best, The Netherlands*

# Key points

- » Compared with carotid atherosclerosis, validation of intracranial vessel wall MRI with histology has not yet been performed.
- » The question arises whether MRI has enough image contrast to visualize *intracranial* atherosclerotic plaque components.
- » Comparison of *ex vivo* imaging and histology of CoW samples shows ability of multicontrast ultrahigh-resolution 7T MRI to:
  - Identify focal wall thickening corresponding with advanced atherosclerotic lesions
  - Distinguish areas of different signal intensities, spatially corresponding with plaque components
- » Areas of foamy macrophages were mostly seen as hypointense areas on PD-,  $T_2$ - and  $T_2^*$ -weighted images.
- » Areas of increased collagen content showed ambiguous signal intensities, ranging from hypo- to hyperintense on all sequences.
- » Additional studies should quantitatively validate signal characteristics of the specific intracranial atherosclerotic plaque components.

## INTRODUCTION

In recent years, several magnetic resonance imaging (MRI) sequences have been developed on 3 and 7 tesla (T) field strength that specifically visualize intracranial arterial vessel wall pathology (**Chapter 2** and **Chapter 3**)<sup>1-7</sup>. Similar to carotid artery atherosclerosis, several studies have recently attempted to characterize intracranial plaque components using MRI, like intraplaque hemorrhage<sup>8,9</sup>, fibrous cap<sup>10</sup> and lipid components<sup>11,12</sup>. For the carotid arteries, much research has already been done validating image signal heterogeneity within the vessel wall with histology, the gold standard<sup>13-19</sup>. Imaging carotid artery atherosclerosis has the advantage of 'easy' access to *ex vivo* atherosclerotic plaque material for validation, using carotid endarterectomy specimens. It is now possible to image calcification, fibrous cap, intraplaque hemorrhage and lipid-rich necrotic core in the carotid artery with moderate to good sensitivity and specificity using multicontrast-MRI<sup>18</sup>. Although one recent study showed promising preliminary results of plaque characterization using a combined T<sub>1</sub>- and T<sub>2</sub>-weighted sequence<sup>20</sup> compared with histology, dedicated validation with histology of intracranial vessel wall sequences with multiple image contrast weightings has not yet been performed. Therefore, the question remains whether MRI with multiple image contrast weightings has enough image contrast to visualize various intracranial atherosclerotic plaque components as well.

**"...validation of MR images with histology for intracranial atherosclerosis *in vivo* is much more cumbersome compared with carotid plaques..."**

Validation of MR images with histology for intracranial atherosclerosis *in vivo* is much more cumbersome compared with carotid plaques, since no therapies (comparable to carotid endarterectomy) exist in which intracranial atherosclerotic plaques are removed. Furthermore, intracranial arteries are smaller than carotid (or other major peripheral) arteries<sup>21</sup>, necessitating a high spatial resolution, and therefore high signal-to-noise ratio (SNR), for plaque visualization. Since the SNR increases approximately linearly with field strength (**Chapter 1**), 7T MRI might provide the spatial resolution necessary to image small atherosclerotic plaques<sup>21</sup>. Furthermore, several dedicated intracranial vessel wall sequences at 7T (**Chapter 2** and **Chapter 3** and **Chapter 4**) have already shown promising results in the visualization of vessel wall lesions *in vivo*.<sup>4,7</sup> In the feasibility study described in this chapter, ultrahigh-resolution 7T MRI sequences with different image contrast weightings were developed and used in an *ex vivo* setting, to assess the ability (image contrast) of 7T MRI to image different intracranial atherosclerotic plaque components. For validation of our findings, results were compared with histology (gold standard).

## **MATERIALS AND METHODS**

### **Specimen preparation**

Five specimens of the circle of Willis (CoW) were selected from > 100 autopsy cases that were performed in our hospital. Material was handled in a coded way that met the criteria of the Code of conduct for responsible use of human tissue that is used in The Netherlands for the use of human tissue in medical research ([www.federa.org](http://www.federa.org)). The sole selection criterion was the macroscopic presence of atherosclerosis as judged by an experienced pathologist (AV). Care was taken that the specimens included the major arteries of the CoW. All specimens had been stored in formaldehyde. After selection, the specimens were cleaned thoroughly with a lukewarm solution of 0.5% Tween-20 (Tween 20, Sigma Aldrich, Missouri, USA) dissolved in Aquadest (Aquadest Laboratory Water) to remove blood clots within the arterial vessel lumen, reducing the chance of artifacts on MR imaging. The specimens were then individually placed within a 9.5 cm round Petri dish, and embedded in a 2% agarose solution (Seakem LE Agarose, Lonza, Rockland, ME, USA). During immersion in the agarose solution, care was taken to remove all air from the specimens. The embedded specimens were stored in a refrigerator at a temperature of 5 °C for solidification until imaging could be performed.

To enable spatial correlation of the MR images with histological slices, cactus spines were used as fiducials and placed in the agarose gel, adjacent to 13 locations of histological sampling. The 13 locations (see **Figure 1**) included, when possible (if no air within artery), all the major arteries of the CoW (vertebral arteries [VA], basilar artery [BA; 3 different levels], posterior cerebral arteries [PCA], distal internal carotid arteries [ICA], middle cerebral arteries [MCA], and anterior cerebral arteries [ACA]).

### **MR imaging protocol**

Imaging was performed on a 7T whole body system (Philips Healthcare, Cleveland, OH, USA) with two 16-channel dedicated surface coils (MR Coils BV, Drunen, the Netherlands) above and below the specimens for signal reception<sup>22</sup>, and a volume transmit/receive coil for transmission (Nova Medical, Wilmington, MA, USA). Two specimens could be imaged at one time. The specimens – within their Petri dish – were placed on top of each other in the middle of a thin plastic container, using plastic filling above and below. The container was then filled with fomblin (Solvay Solexis, Bollate, Italy) until the specimens were completely submerged, to provide susceptibility matching. The two 16-channel surface coils were placed above and below the filled box, after which the whole package was placed inside the volume transmit/receive coil.

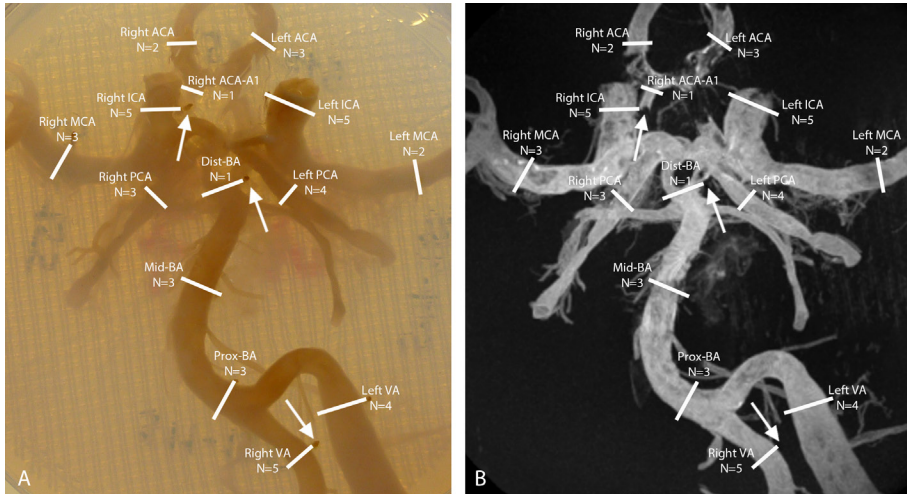


**Figure 1** A, Photograph and B, maximum intensity projection of the 7 tesla (T)  $T_1$ -weighted turbo field echo magnetic resonance imaging (MRI) sequence of the circle of Willis (CoW) specimen of a 87-year-old man, embedded in a 2% agarose solution within a petri dish. The sample locations are illustrated by white lines. For each sample location, care was taken to avoid sampling near a visible air bubble, or sampling of a collapsed arterial segment. The N below each arterial segment denotes the number of samples for that location within the 44 assessed samples obtained from the five CoW specimen. MR images were correlated with histologic slices using fiducials placed within the agarose solution (**arrows** in **A** and **B**). A1 indicates A1 segment of anterior cerebral artery (ACA); BA, basilar artery; dist-BA, distal segment of the BA; ICA, internal carotid artery; MCA, middle cerebral artery; mid-BA, middle segment of the BA; PCA, posterior cerebral artery; prox-BA, proximal segment of the BA; VA, vertebral artery.

Imaging was performed at room temperature. For imaging, sequences with four different contrast weightings were used, resembling previous MRI-histology correlation studies in the proximal ICA. Parameters of the four sequences can be found in **Table 1**. After a 3-dimensional (3D)  $T_1$ -weighted turbo field echo ( $T_1$ -TFE) sequence with full-specimen coverage was applied, a single-slice proton density spin echo (PD-SE)-, a single-slice  $T_2$ -weighted turbo spin echo ( $T_2$ -TSE)- and a single-slice  $T_2^*$ -weighted TFE ( $T_2^*$ -TFE) sequence with identical geometrical parameters were performed for each of the 13 marked locations (resulting in one slice per image contrast per sample location), using the  $T_1$ -weighted images for planning. The PD-SE- and  $T_2$ -TSE sequences included an inversion pulse to null the signal from the agarose gel, similar to cerebrospinal fluid suppression in a fluid attenuated inversion recovery sequence. The inversion delay of 1100 ms was regarded long enough to limit the amount of  $T_1$  weighting in the vessel wall, which has a shorter  $T_1$  *ex vivo* (approximately 300 ms; data not shown). The total scan duration for each CoW specimen was approximately 40.5 hours. To compensate for potential frequency drifts due to the long sequence durations, frequency navigators were used.

**Table 1** Scan parameters of the four used 7 tesla (T) MRI sequences

Parameter	T <sub>1</sub> -TFE	PD-SE	T <sub>2</sub> -TSE	T <sub>2</sub> *-TFE
FOV (mm <sup>3</sup> )	110 x 110 x 34	120 x 40 x 1	120 x 40 x 1	120 x 40 x 1
Acq. Res. (mm <sup>3</sup> )	0.11 x 0.11 x 0.11	0.11 x 0.11 x 1	0.11 x 0.11 x 1	0.11 x 0.11 x 1
TR/TI/TE (ms)	55 / - / 6.0	3500 / 1100 / 12	3500 / 1100 / 51	24 / - / 15
Flip angle (°)	25	90	90	90
TSE/TFE factor	1000	-	7	1
NSA	1	2	22	3
T (hr:min:sec)	3:39:22	0:42:28	1:05:34	1:03:29

Acq. Res. indicates acquired resolution; FOV, field of view; hr, hours; min, minutes; NSA, number of signal averages; PD, proton density; sec, seconds; T, time (duration); TE, echo time; TFE, turbo field echo; TI, inversion time (used to null the gel signal); TR, repetition time; TSE, turbo spin echo.

For the PD-SE and T<sub>2</sub>-TSE, the non-selective frequency navigators were applied just prior to excitation and used to adjust the system frequency accordingly. For the T<sub>2</sub>\*-TFE sequence, a navigator echo was used, as described previously.<sup>23</sup>

### Histologic processing

Histologic processing was performed using an in-house developed protocol. After imaging was performed, approximately 0.5 cm thick tissue samples were taken from the 13 marked locations of each CoW specimen. Ink markings were then used to enable correlation of histological slices and MR images: black ink was used to mark the sample side next to the fiducial, while blue ink was used to mark the cranial side of the sample with respect to the Petri dish. The tissue samples, placed within small plastic containers with 6 spaces, were then placed in ethylenediaminetetraacetic acid (EDTA 12.5%) for 3-4 days to dissolve wall calcifications, to reduce the risk of damaging the samples during slicing. After processing and embedding in paraffin, the samples were cut into 4 µm sections and stained with hematoxylin-eosin (HE) and elastic van gieson (EvG) stain, and assessed using a slide scanner (Olympus slide scanner, Dotlide software version 2.5, Tokyo, Japan). The modified American Heart Association classification by Virmani et al.<sup>24</sup> was used to classify each sample on atherosclerotic characteristics, as follows: no anomaly; early lesions, including intimal thickening (IT; < 50% smooth muscle cells, no lipids, inflammatory cells), fatty streak (FS) and pathological intimal thickening (PIT; > 50% smooth muscle cells, rich in proteoglycans, foamy macrophages); and advanced lesions, including fibrolipid plaque (FL; > 40% lipid), thin cap atheroma (TCA; < 65 µm thickness), fibrous plaque (F; < 40% lipid), fibrocalcified plaque (FC; > 40% calcified) and calcified nodule (CN; calcified element protruding the intima). When applicable, plaque complications – rupture, hemorrhage or erosion – were also assessed.

### **Correlation of MR images with histology**

First,  $T_1$ -weighted images were reconstructed (0.11 mm thickness) for each sample, corresponding to the orientation and location of the PD-,  $T_2$ - and  $T_2^*$ -weighted images at each of the 13 locations marked by the fiducials. Then, the MR images were compared with the histological slices at the corresponding location. If the MR images did not match with the corresponding histological slice – due to errors in MR planning or gross deformation of the sample during histologic processing – the sample was excluded from analysis. Some deformation of the samples is inevitable; however, when no correlation in shape could be identified even when ink locations were used as additional spatial markers, the sample was excluded. Samples were also excluded from analysis in case of histologic processing errors (mixed-up / damaged / parallel (instead of perpendicular) cut samples). The resulting MRI-histology sets were then evaluated for (dis)agreement between plaque components and image contrast differences. First, MR images were assessed by AK for the presence of image contrast heterogeneity within the arterial vessel wall for each sample; then, the corresponding areas on the histological slices were assessed by ND for possible atherosclerotic changes that could explain the image contrast heterogeneity seen on the MR images. When no vessel wall atherosclerosis was present, heterogeneities on MRI were scored as ‘no correlation’. When atherosclerosis was present in the same area, the spatial organization of plaque components (e.g., collagen-rich rim, areas of foamy macrophages) was compared with the spatial organization of the vessel wall MR heterogeneities, scoring either ‘no correlation’ or a correlation which was then described more specifically. Finally, samples in which no MR heterogeneity was found, but where atherosclerotic changes were present, were also described. Since this was a feasibility study assessing the ability of 7T MRI of providing sufficient image contrast for visualizing intracranial atherosclerotic plaques and characterizing its components, blinding was not performed.

## **RESULTS**

### **Sample population**

Five CoW specimens from three man aged 54, 71 and 87 years and two women aged 65 and 74 years were used; a total of 65 samples of CoW arteries were obtained. Twenty-one of these 65 samples (32.3%) were excluded, due to either lack of correlation in shape or fiducial location (n=11), air within the sample which was not seen during MR planning (n=1), or due to histological processing errors (mixed-up / damaged / parallel (instead of perpendicular) cut samples; n=9), resulting in a total of 44 samples for assessment. **Figure 1** illustrates the sample locations, as well as the number of samples obtained at each location.

### Histological classification

Five samples (11.4%) had no atherosclerosis; 31 samples (70.4%) contained early atherosclerotic lesions: 24 samples showed intimal thickening (IT), 4 samples showed a fatty streak (FS), and 3 samples showed pathological intimal thickening (PIT). The remaining 8 samples (18.2%) showed either fibrous plaques (n=7, F) or a fibrolipid plaque (n=1, FL). No fibrocalcific plaques, calcified nodules or thin cap atheroma were seen; also, no plaque complications like rupture, (intraplaque) hemorrhage or erosion were found.

### MR image contrast heterogeneity

Twenty-three of 44 samples (52.3%) showed no image contrast heterogeneity on either of the four MR image contrast weightings ( $T_1$ -, PD-,  $T_2$ - or  $T_2^*$ -weightings; **Figure 2** and **Figure 3**). Samples within this group comprised solely of none or early lesions: 5 samples had no atherosclerosis, the other 18 showed intimal thickening (**Figure 3**). In 21 of 44 samples (47.7%), various patterns of image contrast heterogeneity were found (**Figure 2** and **Table 2**). Eleven samples (25.0%; **Figure 4**) showed good correlation between the spatial organization of vessel wall MR heterogeneities (areas of decreased or increased signal intensity) and the spatial organization of plaque components (e.g., collagen-rich rim, areas of foamy macrophages). These 11 samples comprised of 8 advanced lesions (7 fibrous plaques, 1 fibrolipid plaque) and 3 samples with pathological intimal thickening (last stage of early lesions). Within these samples, areas of foamy macrophages and proteoglycans, or areas with high levels of lipids, were most often (8 of 9 plaques with these characteristics) seen as hypointense areas within the vessel wall on the PD-,  $T_2$ - and  $T_2^*$ -weighted sequences (**Figure 4**); one sample with foamy macrophages showed a hyperintense

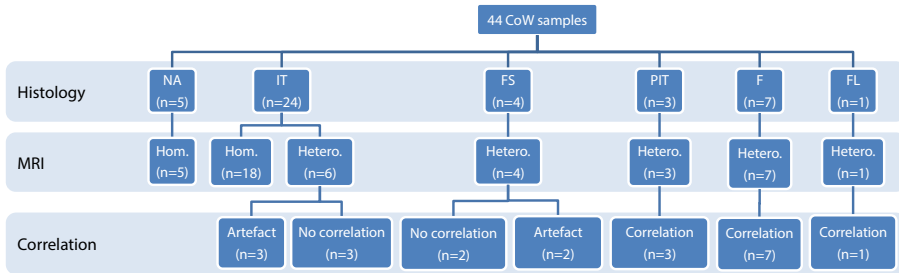


**Figure 2.** Overview of histological classification and the presence of vessel wall heterogeneity on MRI of the 44 samples of the CoW, including correlation scoring. Artefact indicates intima-media artefact; F, fibrous plaque; FL, fibrolipid plaque; FS, fatty streak; Hom., vessel wall with homogeneous signal intensity; Hetero., vessel wall with heterogeneous signal intensity; IT, intimal thickening; NA, no anomaly (no atherosclerosis); PIT, pathological intimal thickening.

signal on all sequences used (distal basilar artery in 71-year-old man; **Table 2**). Areas of increased collagen content (present in all 11 plaques) showed more ambiguous signal intensities: five samples showed corresponding hyperintense areas on at least  $T_2$ - and  $T_2^*$ -weighted images (**Figure 4, case 1-3**), with isointense to hyperintense signal on the  $T_1$ - and PD-weighted images, while five samples showed an hypointense signal for these areas on the  $T_2$ - and  $T_2^*$ -weighted images (**Figure 4, case 4**), with various signal intensities on the  $T_1$ - and PD-weighted images. In one sample, the collagen-rich area could only be distinguished from healthy vessel wall because of the adjacent hypointense area of foamy macrophages. Five other samples (three with intimal thickening and two with fatty streak; 11.4%) showed image contrast heterogeneity on MR images, without corresponding plaque components on histological slices (**Figure 5**).

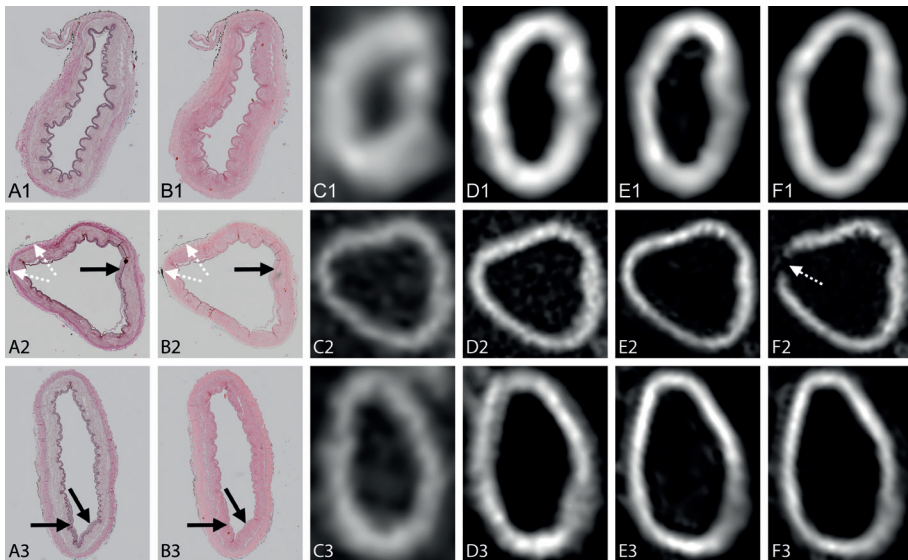


**Figure 3.** Three examples of no or early lesions without signal heterogeneity on 7T MR images. Histologic slices with elastic van gieson (EvG) (A) and hematoxylin-eosin (HE) (B) staining, with corresponding 7T MR images of the  $T_1$ -weighted (C), proton density (PD)-weighted (D),  $T_2$ -weighted (E) and  $T_2^*$ -weighted (F) sequences.

**Case 1:** Cross-section of the left PCA of a 65-year-old woman. Histologic examination showed no anomalies, which was reflected in a homogeneous signal intensity throughout the whole vessel wall on all sequences.

**Case 2:** Cross-section of the right MCA of a 71-year-old man. Histologic examination showed intimal thickening (*black arrow* in A2 and B2), which was not seen as signal heterogeneity of the vessel wall on the MR images. An artefact from the fiducial can be seen on the  $T_2^*$ -weighted image (F2), corresponding to black ink on the histological slices (*dashed white arrows* in A2 and B2).

**Case 3:** Cross-section of the left VA of a 54-year-old man. Histologic examination showed intimal thickening (*black arrows* in A3 and B3), which was not seen as signal heterogeneity of the vessel wall on the MR images.

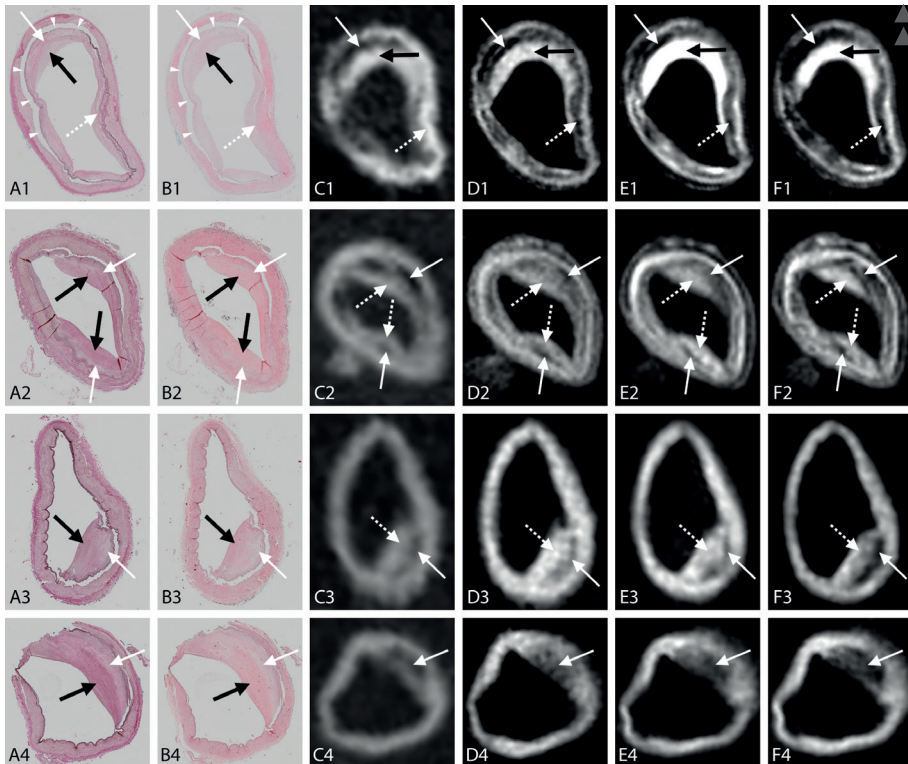


**Figure 4.** Four examples of atherosclerotic plaques with corresponding signal heterogeneity on 7T MR images. Histological slices with EvG (A) and HE (B) staining, with corresponding 7T MR images of the  $T_1$ -weighted (C), PD-weighted (D),  $T_2$ -weighted (E) and  $T_2^*$ -weighted (F) sequences.

**Case 1:** Cross-section of the left ICA of a 87-year-old man. Histologic examination showed a fibrous plaque with proteoglycans (*white arrow* in A1 and B1) and increased collagen (*black arrow* in A1 and B1); a small patch of foamy macrophages could also be appreciated (*dashed white arrow* in A1 and B1). On the corresponding MR images, the rim of increased collagen can be seen as a hyperintense inner rim on all sequences (*black arrow* in C1-F1), while the small patch of foamy macrophages corresponds with a hypointense area within the vessel wall (*dashed arrow* in C1-F1). Due to the intima-media artefact, a distinction between artefact (*arrowheads* in A1 and B1) and proteoglycans lining the artefact within the hypointense area on MRI (*white arrow* in C1-F1) could not be made.

**Case 2:** Cross-section of the right VA of a 71-year-old man. Histologic examination showed a fibrous plaque with increasing collagen from outside (*white arrows* in A2 and B2) to inside (*black arrows* in A2 and B2); on the corresponding MR images, the area with more strongly increased collagen appears as a mostly hyperintense inner area (*dashed white arrows* in C2-F2), while the area with less collagen appears iso- to hypointense (*white arrows* in C2-F2).

**Case 3:** Cross-section of the right ICA of a 71-year-old man. Histologic examination showed pathological intimal thickening (PIT) with proteoglycans and foamy macrophages (*white arrow* in A3 and B3), as well as increased collagen (*black arrow* in A3 and B3; not enough for fibrous plaque); again, the collagen-rich inner area appears isointense on the MR images (*dashed white arrow* in C3-F3), while the area with proteoglycans and foamy macrophages appears mostly hypointense (*white arrow* in C3-F3).

**Case 4:** Cross-section of the left ICA of a 71-year-old man. Histological examination showed a fibrous plaque with a thick inner rim of increased collagen (*black arrow* in A4 and B4), as well as a thick outer rim with foamy macrophages (*white arrow* in A4 and B4); in this case, the vessel wall thickening on MRI has a hypointense signal, corresponding with both an area of foamy macrophages as well as an inner rim of increased collagen (*white arrow* in C4-F4).

**Table 2** Overview of image contrast heterogeneity within the vessel wall on 7T MRI, and its correlation with histology

Subject*	Artery†	Heterogeneity on MRI	Signal intensity‡				Class.§	Correlation MRI versus histology
			T <sub>1</sub>	PD	T <sub>2</sub>	T <sub>2</sub> *¶		
♂, 87	RVA	Focal 'spot' within wall	↓	↓	↓	↓	IT	Intima-media artefact
	Mid-BA	Local inner rim	=	=	↓	↓	FS	No correlation
	R MCA	Line within wall (almost circumf.)	↓	↓	↓	↓	F	Intima-media artefact / foamy macrophages
		Inner rim (almost circumf.)	=	=	↑	↑	F	Increased collagen
	L MCA	Thickening ('core')	↓	↓	⇒/↓	⇒/↓	FL	Lipid core
		Inner rim	⇒/↑	↑	↑	↑	FL	Increased collagen
	R ICA	Thin local line within wall	↓	↓	↓	↓	F	Intima-media artefact / foamy macrophages
		Local thickening	↑	⇒/↑	↑	↑	F	No correlation
		Local area	↓	⇒/↓	⇒/↓	↓	F	Foamy macrophages
	L ICA	Thick local inner rim	=	↑	↑	↑	F	Increased collagen
		Line within wall (almost circumf.)	↓	↓	↓	↓	F	Intima-media artefact
		Local area	⇒/↑	↓	↓	↓	F	Foamy macrophages
♀, 74	RVA	Local lines within wall	=	↓	↓	↓	FS	Intima-media artefact / foamy macrophages
	Prox-BA	Focal line within wall	=	↓	↓	↓	IT	Intima-media artefact
	R PCA	Local line within wall	=	↓	↓	↓	FS	Intima-media artefact
		Inner rim	↑	↑	↑	↑	FS	No correlation
	L PCA	Patchy 'spots' within wall	=	↓	↓	↓	IT	Intima-media artefact
		Focal inner rim 'spots'	=	=	↑	↑	IT	No correlation
	L MCA	Thickening ('core')	↓	↓	↓	↓	PIT	Foamy macrophages & proteoglycans
		Inner rim	=	↑	↑	↑	PIT	Increased collagen
	R ICA	Local line within wall	⇒/↑	⇒/↑	↓	↓	F	Intima-media artefact
		Focal inner rim 'spots'	=	↑	↓	↓	F	Increased collagen
	L ICA	Line within wall	=	↓	↓	↓	IT	Intima-media artefact
	♀, 65	Prox-BA	Lines within wall	=	↓	↓	↓	FS
Mid-BA		Patchy 'spots' within wall	↑	↑	⇒/↑	⇒/↑	IT	No correlation
♂, 54	L ICA	Local line within wall	=	↓	↓	↓	IT	No correlation
		Focal inner 'spot'	↑	↑	↑	↑	IT	No correlation

Table 2 continued I

Subject*	Artery†	Heterogeneity on MRI	Signal intensity‡				Class.§	Correlation MRI versus histology
			T <sub>1</sub>	PD	T <sub>2</sub>	T <sub>2</sub> *		
♂, 71	RVA	Thickening ('core') 2 locations	↓	=	=	↓	F	Less collagen / artefact
		Thick local inner rim 2 locations	=	=	↑	↑	F	Increased collagen
	LVA	Local line within wall	↓	↓	↓	↓	F	Foamy macrophages
		Focal inner area	↑	↓	↓	↓	F	Increased collagen
	Dist-BA	Focal protruding thickening	↑	↑	↑	↑	PIT	Foamy macrophages & proteoglycans
	R ICA	Thickening ('core')	↓	↓	↓	↓	PIT	Foamy macrophages & proteoglycans
		Local inner rim	=	=	=	=	PIT	Increased collagen
	L ICA	Large thickened area	↓	↓	↓	↓	F	Foamy macrophages
		Thin inner rim	↑	↓	↓	↓	F	Increased collagen

Circumf. indicates circumferential.

\* Gender and age at death of the 5 subjects from whom Circle of Willis specimens were used in this study.

† Mid-BA indicates middle part of basilar artery; R, right; L, left; MCA, middle cerebral artery; ICA, (distal) internal carotid artery; VA, vertebral artery; PCA, posterior cerebral artery; prox-BA, proximal part of basilar artery; dist-BA, distal part of basilar artery

‡ Signal intensity of the described vessel wall lesion on each of the four image contrast weightings; =, isointense to surrounding healthy vessel wall; ↓, hypointense to surrounding healthy vessel wall; ↑, hyperintense to surrounding healthy vessel wall.

§ Classification according to the modified American Heart Association classification by Virmani et al.<sup>24</sup>; F indicates fibrous plaque; FL, fibrolipid plaque; FS, fatty streak; IT, intimal thickening; PIT, pathological intimal thickening.

Eleven samples (25.0%; five with no other signal heterogeneity, **Figure 5**) showed a hypointense line within the vessel wall on the PD-, T<sub>2</sub>- and T<sub>2</sub>\*-weighted images, which was isointense on the T<sub>1</sub>-weighted images. Though this hypointensity corresponded with a space between the intima and media of the arterial wall on the histological slices, it was regarded as an artefact of the specimen because of either detachment of the intima (e.g., due to prolonged storage), or because of cleaning of the specimens (flushing arteries with water / careful removal of blood clots). Due to this intima-media artefact, a distinction between artefact and proteoglycans / foamy macrophages lining the artefact within the hypointense area on MRI was sometimes difficult to make (**Figure 4, case 1**).

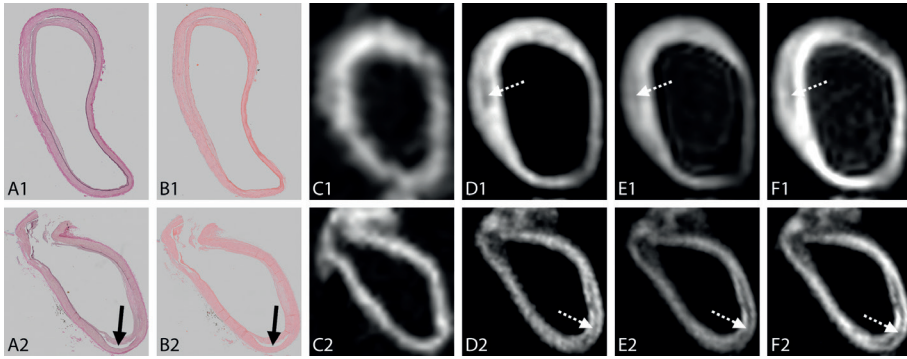


**Figure 5.** Two examples of discrepancies between 7T MRI and histology. Histologic slices with EvG (A) and HE (B) staining, with corresponding 7T MR images of the  $T_1$ -weighted (C), PD-weighted (D),  $T_2$ -weighted (E) and  $T_2^*$ -weighted (F) sequences.

**Case 1:** Cross-section of the right PCA of a 74-year-old woman. Histologic examination showed a fatty streak (FS), which was not seen as signal heterogeneity of the vessel wall on the MR images. A hypointense area away from the fatty streak could be appreciated on the MR images (arrow in D1-F1), but this did not correspond with any vessel wall pathology on histology, apart from intima-media artefact.

**Case 2:** Cross-section of the left ICA of a 74-year-old woman. Histologic examination showed minor intimal thickening; on the PD-,  $T_2$ - and  $T_2^*$ -weighted MR images, a hypointense line could be seen within a large part of the vessel wall (*dashed white arrow* in D2-F2), which corresponded to an intima-media artefact on the histological slices (*black arrow* in A2 and B2).

## DISCUSSION

In the present study we assessed the feasibility of 7T MRI to characterize *ex vivo* intracranial atherosclerotic plaques with sufficient image contrast, using ultrahigh-resolution sequences with four different image contrast weightings. Areas of focal arterial vessel wall thickening on ultrahigh-resolution MR images corresponded with histologically determined advanced atherosclerotic lesions. In all of these more advanced lesions, signal heterogeneities on 7T MRI enabled the spatial differentiation between different plaque components, like foamy macrophages and collagen. In early lesions, no signal intensity heterogeneity could be observed.

Using 7T MRI with dedicated surface coils made it possible to image the intracranial arterial vessel wall *ex vivo* with an acquired in-plane resolution of  $0.11 \times 0.11 \text{ mm}^2$ . For the  $T_1$ -TFE sequence, the images could be reconstructed in all directions using 3D image acquisitions of  $0.11 \times 0.11 \times 0.11 \text{ mm}^3$ . With this high spatial resolution, conspicuousness of the intracranial arterial vessel wall and its pathology could be obtained, although some problems of *ex vivo* imaging remain,

**“...in more advanced lesions, signal heterogeneities on 7T MRI enabled the spatial differentiation between different plaque components, like foamy macrophages and collagen...”**

such as removal of all air from the arterial lumen that gives rise to image artifacts. An initial comparison was performed with histologic classification at specific arterial locations, similar to carotid plaque characterization studies.<sup>25</sup> Of the 44 arterial samples that were assessed in this study, correlation between MRI and histology was shown to be best in the samples with more advanced lesions. None of the 5 samples with healthy arterial vessel walls showed areas of signal hypo- or hyperintensity on MR images. This was also true for 18 of 24 samples (75%) with intimal thickening, suggesting that these early atherosclerotic changes are beyond the contrast-to-noise ratio obtained with the used ultrahigh-resolution sequences.

Of the more advanced lesions, all eight samples (seven with fibrous plaque, one with fibrolipid plaque) showed at least partial correlation between the spatial organization of the MR signal heterogeneities and the spatial organization of plaque components of the corresponding histological slices. In this small subset,

**“...early atherosclerotic changes are beyond the contrast-to-noise ratio obtained with the used ultrahigh-resolution sequences...”**

a hypointense signal on all sequences generally corresponded to the presence of foamy macrophages, increased proteoglycans, or a lipid-rich core (with or without additional intima-media artefact). Areas of increased collagen

content showed more ambiguous signal intensities ranging from hypo- to hyperintense on the same image contrast weightings. In comparison, previous studies<sup>26-28</sup> on plaque characterization in the carotid artery showed a lipid-rich core to be hyperintense on  $T_1$ -weighted imaging and iso- to hypointense on PD- and  $T_2$ -weighted imaging; a fibrous (collagen-rich) area was shown to be isointense on  $T_1$ -weighted imaging, iso- to hyperintense on  $T_2$ -weighted imaging, and hyperintense on PD-weighted imaging. The discrepancies in signal characteristics between these studies and our results may be due to the prolonged formalin fixation of our due to the changed contrast at ultrahigh field (where, e.g., compact collagen has a shorter  $T_2^*$ <sup>29</sup>), or may be related to the less advanced atherosclerotic status of most of our samples. For instance, we only had one sample with a lipid-rich core, and no samples with intraplaque hemorrhage or plaque rupture, advanced atherosclerotic characteristics on which the MR signal characteristics of these previous studies are mostly based.<sup>26-28</sup>

In 14% of the samples (n=6), heterogeneity of the arterial vessel wall was found on MRI without histological correlates. This could be due to the larger through-plane spatial resolution of the sequences used in this study. Although a through-plane spatial resolution of only 1 mm was used, the resolution obtained with histological slices is still several factors above. Partial volume effects within the obtained 1 mm

thick images result in a summation of signal intensities within this 1 mm thick area, while a single histological slice of 4  $\mu\text{m}$  thickness only shows pathology within that 4  $\mu\text{m}$  thick area.

This study has limitations. Although CoW specimens were selected that macroscopically contained atherosclerotic plaques, only 18% of samples contained advanced plaques with corresponding plaque components. A higher percentage of advanced plaques would have given more clear insight into the specific MR signal characteristics of different plaque components (general signal intensity on different image contrast weightings), which are not as clearly present in early lesions. This especially holds true for increased collagen content within atherosclerotic plaques, that showed ambiguous signal intensity results in the current study. Even so, our results still show that 7T MRI has the image contrast to show focal thickening of the intracranial arterial vessel wall and to distinguish areas with different plaque components using ultrahigh-resolution sequences. Further, in this study 2D slices of selective areas were used for most MR imaging; a 3D approach (like the used  $T_1$ -weighted sequence) with isotropic voxels would decrease exclusion of samples due to location inconsistencies between MRI and histology, thereby decreasing possible selection bias. Regarding technical improvements, development of quantitative MR sequences would enable quantitative plaque characterization, making more bias-prone qualitative scoring performed in the current study unnecessary. A hypointense line within the vessel wall was seen in 25% of samples, corresponding to a defect between the intima and media of the vessel wall. This artefact could be related to a prolonged storage period of the CoW specimens. Although easily identifiable, it did influence our results (see **Table 2**), since foamy macrophages / lipid-rich core have the same hypointense signal; therefore, we could not clearly distinguish vacant space from foamy macrophages /lipid-rich core when the artefact was present in the histological slices. This limitation, however, will not be present in *in vivo* characterization of intracranial atherosclerotic plaques. Furthermore, the current *ex vivo* studies will be of limited use in the validation of contrast enhancement that can be visible with *in vivo* MR imaging. Obviously, contrast agent injection and subsequent enhancement can only be imaged *in vivo*<sup>30</sup> and autopsy in these patients is the only validation method. Finally, the very long scan duration (approximately 40 hours) of the ultrahigh-resolution sequences used in this study prohibit the use of these sequences *in vivo* in clinical practice. However, we feel our results may serve as a starting point for further histological validation of *in vivo* used intracranial vessel wall sequences, albeit with lower spatial resolutions.

In conclusion, our results show that 7T MRI, using ultrahigh-resolution sequences with different image contrast weightings, has the image contrast capable of identifying focal thickening of the intracranial arterial vessel walls, as well as distinguishing areas of different signal intensities that spatially correspond to plaque components within more advanced intracranial atherosclerotic plaques. Additional studies that further validate signal characteristics of the specific plaque components in a quantitative manner, also for lower-resolution sequences, will enable future *in vivo* characterization of intracranial atherosclerotic plaques.

## REFERENCE LIST

- (1) Dieleman N, van der Kolk AG, Zwanenburg JJ, Hartevelde AA, Biessels GJ, Luijten PR, Hendrikse J. Imaging intracranial vessel wall pathology using MRI: current prospects and future directions. *Circulation* 2014 [In-press]
- (2) Klein IF, Lavallee PC, Mazighi M, Schouman-Claeys E, Labreuche J, Amarenco P. Basilar artery atherosclerotic plaques in paramedian and lacunar pontine infarctions: a high-resolution MRI study. *Stroke* 2010;41(7):1405-9.
- (3) Xu WH, Li ML, Gao S et al. Plaque distribution of stenotic middle cerebral artery and its clinical relevance. *Stroke* 2011;42(10):2957-9.
- (4) van der Kolk AG, Zwanenburg JJ, Brundel M et al. Intracranial vessel wall imaging at 7.0-T MRI. *Stroke* 2011;42(9):2478-84.
- (5) Skarpathiotakis M, Mandell DM, Swartz RH, Tomlinson G, Mikulis DJ. Intracranial atherosclerotic plaque enhancement in patients with ischemic stroke. *AJNR Am J Neuroradiol* 2013;34(2):299-304.
- (6) Lou X, Ma N, Ma L, Jiang WJ. Contrast-enhanced 3T high-resolution MR imaging in symptomatic atherosclerotic basilar artery stenosis. *AJNR Am J Neuroradiol* 2013;34(3):513-7.
- (7) van der Kolk AG, Hendrikse J, Brundel M et al. Multi-sequence whole-brain intracranial vessel wall imaging at 7.0 tesla. *Eur Radiol* 2013;23(11):2996-3004.
- (8) Turan TN, Bonilha L, Morgan PS, Adams RJ, Chimowitz MI. Intraplaque hemorrhage in symptomatic intracranial atherosclerotic disease. *J Neuroimaging* 2011;21(2):e159-e161.
- (9) Park JK, Kim SH, Kim BS, Choi G, Jeong SY, Choi JC. Imaging of intracranial plaques with black-blood double inversion recovery MR imaging and CT. *J Neuroimaging* 2011;21(2):e64-e68.
- (10) Chung JW, Kim BJ, Choi BS et al. High-resolution magnetic resonance imaging reveals hidden etiologies of symptomatic vertebral arterial lesions. *J Stroke Cerebrovasc Dis* 2014;23(2):293-302.
- (11) Natori T, Sasaki M, Miyoshi M et al. Evaluating middle cerebral artery atherosclerotic lesions in acute ischemic stroke using magnetic resonance T1-weighted 3-dimensional vessel wall imaging. *J Stroke Cerebrovasc Dis*, published online before print July 18, 2013; doi: 10.1016/j.jstrokecerebrovasdis.2013.06.025.
- (12) Turan TN, Rumboldt Z, Brown TR. High-resolution MRI of basilar atherosclerosis: three-dimensional acquisition and FLAIR sequences. *Brain Behav* 2013;3(1):1-3.
- (13) Yuan C, Mitsumori LM, Ferguson MS et al. In vivo accuracy of multispectral magnetic resonance imaging for identifying lipid-rich necrotic cores and intraplaque hemorrhage in advanced human carotid plaques. *Circulation* 2001;104(17):2051-6.
- (14) Cai JM, Hatsukami TS, Ferguson MS, Small R, Polissar NL, Yuan C. Classification of human carotid atherosclerotic lesions with in vivo multicontrast magnetic resonance imaging. *Circulation* 2002;106(11):1368-73.
- (15) Moody AR, Murphy RE, Morgan PS et al. Characterization of complicated carotid plaque with magnetic resonance direct thrombus imaging in patients with cerebral ischemia. *Circulation* 2003;107(24):3047-52.

- (16) Mitsumori LM, Hatsukami TS, Ferguson MS, Kerwin WS, Cai J, Yuan C. In vivo accuracy of multisequence MR imaging for identifying unstable fibrous caps in advanced human carotid plaques. *J Magn Reson Imaging* 2003;17(4):410-20.
- (17) Cappendijk VC, Cleutjens KB, Kessels AG et al. Assessment of human atherosclerotic carotid plaque components with multisequence MR imaging: initial experience. *Radiology* 2005;234(2):487-92.
- (18) Narumi S, Sasaki M, Ohba H et al. Predicting carotid plaque characteristics using quantitative color-coded T1-weighted MR plaque imaging: correlation with carotid endarterectomy specimens. *AJNR Am J Neuroradiol*, published online before print October 3, 2013; doi: 10.3174/ajnr.A1015.
- (19) den Hartog AG, Bovens SM, Koning W et al. Current status of clinical magnetic resonance imaging for plaque characterisation in patients with carotid artery stenosis. *Eur J Vasc Endovasc Surg* 2013;45(1):7-21.
- (20) Majidi S, Sein J, Watanabe M et al. Intracranial-derived atherosclerosis assessment: an in vitro comparison between virtual histology by intravascular ultrasonography, 7T MRI, and histopathologic findings. *AJNR Am J Neuroradiol* 2013;34(12):2259-64.
- (21) Jahnke C, Dietrich T, Paetsch I et al. Experimental evaluation of the detectability of submillimeter atherosclerotic lesions in ex vivo human iliac arteries with ultrahigh-field (7.0 T) magnetic resonance imaging. *Int J Cardiovasc Imaging* 2007;23(4):519-27.
- (22) Petridou N, Italiaander M, van de Bank BL, Siero JC, Luijten PR, Klomp DW. Pushing the limits of high-resolution functional MRI using a simple high-density multi-element coil design. *NMR Biomed* 2013;26(1):65-73.
- (23) Versluis MJ, Peeters JM, van RS et al. Origin and reduction of motion and f0 artifacts in high resolution T2\*-weighted magnetic resonance imaging: application in Alzheimer's disease patients. *Neuroimage* 2010;51(3):1082-8.
- (24) Virmani R, Kolodgie FD, Burke AP, Farb A, Schwartz SM. Lessons from sudden coronary death: a comprehensive morphological classification scheme for atherosclerotic lesions. *Arterioscler Thromb Vasc Biol* 2000;20(5):1262-75.
- (25) Saam T, Hatsukami TS, Takaya N et al. The vulnerable, or high-risk, atherosclerotic plaque: noninvasive MR imaging for characterization and assessment. *Radiology* 2007;244(1):64-77.
- (26) Yuan C, Mitsumori LM, Beach KW, Maravilla KR. Carotid atherosclerotic plaque: noninvasive MR characterization and identification of vulnerable lesions. *Radiology* 2001;221(2):285-99.
- (27) Fuster V, Fayad ZA, Moreno PR, Poon M, Corti R, Badimon JJ. Atherothrombosis and high-risk plaque: Part II: approaches by noninvasive computed tomographic/magnetic resonance imaging. *J Am Coll Cardiol* 2005;46(7):1209-18.
- (28) Silvera SS, Aidi HE, Rudd JH et al. Multimodality imaging of atherosclerotic plaque activity and composition using FDG-PET/CT and MRI in carotid and femoral arteries. *Atherosclerosis* 2009;207(1):139-43.
- (29) de Jong S, Zwanenburg JJ, Visser F, van der Nagel R, van Rijen HV, Vos MA, de Bakker JM, Luijten PR. Direct detection of myocardial fibrosis by MRI. *J Mol Cell Cardiol* 2011;51:974-9.
- (30) Portanova A, Hakakian N, Mikulis DJ, Virmani R, Abdalla WM, Wasserman BA. Intracranial vasa vasorum: insights and implications for imaging. *Radiology* 2013;267(3):667-79.





# Part 3

## SAFETY ASPECTS OF 7T MRI

---

**Adapted from:**

**Van der Kolk AG**, Ansems J, Raaijmakers AJE, van den Berg CAT, de Borst GJ, Hendrikse J, Luijten PR, Webb AG, Renema WKJ, Klomp DWJ. ***No safety risk in radiofrequency heating of 20 metallic peripheral arterial stents embedded within tissue for MRI studies at 7 tesla.*** Submitted.

# Chapter 6

## SAFETY CONSIDERATIONS FOR RADIOFREQUENCY HEATING OF PERIPHERAL ARTERIAL STENTS

---

Anja G van der Kolk, MD<sup>1</sup>; Janneke Ansems, MSc<sup>4</sup>, Alexander JE Raaijmakers, PhD<sup>1</sup>; Cornelis AT van den Berg, PhD<sup>2</sup>; Gert J de Borst, MD<sup>3</sup>; Jeroen Hendrikse, MD PhD<sup>1</sup>; Peter R Luijten, PhD<sup>1</sup>; Andrew G Webb, PhD<sup>5</sup>; W KlaasJan Renema, PhD<sup>4</sup>; Dennis WJ Klomp, PhD<sup>1</sup>

*From the <sup>1</sup>Department of Radiology, <sup>2</sup>Department of Radiotherapy and <sup>3</sup>Department of Vascular Surgery, University Medical Center Utrecht, P.O. Box 85500, 3508 GA Utrecht, The Netherlands; the <sup>4</sup>Department of Radiology, Radboud University Nijmegen Medical Center, P.O. Box 9101, 6500 HB Nijmegen, The Netherlands; and <sup>5</sup>C.J.Gorter Center for High Field MRI, Department of Radiology, Leiden University Medical Center, Leiden, The Netherlands.*

# Key points

- » Full application of 7T MRI in the clinical setting is limited by strict safety rules regarding metallic implants, primarily because of fear of RF heating.
- » Literature shows conflicting results regarding RF heating of metallic implants at different field strengths.
- » Higher frequency at high field strength has two effects:
  - Increases risk of resonance, thereby *increasing* risk of RF heating
  - Increases attenuation of electromagnetic waves in tissue, dampening resonance and *decreasing* risk of RF heating
- » Resonance damping is shown to be the dominant effect at 7T, decreasing the risk of RF heating of metallic implants when embedded in tissue.
- » Twenty peripheral arterial stents showed a corresponding lack of RF heating in a worst-case scenario.
- » Displacement and torque measurements of the 20 stents were within safety limits, demonstrating MR compatibility of these stents at 7T MRI when embedded in tissue.

## INTRODUCTION

Magnetic resonance imaging (MRI) has evolved into one of the most important non-invasive techniques within the field of clinical diagnostic imaging, with 7 tesla (7T) being the most recent commercially available magnetic field strength for potential clinical MRI applications<sup>1</sup>. Due to the increased signal-to-noise ratio (SNR) and contrast-to-noise ratio (CNR), and increased sensitivity to tissue-specific magnetic susceptibility effects, high-resolution images with improved lesion conspicuousness can be obtained<sup>2-4</sup>. Many (clinical) studies have therefore focused on using 7T MRI for diagnosis of a multitude of diseases, predominantly in the brain, such as multiple sclerosis (MS) and cerebrovascular diseases (**Chapter 1**)<sup>5</sup>.

An important prerequisite for clinical acceptance of an MR system is assessment and validation of the intrinsic safety of implanted devices, such as metallic implants. A substantial number of patients eligible for 7T MRI – in a clinical or research context – have small metallic implants such as arterial stents, surgical clips, or dental prostheses, and are currently excluded from 7T imaging<sup>6</sup>. Given the focus of 7T studies on patients with cardiovascular or neurologic diseases – relatively older people with a high likelihood to have undergone medical interventions – this limitation to research projects and clinical diagnosis has a severe impact.

**“...substantial number of patients eligible for 7T MRI have small metallic implants and are currently excluded from 7T imaging...”**

Three major factors that play a role in the intrinsic safety of metallic implants are radiofrequency (RF) heating, magnetically induced displacement force and magnetically induced torque. Testing of these factors at lower field strengths has been standardized in the American Society for Testing and Measurement (ASTM) standards<sup>7-9</sup>, and metallic implants have been tested to various extent for 1.5T and 3T MRI<sup>10-12</sup>. However, higher magnetic field strengths, such as 7T, give rise to highly non-uniform RF fields and RF power deposition<sup>13-15</sup>. In addition, in contrast to lower field strengths, local excitation coils rather than a large body coil are used extensively. Since the ASTM standards, defined for lower field strengths, assume both well-characterized RF fields as well as transmission by a large volume coil, they will therefore not be appropriate for testing at 7T, especially regarding possible RF heating.

As a consequence, safety studies at 7T have only recently emerged within the field of MR safety. Within these studies, a limited amount of different types of metallic implants, such as intraocular lenses<sup>16</sup>, upper eyelid implants<sup>17</sup>, ear-nose-throat implants<sup>18</sup>, cranial fixation plates<sup>19</sup>, extracranial implants<sup>20</sup>, coronary artery stents<sup>21</sup>, and dental retainer wires<sup>22</sup> have been tested. These metallic implants showed no

RF heating at 7T field strength. However, conflicting results have been published at lower field strengths, in which, for instance, excessive temperature increases at 1.5T due to RF heating have been reported<sup>23, 24</sup>. The question arises on what underlying factor(s) associated with RF heating these discrepancies are based.

Several factors are important when considering the RF safety of metallic implants at 7T. Any conductive (metallic) structure that is placed within the electromagnetic (EM) field of the RF transmit coil will couple with that field (i.e. act as an antenna to receive and potentially amplify the local EM field). The oscillating EM field causes a differential voltage along the length of the structure, resulting in an alternating current (AC) flow. This subsequently leads to concomitant high magnetic and electric

fields in the immediate surroundings that can lead – due to induced currents in the surrounding tissue – to localized heating. The currents in the structure maximize in the resonance condition, which is when the length of the structure matches

**“...question arises on what underlying factor(s) associated with RF heating these discrepancies are based...”**

integer multiples of half the wavelength in tissue of the EM field. In this case, coupling with the EM field is maximal and extreme localized heating can occur<sup>24</sup>. The half-wavelength at which resonance occurs at a magnetic field strength of 1.5T is 236 cm in air and approximately 34 cm in blood vessels<sup>25</sup>. At 7T, the Larmor frequency is higher, and therefore the half-wavelength at which resonance occurs is shorter: 51 cm in air and approximately 7 cm in blood vessels. This latter length is close to the size of commonly used peripheral arterial stents, which have typical lengths between 2-10 cm, particularly when including the wire winding pattern of a given stent. This wire-winding pattern, common to most stents, can increase the electrical length at which resonance occurs, which significantly increases the risk of resonance.

Coupling of the conductive structure is dependent on the quality (Q) factor of the structure. The Q factor represents the ratio between the amount of energy that is induced and stored in the structure (build-up) and the amount of energy that is dissipated (in the surrounding tissue, causing induced currents) within a resonant system. A high Q factor implies stronger coupling between the implant and the RF coil, and therefore more RF power transferred from the transmit coil to the implant. At higher frequencies, however, the induced field of the transmit coil will be counteracted more by the fields caused by the currents in the surrounding tissue. In fact, these counteracting fields increase the resistance of the stent (loading), resulting in a damping of resonances (less energy within stent, more energy dissipated) or, equivalently, a decrease of the Q factor at higher field strength.<sup>26, 27</sup>

In this study, we sought to determine the effect of 7T on the factors associated with RF heating of metallic implants, and the reason for the discrepancies as found at lower field strengths, using tissue-mimicking phantom experiments. These fundamental experiments showed that a very low Q factor at high magnetic field strength is the dominant factor in the assessment of safety of metallic implants at 7T, which results in a low risk of localized heating due to EM fields. Further, we tested these findings in temperature measurements of 20 metallic arterial peripheral stents of worst-case lengths at 7T, that, combined with validating mechanical safety, supported the safety hypotheses by showing an increase of < 2 °C when overriding safety limits threefold.

## **MATERIALS AND METHODS**

First, fundamental experiments were performed to assess to what extent the Q factor of a given conductive structure is influenced by loading of the structure and by the frequency of the RF transmit coil. Then, temperature increase was measured in a phantom setting, using metallic peripheral arterial stents, with a length approximating the half-wavelength of the RF field at 7T, positioned in the strongest electric field of the transmit coil, to simulate the *in vivo* situation in a 'worst-case' scenario. To complete the full safety testing of these 20 stents for MR compatibility at 7T, displacement and torque measurements were performed.

### **Q factor measurements with variable loading**

The net-like, wire-winding structure of stents makes it difficult to exactly predict their resonant length, since the length of the path that currents have to travel along the stent does not necessarily coincide with the total length of the stent. Therefore, the length of a non-insulated copper wire (diameter 1 mm) was varied until resonance occurred at 298 MHz, the Larmor frequency at 7T. The copper wire was first suspended in a large container of deionized water. Then salt was increasingly added to obtain a total of 5 different solution conductivities: 0.05 S/m (deionized water), 0.25 S/m, 0.5 S/m, 0.75 S/m, and 1.0 S/m. Electrical conductivity was measured using the network analyzer in combination with an open-ended coaxial probe (HP85070, Agilent Technologies Inc., Palo Alto, CA, USA). Q factors of the copper wire for the different solution conductivities were calculated using a network analyzer (8714ET, Agilent Technologies Inc., Palo Alto, CA, USA) with two weakly coupled small pickup probes that were placed on either end of the copper wire. The transmission of probe 1 to probe 2 ( $S_{12}$  measurement) was used by the network analyzer to calculate the center frequency and bandwidth of the wire. The Q factor was then calculated by dividing the center frequency by the bandwidth.

### **Q factor measurements with variable frequency**

Twenty conductors bent in a single loop with diameters of 20 (6 conductors), 30 (8 conductors) and 50 mm (6 conductors) were constructed using an insulated copper wire (diameter 1 mm), and tuned (to resonate) by a single capacitor to frequencies ranging from 50-350 MHz. Unloaded Q factors (in air) were measured as described above. Loaded Q values were measured similarly by partial suspension (95% of surface area, excluding the tuning capacitor, being the dominant part of the electric fields) in saline with a conductivity of 0.5 S/m, resembling human tissue.

### **Peripheral stents**

Twenty peripheral arterial stents (used for endovascular treatment of the carotid artery) from five different commercial vendors were included, ranging in length from 20-100 mm – resembling the half-wavelength at 7T in tissue of approx. 70 mm – and in diameter from 4-10 mm (Table). None of the included stents had a surface coating, and all stents had a woven lattice without welds. Thirteen of the included stents in this study have been approved for use in a recent international clinical trial on carotid stenting<sup>28</sup>. Stents were individually embedded in an agarose phantom with minimized heat flow (volume 750 mL, conductivity 0.5 S/m), which mimicked the dielectric- and conductivity properties of tissue as stated in the standard ASTM test method, F2182-11<sup>7</sup>.

### **MR setup**

The worst-case scenario setup that was used was adapted from the test setup used in the ASTM-standard for RF induced heating (F2182-11)<sup>7</sup>. ASTM standard F2182-11 has a worst-case setup that is appropriate for MRI systems that produce relatively uniform RF fields due to the low frequency (i.e. 1.5T and 3T MR systems) and subsequent large wavelengths compared to the dimensions of the phantom used. At 7T, however, the RF fields produced in such a phantom are not homogeneous (due to standing waves), and RF power concentrates in specific areas, resulting in severe inhomogeneity in the specific absorption (SAR) distribution<sup>13-15</sup>. Therefore, RF energy- and SAR values of the ASTM standard cannot be directly translated to 7T.

To account for these issues, a local RF coil which produces a strong EM field and well-characterized maximum local SAR at reproducible locations was used<sup>29</sup>. This custom-built two-channel unilateral RF coil, originally designed for breast imaging at 7T, was used as an RF transmit and receive coil<sup>29</sup>. The coil was tuned and matched to 50 Ohms at 298 MHz and operated in quadrature. Finite difference time domain calculations were applied to estimate the electromagnetic fields in the female model Ella of The Virtual Family<sup>30</sup> at a spatial isotropic resolution of 2 mm<sup>31, 32</sup>. Local specific absorption rate (SAR) was extrapolated to isotropic voxels of 10 mL,

**Table** Maximum temperature increase, maximum displacement and torque measurement for each tested peripheral arterial stent

No.	Vendor	Type	Diameter (mm)	Length (mm)	Max temp increase (°C)	Max deflection (°)	Gravity torque (N m)	Flip torque (N m)
1	Invatec	Maris	7	80	0.2	7	$2.5 \times 10^{-4}$	$2.9 \times 10^{-6}$
2	Invatec	Scuba	7	30	0.4	15	$2.1 \times 10^{-5}$	$2.9 \times 10^{-6}$
3	Boston Scientific	Carotid Wallstent Monorail	10	24	0.4	32	$3.4 \times 10^{-5}$	$2.9 \times 10^{-6}$
4	Boston Scientific	Adapt™ Monorail™	4-9	32	0.5	6	$2.3 \times 10^{-5}$	$2.9 \times 10^{-6}$
5	Boston Scientific	Adapt™ Monorail™	4-9	40	1.3	6	$3.3 \times 10^{-5}$	$2.9 \times 10^{-6}$
6	Cordis	Smart Control Nitinol stent	7	80	0.2	7	$3.0 \times 10^{-4}$	$2.9 \times 10^{-6}$
7	Cordis	Smart Control Nitinol stent	6	100	0.0	7	$4.6 \times 10^{-4}$	$6.4 \times 10^{-6}$
8	Cordis	Precise	10	40	0.8	6	$7.6 \times 10^{-5}$	$2.9 \times 10^{-6}$
9	Cordis	Precise	10	20	0.0	6	$1.8 \times 10^{-5}$	$2.9 \times 10^{-6}$
10	Cordis	Precise	5	20	0.5	7	$1.5 \times 10^{-5}$	$2.9 \times 10^{-6}$
11	Cordis	Precise	5	40	1.6	7	$6.2 \times 10^{-5}$	$2.9 \times 10^{-6}$
12	Ev3	Protege RX	8	60	0.3	7	$2.0 \times 10^{-4}$	$2.9 \times 10^{-6}$
13	Ev3	Protege RX	8	40	0.7	7	$8.5 \times 10^{-5}$	$2.9 \times 10^{-6}$
14	Ev3	Protege Everflex	7	100	0.1	7	$4.0 \times 10^{-4}$	$5.0 \times 10^{-6}$
15	Abbott Vascular	Xact Carotid stent	7	20	0.6	6	$1.6 \times 10^{-5}$	$2.9 \times 10^{-6}$
16	Abbott Vascular	Xact Carotid stent	8-6	40	1.9	7	$6.0 \times 10^{-5}$	$2.9 \times 10^{-6}$
17	Abbott Vascular	RX Acculink	8-6	40	0.4	6	$4.5 \times 10^{-5}$	$2.9 \times 10^{-6}$
18	Abbott Vascular	RX Acculink	7-10	40	0.7	6	$4.2 \times 10^{-5}$	$2.9 \times 10^{-6}$
19	Abbott Vascular	RX Acculink	6	20	0.7	5	$1.1 \times 10^{-5}$	$2.9 \times 10^{-6}$
20	Abbott Vascular	Xact Carotid stent	9-7	40	1.2	6	$6.0 \times 10^{-5}$	$2.9 \times 10^{-6}$

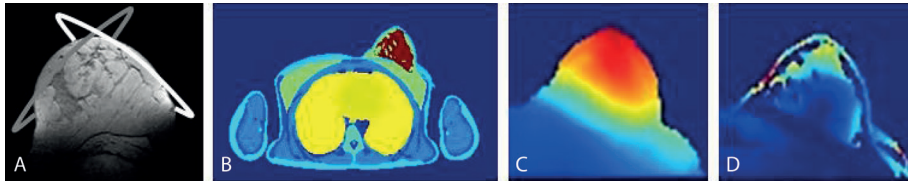


**Figure 1** Measurements and simulations of the focused field and radiofrequency (RF) power deposition of the RF transmitter coil used to deposit a well-controlled and maximum energy to the stents. (A) Illustration of coil setup, in which the two circles indicate the location of the dual channel RF coil surrounding the model breast. (B) Anatomical model (Ella, 22)<sup>30</sup> merged with segmented data from 7 tesla (7T) magnetic resonance imaging (MRI) images. (C) Simulated RF field distribution of the dual channel RF coil, showing an inhomogeneous field with a maximum of 40  $\mu\text{T}$  in the center of the model breast when 2 kW of RF power is delivered. (D) Corresponding simulated specific absorption rate (SAR) profile of the same breast model, showing RF power deposition to a maximum of 10 W/kg when 4 W of RF power is delivered.

corresponding to local SAR values averaged over less than 10 g, as defined in the International Electrotechnology Commission (IEC) guidelines<sup>33</sup>. The average power required to obtain a maximum local SAR of 10 W/kg was defined (**Figure 1**). This hotspot was found close to the capacitors of the RF coil, ensuring a well-defined location of the electric field gradient to test the stents in a worst-case condition. Each stent embedded in a phantom was therefore positioned in the coil at this position of highest calculated SAR.

### MR scan protocol

We acquired MRI data with a passively shielded 7T MRI scanner (Philips Healthcare, Cleveland, OH, USA). Coil-specific parameters were adapted to enable scan parameters to exceed the calculated SAR limit by a factor of three. A semi-LASER (localization by adiabatic selective refocusing) spectroscopic sequence<sup>34</sup> with repetition time (TR) of 1000 ms was used to administer a time-averaged RF power of 12 W to the phantom. This RF power was measured at the entrance of the coil by a calibrated RF power measurement device. During the 5-minute semi-LASER sequence, high RF power of 12 W was administered, resulting in a local SAR of 30 W/kg, which is three times the international local body SAR limit of 10 W/kg in the “first controlled model”<sup>33</sup>.

For each stent, two consecutive 5-minute semi-LASER sequences were performed. According to the ASTM standard, a period of 15 minutes of scanning with RF power of 2 W/kg, assuming a homogeneous RF field and global SAR, is recommended<sup>7</sup>. We compensated for the inhomogeneity of the RF field by making use of a well-characterized and reliable local SAR distribution. Together with increased RF power administration, and assuming a linear temperature rise, this allows for the reduced scan times in our setup.

**Temperature measurements**

Temperature was measured once per second by four MRI-compatible fiber-optic temperature probes (Luxtron m3300, Santa Clara, CA, temperature resolution 0.1 degrees Celsius). Two probes were placed at the ends of each stent and two probes were placed parallel and perpendicular to the stent as a reference. Placement of probes was verified by a 3-dimensional (3D) MRI scan prior to the measurement. Temperature measurements consisted of 2 minutes baseline recording followed by measurements during two consecutive 5-minute semi-LASER sequences. Measurements were also obtained without any stent in the phantom to confirm the location of highest RF power deposition.

**Displacement force measurements**

Displacement is caused by the force produced by static magnetic field gradients. For measuring displacement, each stent was put in an apparatus as described in ASTM standard F2052-06<sup>ε1</sup>, that measured the attraction of the static magnetic field on the stent compared to the force of gravity<sup>8</sup>. The measurement was performed at the position of the highest spatial gradient, which is the entrance of the bore, off-axis and at a side wall. The spatial gradient of the magnetic field at this location was 482 gauss/cm<sup>35</sup>.

**Torque measurements**

Torque, or a 'twist' of the implant, is caused by the interaction of the static magnetic field with the magnetization in the implant – the force aligns the implant with the magnetic field – and is strongest in the isometric center of the scanner bore<sup>9</sup>. For measuring torque, an adapted version of the apparatus as described in ASTM standard F2213-06 was used<sup>9</sup>. In this standard, the 'twist' the main magnetic field applies on a metallic implant is assessed by using small springs that are calibrated to measure the force necessary to undo the twist. However, even very small springs will contain some form of metal, and are therefore excluded for a test setup at 7T. We therefore made a setup in which each tested implant (stent) was carried by a custom-made small tube which was attached to a fine tensed thread and suspended in air. Attached to the tube was a small and long plastic block to which additional small blocks could be added, in order to stabilize the assembly before testing. The apparatus was then placed in the center of the main magnetic field with the stent parallel and at a slight angle to the field. Small plastic weights were hung on the plastic block until the coil-plastic unit twisted by their weight. In this way, an approximation of the precise torque for each stent could be calculated, based on the sum of the weights and the moment of the stent, and compared with the calculated gravitational torque (based on the weight and length of the

stent)<sup>9</sup>. The weights of the stents and the small weights were measured using an electronic weighing scale (Mettler Analytical Balance AE 240 Dual Range Balance, Mettler Toledo Intl.) with a reproducibility of 0.02 mg.

## RESULTS

### Q factor dependence

The influence of loading on the Q factor was examined by tuning the length of a copper wire to a half-wave at 298 MHz (resonance frequency at 7T), submerging it in deionized water with variable conductivity (by solution of NaCl), and measuring the Q factor for each of the 5 different solutions. We found the copper wire to have a measured loaded Q factor of 10 in deionized water. The Q factor dropped to 3 when the conductivity of the solution was increased to 0.5 S/m, which mimics the conductivity properties of tissue (**Figure 2**).

Next, the influence of frequency of the RF transmit coil on loading and therefore indirectly on the Q factor, was examined. Measurements were made of the Q factor of 20 conductors bent as single loops that were made resonant by capacitors to different frequencies (ranging from 50-350 MHz), and were suspended in air and in a saline solution with a 0.5 S/m conductivity. Q factors for each coil were calculated to be above 240 in air (**Figure 3a**). When the coils were loaded, the Q factor decreased from approximately 70 at a frequency of 127 MHz (which corresponds to a clinical 3T scanner) to 10 at 300 MHz (**Figure 3b**).

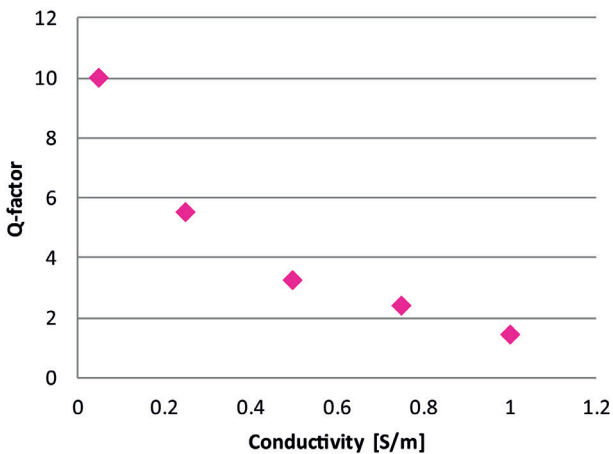


**Figure 2** Resonance damping reflected by quality (Q) factor measurements in different media. Q factor values of a tuned copper wire (half-wavelength) resonating at 298 MHz as a function of the electrical conductivity of the surrounding saline solution.

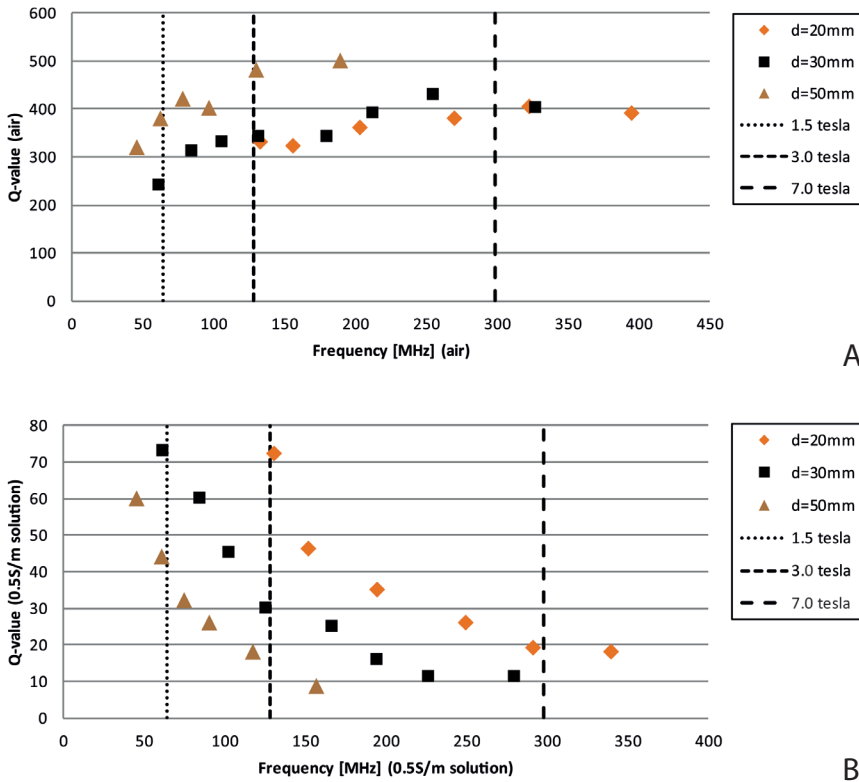


**Figure 3** Resonance damping reflected by Q factor measurements at different frequencies resembling the available MRI field strengths. Q factor values of 20 copper conductors, bent as single loops and tuned with capacitors to resonate at frequencies ranging from 50 to 350MHz (i.e., resembling MRI of 1.2T to 8T). In (A), the tuned conductors were unloaded (in air), while in (B), they were loaded by close to complete submersion within a saline solution with 0.5 S/m conductivity. The diameter of the single loops is denoted by d; corresponding field strength Larmor frequencies are indicated by dotted lines.

### Temperature measurements

Measurements were performed with 20 stents that were placed in individual phantoms with a conductivity of 0.5 S/m, and positioned at the location of maximum local SAR within the RF coil. The temperature measurements during MR scanning showed that in this worst-case setting, no stent produced a rise in temperature above 2 °C (mean 0.6 °C, range 0.0-1.9 °C; **Figure 4, Table**), compared with no temperature change without the stent present. The maximum temperature increase was found for stents with a length of 40 mm; considering the wire winding pattern of a stent, this length is close to the expected half-wavelength of 70 mm in the used phantom.

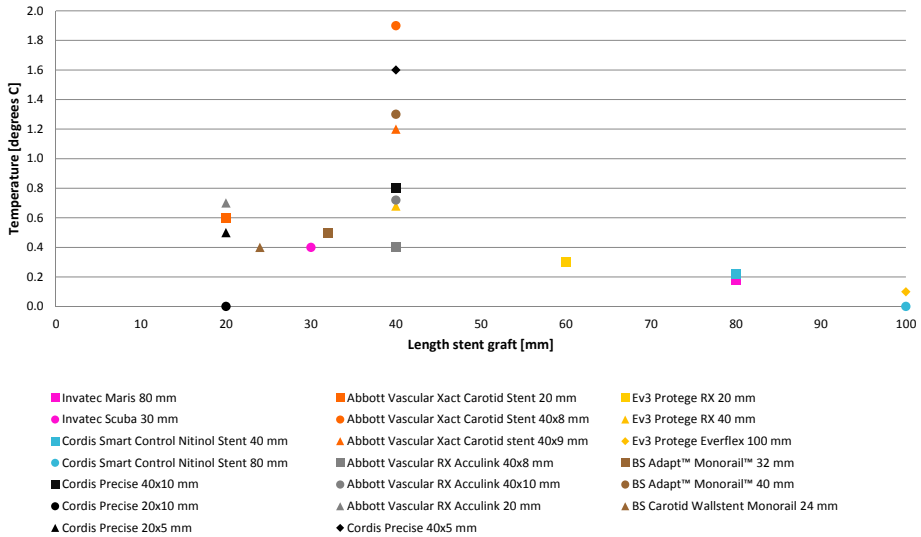


**Figure 4** RF-induced temperature changes of peripheral arterial coils. Graph showing measured temperature increases at the tip of 20 tested stents in tissue-equivalent phantoms. Temperature was measured during a 5-minute administration of RF power, set to three times the international local body SAR limit of 10 W/kg when assuming no stent.

### Magnetic forces

Displacement and torque, both magnetically induced effects, were tested using the respective ASTM standards (F2052-06<sup>61</sup> and F2213-06)<sup>8, 9</sup>, which were adapted if necessary to the high field strength situation. Displacement experiments showed a mean displacement of 8 degrees (**Table**), with the largest displacement of 32 degrees found in a stent with 10 mm diameter and 24 mm length. This value is below the maximally allowed safety guideline of 45 degrees displacement<sup>8</sup>. Torque experiments showed a mean naturally occurring torque, due to the gravitational field, of  $1.1 \times 10^{-4}$  N m (range  $1.1 \times 10^{-5}$  to  $4.6 \times 10^{-4}$  N m; **Table**). When placed in our test setup at the isometric center of the scanner bore, the mean torque induced by the static magnetic field was  $3.2 \times 10^{-6}$  N m (range  $2.9 \times 10^{-6}$  to  $6.4 \times 10^{-6}$  N m), which is approximately 35 times less than caused by the gravitational torque (**Table**).

### DISCUSSION

Metallic implants are currently a major contraindication for MR imaging at 7T. Due to the high frequency of the RF transmit field, the half-wavelength at which resonance occurs can approach the dimensions of commonly used metallic implants, such as (widely used) peripheral arterial stents, thereby potentially increasing the risk of RF heating. In addition, magnetically induced forces are stronger when a high

magnetic field strength is used, increasing the risk of displacement and torque of the metallic implant. However, other factors that are influenced by the high magnetic field strength – such as resonance damping – also come into play, the extent of which has not been extensively studied to date.

Our results indicate that the resonance damping or Q factor decrease is the dominant factor in RF heating of conductive structures, such as metallic implants, at a high magnetic field strength of 7T. These results were reproduced indirectly by our temperature measurements of 20 stents, in which stent sizes were used with a strong coupling (due to resonance and position) to the RF source, and exposed RF power levels far higher than the regulatory limits. In this setup we found no substantial temperature increase of the peripheral arterial stents. These findings are supported by results from other studies at 7T, that showed no RF heating when testing different types of metallic implants<sup>16-22</sup>. Cases in literature, in which

**“...resonance damping or Q factor decrease is the dominant factor in RF heating of conductive structures at a high magnetic field strength of 7T...”**

excessive temperature increases due to RF heating have been reported, are obtained at 1.5T and can be explained by very high Q factors<sup>23,24</sup>. Additionally to its lower frequency and therefore higher Q factors, the guide wires as reported at 1.5T are surrounded by air that does not absorb RF energy. This increases the Q factor even further, thereby no longer dampening the potential resonance, thus causing excessive heating in tissue.

Regarding RF heating of the 20 tested stents in this study, two additional factors that play a role are the effects of blood flow on heating and the effects of reduced global SAR at a high magnetic field strength. Blood flow is an extremely effective mechanism of heat dissipation<sup>36</sup>. In our test setup, we have not taken this mechanism into account. Even if the temperature at the tip of the peripheral arterial stent increases by 1.9 °C (the highest temperature increase found in our study), the blood flowing through the stent would be able to diminish this temperature rise<sup>37,38</sup>, most probably resulting in an even lower temperature rise for stents than reported in our study. When considering overall safety aspects of MR imaging, SAR – the rate of energy absorption by a subject when it is exposed to an RF field – is an important determinant for the maximum amount of RF power that can be given. It can be divided into global SAR (averaged over the whole body) and local SAR, where local SAR is dependent on the local tissue properties. To prevent tissue heating, international limits have been determined for both global and local SAR individually, where local SAR limits are less restricted (i.e. higher) due to the local nature of power deposition. At lower field strengths (e.g. 1.5T), local SAR limits are often not reached due to the more homogeneous distribution of RF

energy; therefore, the averaged overall RF power that can be applied is restricted primarily by global SAR limits. At high magnetic field strengths (which is the case in our situation at 7T), RF energy is distributed less homogeneously, causing tissue ‘hotspots’ with (very) high local SAR values. In this case, *local* SAR limits primarily restrict the averaged overall RF power exposure. Consequently, the overall maximum RF power that can be used at a high magnetic field strength will be lower than at lower field strengths, thereby exposing stents, when not specifically at a ‘hotspot’, to less RF energy at high field, even further decreasing the risk of RF heating.

Torque and displacement, induced by the static magnetic field, need to be considered when a metallic implant is considered to be accepted as ‘MR conditional’ or even ‘MR safe’<sup>39,40</sup>. Torque tests showed that the torque caused by the gravitational field on the tested stents is approximately 35 times stronger than their torque induced by the magnetic field. The displacement tests showed that the force of the static magnetic field gradient on the tested stents is less than their experienced gravitational force. These results suggest that there are no risks of any physical displacement of the stents included in this study inside the body within a 7T MR environment.

The strength of the static magnetic field gradient is dependent on the method of shielding – reducing magnetic field outside the MR system – and can be either passive or active. In passive shielding, ferromagnetic plating

**“...the 20 tested stents are MR compatible at 7T when embedded in tissue...”**

shields the system, while with active shielding, a portion of the main magnetic field is opposed through an extra set of superconducting windings within the cryostat. With active shielding, therefore, the static magnetic field will be more confined to the MR system, resulting in stronger static field gradients. Although currently most 7T systems are passively shielded, displacement tests for the tested stents might have to be performed again when actively shielded 7T systems become commercially available.

In conclusion, the risk of RF heating of a conductive structure, like a metallic implant, at a high magnetic field strength is primarily determined by the Q factor. Our results show that this Q factor at 7T is very low, especially when compared to lower magnetic field strengths, resulting in a temperature rise of  $\leq 2$  °C of 20 tested peripheral arterial stents in a worst-case scenario. Displacement and torque measurements of these 20 stents were within MR safety limits, suggesting that these 20 tested stents are MR compatible at 7T when embedded in tissue.

### **ACKNOWLEDGEMENTS**

We would like to thank W.J.M. Gosselink for his help designing the setup for measuring the magnetically induced torque of the 20 tested metallic peripheral arterial stents.

## REFERENCE LIST

- (1) Moser E, Stahlberg F, Ladd ME, Trattnig S. 7-T MR—from research to clinical applications? *NMR Biomed* 2012;25(5):695-716.
- (2) Duyn JH, van Gelderen P, Li TQ, de Zwart JA, Koretsky AP, Fukunaga M. High-field MRI of brain cortical substructure based on signal phase. *Proc Natl Acad Sci U S A* 2007;104(28):11796-801.
- (3) Vaughan JT, Garwood M, Collins CM et al. 7T vs. 4T: RF power, homogeneity, and signal-to-noise comparison in head images. *Magn Reson Med* 2001;46(1):24-30.
- (4) Eapen M, Zald DH, Gatenby JC, Ding Z, Gore JC. Using high-resolution MR imaging at 7T to evaluate the anatomy of the midbrain dopaminergic system. *AJNR Am J Neuroradiol* 2011;32(4):688-94.
- (5) van der Kolk AG, Hendrikse J, Zwanenburg JJ, Visser F, Luijten PR. Clinical applications of 7T MRI in the brain. *Eur J Radiol* 2003;82(5):708-18.
- (6) van der Kolk AG, Zwanenburg JJ, Brundel M et al. Intracranial vessel wall imaging at 7.0-T MRI. *Stroke* 2011;42(9):2478-84.
- (7) American Society for Testing and Materials (ASTM) International. ASTM Standard F2182, 2011, "Measurement of radio frequency induced heating on or near passive implants during magnetic resonance imaging" ASTM International, West Conshohocken, PA, 2011, DOI: 10.1520/F2182-11, www.astm.org.
- (8) American Society for Testing and Materials (ASTM) International. ASTM Standard F2052, 2006e1, "Measurement of magnetically induced displacement force on medical devices in the magnetic resonance environment" ASTM International, West Conshohocken, PA, 2006, DOI: 10.1520/F2052-06E01, www.astm.org.
- (9) American Society for Testing and Materials (ASTM) International. ASTM Standard F2213, 2006, "Measurement of magnetically induced torque on medical devices in the magnetic resonance environment" ASTM International, West Conshohocken, PA, 2006, DOI: 10.1520/F2213-06, www.astm.org.
- (10) Shellock FG, Shellock VJ. Metallic stents: evaluation of MR imaging safety. *AJR Am J Roentgenol* 1999;173(3):543-7.
- (11) Shellock FG, Forder JR. Drug eluting coronary stent: in vitro evaluation of magnet resonance safety at 3 tesla. *J Cardiovasc Magn Reson* 2005;7(2):415-9.
- (12) Hug J, Nagel E, Bornstedt A, Schnackenburg B, Oswald H, Fleck E. Coronary arterial stents: safety and artifacts during MR imaging. *Radiology* 2000;216(3):781-7.
- (13) van den Bergen B, Van den Berg CA, Bartels LW, Lagendijk JJ. 7 T body MRI: B1 shimming with simultaneous SAR reduction. *Phys Med Biol* 2007;52(17):5429-41.
- (14) van den Bergen B, Klomp DW, Raaijmakers AJ et al. Uniform prostate imaging and spectroscopy at 7 T: comparison between a microstrip array and an endorectal coil. *NMR Biomed* 2011;24(4):358-65.
- (15) van den Bergen B, Van den Berg CA, Klomp DW, Lagendijk JJ. SAR and power implications of different RF shimming strategies in the pelvis for 7T MRI. *J Magn Reson Imaging* 2009;30(1):194-202.

- (16) van Rijn GA, Mourik JE, Teeuwisse WM, Luyten GP, Webb AG. Magnetic resonance compatibility of intraocular lenses measured at 7 tesla. *Invest Ophthalmol Vis Sci* 2012;53(7):3449-53.
- (17) Schrom T, Thelen A, Asbach P, Bauknecht HC. Effect of 7.0 tesla MRI on upper eyelid implants. *Ophthal Plast Reconstr Surg* 2006;22(6):480-2.
- (18) Thelen A, Bauknecht HC, Asbach P, Schrom T. Behavior of metal implants used in ENT surgery in 7 tesla magnetic resonance imaging. *Eur Arch Otorhinolaryngol* 2006;263(10):900-5.
- (19) Kraff O, Wrede KH, Schoemberg T et al. MR safety assessment of potential RF heating from cranial fixation plates at 7 T. *Med Phys* 2013;40(4):042302.
- (20) Sammet CL, Yang X, Wassenaar PA et al. RF-related heating assessment of extracranial neurosurgical implants at 7T. *Magn Reson Imaging* 2013;31(6):1029-34.
- (21) Santoro D, Winter L, Muller A et al. Detailing radio frequency heating induced by coronary stents: a 7.0 tesla magnetic resonance study. *PLoS One* 2012;7(11):e49963.
- (22) Wezel J, Kooij BJ, Webb AG. Assessing the MR compatibility of dental retainer wires at 7 tesla. *Magn Reson Med*, published online before print November 11, 2013; DOI 10.1002/mrm.25019.
- (23) Finelli DA, Rezaï AR, Ruggieri PM et al. MR imaging-related heating of deep brain stimulation electrodes: in vitro study. *AJNR Am J Neuroradiol* 2002;23(10):1795-802.
- (24) Konings MK, Bartels LW, Smits HF, Bakker CJ. Heating around intravascular guidewires by resonating RF waves. *J Magn Reson Imaging* 2000;12(1):79-85.
- (25) Gabriel C, Gabriel S, Corthout E. The dielectric properties of biological tissues: I. Literature survey. *Phys Med Biol* 1996;41(11):2231-49.
- (26) Carlson JW. Power deposition and noise correlation in NMR samples. *Magn Reson Med* 1989;10(3):399-403.
- (27) Stutzman WL, Thiele GA. *Antenna Theory and Design*. 2nd edition ed. Wiley; 1997.
- (28) Ederle J, Dobson J, Featherstone RL et al. Carotid artery stenting compared with endarterectomy in patients with symptomatic carotid stenosis (International Carotid Stenting Study): an interim analysis of a randomised controlled trial. *Lancet* 2010;375(9719):985-97.
- (29) Korteweg MA, Veldhuis WB, Visser F et al. Feasibility of 7 tesla breast magnetic resonance imaging determination of intrinsic sensitivity and high-resolution magnetic resonance imaging, diffusion-weighted imaging, and (1)H-magnetic resonance spectroscopy of breast cancer patients receiving neoadjuvant therapy. *Invest Radiol* 2011;46(6):370-6.
- (30) Christ A, Kainz W, Hahn EG et al. The Virtual Family--development of surface-based anatomical models of two adults and two children for dosimetric simulations. *Phys Med Biol* 2010;55(2):N23-N38.
- (31) Van den Berg CA, Bartels LW, van den BB et al. The use of MR B+1 imaging for validation of FDTD electromagnetic simulations of human anatomies. *Phys Med Biol* 2006;51(19):4735-46.
- (32) Klomp DJ, Raaijmakers AJ, Korteweg MA et al. High resolution MR imaging and spectroscopy of the human breast at 7T using a focused field RF coil setup. *Proc Intl Soc Mag Reson Med* 18 (2010), abstract no. 2469.

- (33) International Electrotechnology Commission (IEC). IEC 60601-2-33. Medical electrical equipment - Part 2-33: Particular requirements for the basic safety and essential performance of magnetic resonance equipment for medical diagnosis. 3<sup>rd</sup> edition 2010.
- (34) Boer VO, van Lier AL, Hoogduin JM, Wijnen JP, Luijten PR, Klomp DW. 7-T (1) H MRS with adiabatic refocusing at short TE using radiofrequency focusing with a dual-channel volume transmit coil. *NMR Biomed* 2011;24(9):1038-46.
- (35) Shellock FG, Kanal E, Gilk TB. Regarding the value reported for the term "spatial gradient magnetic field" and how this information is applied to labeling of medical implants and devices. *AJR Am J Roentgenol* 2011;196(1):142-5.
- (36) Pennes HH. Analysis of tissue and arterial blood temperatures in the resting human forearm. *J Appl Physiol* 1948;1(2):93-122.
- (37) Lagendijk JJ. The influence of bloodflow in large vessels on the temperature distribution in hyperthermia. *Phys Med Biol* 1982;27(1):17-23.
- (38) Crezee J, Lagendijk JJ. Experimental verification of bioheat transfer theories: measurement of temperature profiles around large artificial vessels in perfused tissue. *Phys Med Biol* 1990;35(7):905-23.
- (39) Shellock FG, Woods TO, Crues JV, III. MR labeling information for implants and devices: explanation of terminology. *Radiology* 2009;253(1):26-30.
- (40) American Society for Testing and Materials (ASTM) International. ASTM Standard F2503, 2008, "Marking medical devices and other items for safety in the magnetic resonance environment" ASTM International, West Conshohocken, PA, 2008, DOI: 10.1520/F2503-08, [www.astm.org](http://www.astm.org).





# **GENERAL DISCUSSION**

---

Cerebral (arterial) ischemic stroke is a major cause of disability and death in the world.<sup>1</sup> In ischemic stroke, an area of brain tissue suffers from a lack of blood supply due to blockage of the artery that supplies this area. In the equivalent ischemic disease of the heart, the coronary arteries surrounding and directly nourishing the heart are the major focus of imaging and treatment such as stenting and angioplasty.<sup>2</sup> In case of cerebral ischemic stroke, however, most attention is paid to the carotid arteries localized *outside* the brain instead of the arteries that locally supply blood to the brain.<sup>3</sup> Even though carotid artery pathology (atherosclerosis,

**“...striking that only recently attention has shifted towards pathology of the ‘coronary artery equivalents’ of the brain: the intracranial arteries...”**

arterial dissection) has proven its role in the occurrence of ischemic stroke, it is striking that only recently attention has shifted towards pathology of the ‘coronary artery equivalents’ of the brain: the intracranial arteries. The

apparent undervaluation of the intracranial arteries may be explained by, first, the absence – until a few years ago – of imaging techniques directly visualizing intracranial vessel wall pathology and, second, the lack of therapeutic techniques other than standard medical therapy for treatment of intracranial vessel wall pathology.

In recent years, substantial progress has been made within the field of intracranial vessel wall MR imaging, primarily using (ultra)high field strengths (3T and 7T), where a variety of sequences have been developed and applied in a diverse group of patients.<sup>4-14</sup> Initially, visualizing the intracranial vessel wall itself was one of the major goals, but with continued developments, several attempts have already been made to characterize intracranial (atherosclerotic) lesions.<sup>15-22</sup> This led to promising results like differentiating self-limiting diseases such as reversible vasoconstriction syndrome from therapy-requiring diseases such as vasculitis.<sup>23, 24</sup> When continuing along this track, the ultimate goal would be personalized medicine, with a reliable diagnosis and dedicated treatment of the individual patient presenting with a (transient) ischemic event: 1. defining the underlying cause of the ischemic event (e.g., atherosclerosis, vasculitis); 2. identifying the specific lesion that has caused the ischemic event (intra- or extracranial, lesion location); 3. dedicated treatment of the culprit lesion (and any other vulnerable lesion with a risk of recurrent ischemia); and 4. preventing recurrent (transient) ischemic events with early medical therapy or preventive endovascular treatment.

But, although promising results in the direction of this goal have been shown, several topics need to be addressed if the current progress within this research field is to lead to implementation of intracranial vessel wall imaging in clinical practice.

### Validation of vessel wall imaging techniques

As described above, several research groups have shown promising results in imaging vessel wall lesions within different patient groups, imaging plaque characteristics, and differentiating vasculitis from other vessel wall pathology.<sup>4-24</sup> The diagnosis of these vessel wall lesions is based on the assumption that (focal) thickening as seen on the intracranial vessel wall sequences reflects vessel wall pathology in the same way that focal carotid artery thickening represents atherosclerotic plaque, especially when the lesions are present within a symptomatic vascular territory. However, when we use this definition, a striking amount of patients has one or more of these lesions, as can be seen in **Chapter 2**.<sup>25</sup> Several questions then arise, like what is the nature of these lesions? Are they indeed atherosclerotic plaques, and, if so, in a vulnerable state? What imaging characteristics enable us to differentiate between different kinds of vessel wall pathology? And, equally important, what is normal healthy vessel wall, and what does normal aging of the vessel wall look like on MRI? In other words, we do not know whether what we believe to be vessel wall lesions, or even specifically atherosclerotic plaques, are truly lesions. An important next step in the field of intracranial vessel wall MR imaging is, thus, the validation of imaging sequences with histology (gold standard).

Some studies have made first steps to validate intracranial vessel wall pathology; however, these studies have either used a low field strength (1.5T)<sup>26</sup> – without the advantage of higher SNR and therefore higher spatial resolution – or MRI sequences with an ultrahigh spatial resolution<sup>27</sup> and long scan times (**Chapter 5**), prohibiting the use of these sequences in clinical practice. Although of low spatial resolution (1.5T) or not clinically applicable due to long scan times (7T), these studies, comparing MRI with histology, do provide qualitative evidence that (ultra high-field) MRI has the image contrast to visualize vessel wall thickening and heterogeneity corresponding with different atherosclerotic plaque components (**Chapter 5**). Future studies should focus on validating commonly used *in vivo* intracranial vessel wall sequences, preferably using both *in vivo* MR imaging in patients as well as *ex vivo* imaging of vessel wall segments of these same patients (when deceased). In addition, the development of quantitative plaque analysis, characterizing plaque components (and plaque vulnerability) based on their  $T_1$ -, PD-,  $T_2$ -, and  $T_2^*$  values, may prove to be of value in the development of standardized descriptions of these components on MR images.

### International collaboration

In the last decade, literature has shown intracranial vessel wall studies of research groups from several different countries, using different MR sequences, different

field strengths, and investigating different populations.<sup>4-24</sup> In most of these studies, patient groups were relatively small, making it difficult to state firm, statistically significant conclusions. Especially for intracranial vessel wall diseases that are not very common but therapeutically important, like vasculitis, including a large enough sample size is often difficult within a reasonable inclusion time. Also, most studies tend to emphasize unique or striking vessel wall pathology, while the healthy intracranial vessel wall characteristics and common lesions seem to be undervalued.

Like in many therapeutic trials, international collaboration between different intracranial vessel wall MR research groups would have several advantages. First, patient recruitment in several research hospitals would enable examinations on large, more homogeneous study groups (e.g., proven vasculitis only, (probable)

atherosclerosis only). For instance, in four years only 70 patients have been included in the 7T intracranial vessel wall imaging (IVI) study (**General introduction, Chapter 2, Chapter 3, Chapter 4**); if more than one medical center had been involved, many

**“...international collaboration between different intracranial vessel wall MR research groups would have several advantages...”**

more patients could have been included, with potentially different etiologies, which would have increased the power of the study. Second, exchanging MR sequences and imaging experience may ultimately lead to a small standardized subset of MR sequences that prove to be best in visualizing intracranial vessel wall pathology, and have been validated with histology. These sequences can then be used in large multicenter studies. Third, although perhaps still for the distant future, experienced researchers and clinical specialists (neurologists, neuroradiologists) would be able to combine their expertise to create recommendations for intracranial vessel wall imaging in clinical practice, and give suggestions and directions for interpreting intracranial vessel wall images, and for defining the relevance of these findings with regard to diagnosis and treatment.

### **Technical developments**

In **Chapter 2**, the first intracranial vessel wall sequence at 7T MRI was developed and tested in healthy volunteers and patients with ischemic stroke or TIA of the anterior cerebral circulation.<sup>25</sup> It was able to image both healthy intracranial vessel wall and vessel wall lesions with clear contrast between vessel wall, blood and cerebrospinal fluid. However, its disadvantages were the small coverage and the single contrast weighting ( $T_1$ -weighting), prohibiting both evaluation of more distal intracranial arteries as well as lesion characterization using multiple contrast weightings.

Therefore, new MR sequences with whole-brain coverage and three different image contrast weightings (PD-,  $T_1$ - and  $T_2$ -weighted) were developed (**Chapter 3**).<sup>28</sup> The whole-brain coverage made it possible to image both the proximal large arteries of the circle of Willis as well as their smaller, more distally located branches, which is an advantage over most 3T sequences. This enabled the presentation of an overview of predilection locations for intracranial vessel wall lesions (**Chapter 4**).

However, these 7T studies also showed that it is questionable whether the current spatial resolution of  $0.8 \times 0.8 \times 0.8 \text{ mm}^3$ , albeit enough for visualizing vessel wall lesions, is high enough to differentiate different plaque components within these individual lesions. A higher spatial resolution would increase the already long scan time; however, development of dedicated small-coverage sequences with different image contrast weightings, targeted to one or more specific vessel wall lesions, may enable better characterization of these lesions. Second, due to the long scan duration (approximately 10 minutes), a clinical protocol consisting of more than two image contrast weightings is not feasible; this also holds true for the current 3T sequences. Faster scanning, depending on the technical developments of the used MR scanners, would enable the use of more than one vessel wall sequence alongside standard clinically used imaging sequences, like FLAIR and TOF-MRA, making clinical implementation more feasible. Regarding spatial resolution, current 3T MR sequences have a slightly higher spatial resolution (ranging from  $0.25 \times 0.25 \times 2 \text{ mm}^3$  to  $0.8 \times 0.8 \times 3 \text{ mm}^3$ )<sup>4-24</sup> than the discussed 7T sequences. However, all except three<sup>16, 19, 20</sup> have a small field-of-view, limiting their use to imaging vessel wall lesions already seen on MRA. Also, cerebrospinal fluid suppression is still difficult at a 3T field strength, decreasing conspicuousness of the arterial outer wall.

Taking the discussed advantages and disadvantages of the different intracranial vessel wall sequences at different field strengths together, several technical developments may further improve vessel wall imaging at both field strengths. For instance, developing a robust whole-brain coverage 3T sequence (preferably  $T_1$ -weighted for possible enhancement) may enable screening of patients for intracranial vessel wall lesions anywhere in the cerebral arterial tree, and robust cerebrospinal fluid suppression may improve lesion conspicuousness. Then, the dedicated small-coverage sequences with different image contrast weightings could be used to characterize specific lesions seen on the whole-brain images. This improvement can also be implemented at 7T, by translation of the dedicated

**“...enable the development of intracranial vessel wall sequences with ‘new’ image contrasts...”**

3T small-coverage sequences to ultrahigh field strength. With these sequences, it may be possible to identify the vulnerable plaque at risk of causing subsequent ischemic events, and characterize vessel wall lesions other than atherosclerosis.

These developments could decrease differences between 3T and 7T intracranial vessel wall imaging, and, since 7T MRI is not yet clinically implemented and vastly outnumbered by 3T MR platforms, vessel wall imaging at 3T may become first choice in clinical practice. However, the advantages of ultrahigh-field MRI (**Chapter 1**), like increased magnetic susceptibility, enable the development of intracranial vessel wall sequences with 'new' image contrasts, like phase imaging or dedicated  $T_2^*$ -weighted sequences, for instance for identifying blood products within plaques.<sup>29</sup> Also, a higher spatial resolution can ultimately be achieved at 7T. These advantages then enable careful selection of a subgroup of patients for whom this increased spatial resolution and lesion conspicuousness at 7T proves to have additional value over the currently used 3T intracranial vessel wall sequences. A challenge for this type of sequences at 7T might be to generate black blood versions, or to achieve sufficient contrast between lumen and vessel wall, due to the current lack of a body transmit RF coil at 7T for non-selective inversion of the blood signal.

A major disadvantage of 7T intracranial vessel wall MRI – and, in fact, of all 7T imaging (**Chapter 1**) – is the large number of contraindications related to RF heating of metallic implants. In **Chapter 6**, it was shown that tissue loading and energy losses, quantified by the Q factor, play a dominant role in mitigating the risk of heating of metallic implants at 7T. These results were supported by a phantom experiment with 20 tested peripheral arterial stents in a worst-case scenario, showing no RF heating above safety limits. Although the conclusion of this study was focused on the fact that 20 commonly used metallic peripheral arterial stents proved to be MR compatible at 7T when embedded in tissue, the results also tentatively suggest that not only the 20 tested peripheral arterial stents, but *no* metallic implants, of whatever length, will cause significant (injury-causing) heating due to the RF field at 7T *when embedded in tissue*. This fundamental understanding would not only enable more diverse patient studies – e.g., including patients with a history of surgery or (endo)vascular intervention – but it is also mandatory for future safety guidelines regarding the use of 7T in the regular clinical setting, for instance in the case of intracranial vessel wall pathology.

## Conclusion

Intracranial vessel wall MRI has shown considerable progress within a relatively short period of time. It is a rapidly growing field, in which much work is still to be done, like validation of intracranial vessel wall sequences, joint effort and collaboration

of the international community, and the realization of larger, more homogeneous patient studies. However, when following this course, implementation of these promising techniques may be achieved in clinical practice before long, ultimately enabling personalized diagnosis and treatment of the individual patient with intracranial vessel wall disease.

### **FOR FUTURE RESEARCH**

- » Validation of intracranial vessel wall sequences with histology
  - What is normal / healthy (aging)?
  - Imaging characteristics per disease
- » Collaboration between research groups
  - Enables larger, more homogeneous patient groups
  - Consensus regarding vessel wall imaging techniques
  - Expert platform
- » Clinical implementation
  - 3T versus 7T → each can have its own role
  - Specific patient groups?
  - Implementing in diagnostic workup & treatment planning

## REFERENCE LIST

- (1) Go AS, Mozaffarian D, Roger VL et al. Heart disease and stroke statistics--2013 update: a report from the American Heart Association. *Circulation* 2013;127(1):e6-e245.
- (2) Anderson JL, Adams CD, Antman EM et al. 2011 ACCF/AHA focused update incorporated into the ACC/AHA 2007 guidelines for the management of patients with unstable angina/non-ST-elevation myocardial infarction: a report of the American College of Cardiology Foundation/American Heart Association task force on practice guidelines. *Circulation* 2011;123(18):e426-e579.
- (3) Furie KL, Kasner SE, Adams RJ et al. Guidelines for the prevention of stroke in patients with stroke or transient ischemic attack: a guideline for healthcare professionals from the American Heart Association/American Stroke Association. *Stroke* 2011;42(1):227-76.
- (4) Niizuma K, Shimizu H, Takada S, Tominaga T. Middle cerebral artery plaque imaging using 3-tesla high-resolution MRI. *J Clin Neurosci* 2008;15(10):1137-41.
- (5) Swartz RH, Bhuta SS, Farb RI et al. Intracranial arterial wall imaging using high-resolution 3-tesla contrast-enhanced MRI. *Neurology* 2009;72(7):627-34.
- (6) Ryu CW, Jahng GH, Kim EJ, Choi WS, Yang DM. High resolution wall and lumen MRI of the middle cerebral arteries at 3 tesla. *Cerebrovasc Dis* 2009;27(5):433-42.
- (7) Ma N, Jiang WJ, Lou X et al. Arterial remodeling of advanced basilar atherosclerosis: a 3-tesla MRI study. *Neurology* 2010;75(3):253-8.
- (8) Xu WH, Li ML, Gao S et al. In vivo high-resolution MR imaging of symptomatic and asymptomatic middle cerebral artery atherosclerotic stenosis. *Atherosclerosis* 2010;212(2):507-11.
- (9) Vergouwen MD, Silver FL, Mandell DM, Mikulis DJ, Swartz RH. Eccentric narrowing and enhancement of symptomatic middle cerebral artery stenoses in patients with recent ischemic stroke. *Arch Neurol* 2011;68(3):338-42.
- (10) Qiao Y, Steinman DA, Qin Q et al. Intracranial arterial wall imaging using three-dimensional high isotropic resolution black blood MRI at 3.0 tesla. *J Magn Reson Imaging* 2011;34(1):22-30.
- (11) Chung GH, Kwak HS, Hwang SB, Jin GY. High resolution MR imaging in patients with symptomatic middle cerebral artery stenosis. *Eur J Radiol* 2012;81(12):4069-74.
- (12) Shi M, Wang S, Zhou H, Cheng Y, Feng J, Wu J. Wingspan stenting of symptomatic middle cerebral artery stenosis and perioperative evaluation using high-resolution 3 tesla MRI. *J Clin Neurosci* 2012;19(6):912-4.
- (13) Kim JM, Jung KH, Sohn CH, Moon J, Han MH, Roh JK. Middle cerebral artery plaque and prediction of the infarction pattern. *Arch Neurol* 2012;69(11):1470-5.
- (14) Lou X, Ma N, Ma L, Jiang WJ. Contrast-enhanced 3T high-resolution MR imaging in symptomatic atherosclerotic basilar artery stenosis. *AJNR Am J Neuroradiol* 2013;34(3):513-7.
- (15) Skarpathiotakis M, Mandell DM, Swartz RH, Tomlinson G, Mikulis DJ. Intracranial atherosclerotic plaque enhancement in patients with ischemic stroke. *AJNR Am J Neuroradiol* 2013;34(2):299-304.
- (16) Turan TN, Bonilha L, Morgan PS, Adams RJ, Chimowitz MI. Intraplaque hemorrhage in symptomatic intracranial atherosclerotic disease. *J Neuroimaging* 2011;21(2):e159-e161.

- (17) Park JK, Kim SH, Kim BS, Choi G, Jeong SY, Choi JC. Imaging of intracranial plaques with black-blood double inversion recovery MR imaging and CT. *J Neuroimaging* 2011;21(2):e64-e68.
- (18) Chung JW, Kim BJ, Choi BS et al. High-resolution magnetic resonance imaging reveals hidden etiologies of symptomatic vertebral arterial lesions. *J Stroke Cerebrovasc Dis* 2014;23(2):293-302.
- (19) Natori T, Sasaki M, Miyoshi M et al. Evaluating middle cerebral artery atherosclerotic lesions in acute ischemic stroke using magnetic resonance T1-weighted 3-dimensional vessel wall imaging. *J Stroke Cerebrovasc Dis*, published online before print July 18, 2013; doi: 10.1016/j.jstrokecerebrovasdis.2013.06.025.
- (20) Turan TN, Rumboldt Z, Brown TR. High-resolution MRI of basilar atherosclerosis: three-dimensional acquisition and FLAIR sequences. *Brain Behav* 2013;3(1):1-3.
- (21) Mi Kim S, Ryu CW, Jahng GH, Jong KE, Suk CW. Two different morphologies of chronic unilateral middle cerebral artery occlusion: evaluation using high-resolution MRI. *J Neuroimaging*, published online before print January 16, 2013; doi: 10.1111/jon.12009.
- (22) Zhu XJ, Du B, Lou X et al. Morphologic characteristics of atherosclerotic middle cerebral arteries on 3T high-resolution MRI. *AJNR Am J Neuroradiol* 2013;34(9):1717-22.
- (23) Mandell DM, Matouk CC, Farb RI et al. Vessel wall MRI to differentiate between reversible cerebral vasoconstriction syndrome and central nervous system vasculitis: preliminary results. *Stroke* 2012;43(3):860-2.
- (24) Pfefferkorn T, Linn J, Habs M et al. Black blood MRI in suspected large artery primary angiitis of the central nervous system. *J Neuroimaging* 2013;23(3):379-83.
- (25) van der Kolk AG, Zwanenburg JJ, Brundel M et al. Intracranial vessel wall imaging at 7.0-T MRI. *Stroke* 2011;42(9):2478-84.
- (26) Chen XY, Lam WW, Ng HK, Zhao HL, Wong KS. Diagnostic accuracy of MRI for middle cerebral artery stenosis: a postmortem study. *J Neuroimaging* 2006;16(4):318-22.
- (27) Majidi S, Sein J, Watanabe M et al. Intracranial-derived atherosclerosis assessment: an in vitro comparison between virtual histology by intravascular ultrasonography, 7T MRI, and histopathologic findings. *AJNR Am J Neuroradiol* 2013;34(12):2259-64.
- (28) van der Kolk AG, Hendrikse J, Brundel M et al. Multi-sequence whole-brain intracranial vessel wall imaging at 7.0 tesla. *Eur Radiol* 2013;23(11):2996-3004.
- (29) Kim TW, Choi HS, Koo J et al. Intramural hematoma detection by susceptibility-weighted imaging in intracranial vertebral artery dissection. *Cerebrovasc Dis* 2013;36(4):292-8.



# **SUMMARY**

---



Intracranial atherosclerosis is one of the main causes of cerebral ischemic events. Current conventional imaging techniques assessing intracranial arterial disease *in vivo* only visualize the vessel wall lumen instead of the pathological vessel wall itself. Therefore, not much is known about the prevalence and imaging characteristics of intracranial vessel wall pathology (like atherosclerosis) *in vivo*, and distinguishing different vessel wall pathologies remains difficult. Visualizing the intracranial vessel wall is challenging, as the vessels are small and do not have a single orientation.

This thesis describes the development of several 7 tesla (T) magnetic resonance imaging (MRI) sequences specifically designed to visualize the intracranial arterial vessel wall *in vivo*. Preliminary studies on healthy volunteers show the ability of the developed sequences to image healthy intracranial arterial vessel walls. Subsequent studies on patients with ischemic stroke or transient ischemic attack (TIA) show successful visualization of intracranial vessel wall lesions as well. In the majority of patients, one or more vessel wall lesions are found on MR imaging, of which  $\frac{3}{4}$  cannot be seen on conventional imaging, and would therefore have been missed without the use of these dedicated MRI sequences. Most lesions are found in the distal internal carotid artery, as well as the M1- and M2 segment of the middle cerebral artery, and do not change over time (1 month), possibly reflecting a more generalized atherosclerotic process.

Currently the main atherosclerotic culprit lesion is thought to be the 'vulnerable' atherosclerotic plaque: a plaque with specific characteristics like a lipid-rich necrotic core and intraplaque hemorrhage. For the extracranial carotid artery, validation studies have determined specific *in vivo* image contrast characteristics for plaque characterization. However, it is not known whether MRI has the image contrast necessary to image intracranial plaque components as well. In this thesis, in an *ex vivo* setting ultrahigh-resolution 7T MRI sequences were indeed able to distinguish areas of different signal intensities that spatially corresponded to plaque components within advanced atherosclerotic plaques, paving the way towards characterization of *in vivo* intracranial vessel wall lesions.

Although 7T MRI has several advantages over imaging on lower field strengths – like an increased signal-to-noise ratio, enabling imaging at higher spatial resolution, with isotropic voxels – a major drawback are the strict safety rules regarding metallic implants, which are based on conflicting results of RF heating of implants at different field strengths. In this thesis, fundamental experiments were performed at 7T, explaining the discrepancies of RF heating at different field strengths; further, 20 peripheral arterial stents were tested and found MR compatible for 7T MRI.

Intracranial vessel wall MRI has shown considerable progress within the last few years. Much work is still to be done, like validation of vessel wall sequences, collaboration of the international community, and realization of larger patient studies. However, when following this course, implementation of these techniques in clinical practice may be achieved in near future.



# NEDERLANDSE SAMENVATTING

---



Intracraniale atherosclerose is een van de meest voorkomende oorzaken van (tijdelijke) cerebrale ischemie. De huidige conventionele technieken voor *in vivo* visualisatie van ziekten van de intracraniale arteriële vaatwand brengen het lumen van de vaatwand in beeld, in plaats van de pathologische vaatwand zelf. Er is hierdoor weinig bekend over de *in vivo* prevalentie en de beeldkarakteristieken van pathologie van de intracraniale vaatwand (zoals atherosclerose), waardoor een onderscheid tussen verschillende vaatwandziekten moeilijk te maken is. Het goed in beeld brengen van de intracraniale vaatwand is een uitdaging, omdat de vaten klein zijn en niet in één richting zijn georiënteerd.

Dit proefschrift beschrijft de ontwikkeling van enkele 7 tesla (T)-MRI-sequenties, ontworpen om *in vivo* specifiek de intracraniale arteriële vaatwand in beeld te brengen. Initiële studies met gezonde vrijwilligers laten zien dat de ontwikkelde sequenties in staat zijn de gezonde intracraniale arteriële vaatwanden in beeld te brengen. Vervolgstudies met patiënten met (tijdelijke) cerebrale ischemie tonen aan dat de sequenties tevens succesvol zijn in het in beeld brengen van laesies van de intracraniale vaatwand. Bij het merendeel van de patiënten worden één of meer vaatwandlaesies gevonden, waarvan drie kwart niet op conventionele beeldvorming terug te zien is. De laesies worden met name gezien in de distale a. carotis interna en in het M1- en M2-segment van de a. cerebri media, en blijken bij controle (na 1 maand) niet in aspect te veranderen.

Tegenwoordig ziet men de ‘vulnerable’ atherosclerotische plaque - met lipiderijke necrotische kern en intraplaque-bloedingen - als belangrijkste veroorzaker van (voorbijgaande) ischemie. In het verleden zijn voor de extracraniale a. carotis meerdere studies verricht voor plaquekarakterisatie, waarbij *in vivo* beeldcontrastkenmerken op MRI werden gevalideerd met plaquecomponenten in histologische coupes. Het is echter niet bekend of MRI beschikt over voldoende beeldcontrast om ook intracraniale plaquecomponenten te karakteriseren. In dit proefschrift wordt bevestigd dat 7T-MRI gebieden met verschillende signaalintensiteiten kan onderscheiden die ruimtelijk overeenkomen met plaquecomponenten.

7T-MRI heeft meerdere voordelen boven beeldvorming op lagere veldsterkten, waaronder een grotere ‘signal-to-noise ratio’, waardoor met een hogere spatiële resolutie en isotrope voxels kan worden gescand. De strikte veiligheidsregels wat betreft metalen implantaten blijven echter een belangrijk nadeel. In dit proefschrift worden, aan de hand van fundamentele experimenten met 7T, het mechanisme van RF-opwarming op verschillende veldsterkten uitgelegd. Daarnaast worden 20 perifere arteriële stents getest en ‘MR compatible’ bevonden voor 7T-MRI.

MRI van de intracraniale vaatwanden heeft zich de afgelopen jaren sterk ontwikkeld. Er moet nog veel gebeuren, zoals validatie van vaatwandsequenties, internationale samenwerking, en het realiseren van studies met grotere patiëntengroepen. Wanneer deze ontwikkeling zich echter doorzet, kan implementatie van deze technieken in de klinische praktijk in de nabije toekomst werkelijkheid worden.



# **LIST OF PUBLICATIONS**

---

## PEER-REVIEWED PUBLICATIONS

Langdon W, Donahue M, **van der Kolk AG**, Rane S, Strother M. *Correlating hemodynamic MRI with high-field intracranial vessel wall imaging in stroke.*

Accepted in Journal of Radiology Case Reports.

Dieleman N, **van der Kolk AG**, Zwanenburg JJM, Hartevelde AA, Biessels GJ, Luijten PR, Hendrikse J. *Imaging intracranial vessel wall pathology using MRI: current prospects and future directions.*

Accepted in *Circulation*.

Truijman MTB, Kooi ME, van Dijk AC, de Rotte AAJ, **van der Kolk AG**, Liem MI, Schreuder FH, Boersman H, Mess WH, van Oostenbrugge RJ, Koudstaal PJ, Kappelle LJ, Nederkoorn PJ, Nederveen AJ, Hendrikse J, van der Steen AFW, Daemen MJAP, van der Lugt A. *PARISK (Plaque At RISK): Prospective multicenter study for diagnosis efficacy for high risk plaque and stroke.*

International Journal of Stroke 2013 Oct; doi: 10.1111/ijvs.12167 (Epub ahead of print).

**van der Kolk AG**, Zwanenburg JJM, Brundel M, Biessels GJ, Smit EJ, Visser F, Luijten PR, Hendrikse J. *Multi-sequence whole-brain intracranial vessel wall imaging at 7.0 tesla.* Eur Radiol 2013;23(11):2996-3004.

**van der Kolk AG**, Hendrikse J, Zwanenburg JJ, Visser F, Luijten PR. *Clinical applications of 7T MRI in the brain.*

Eur J Radiol 2013;82(5):708-18.

**van der Kolk AG**, Zwanenburg JJ, Brundel M, Biessels GJ, Visser F, Luijten PR, Hendrikse J. *Intracranial vessel wall imaging at 7.0-T MRI.*

Stroke 2011;42(9):2478-84.

**van der Kolk AG**, de Borst GJ, Jongen LM, den Hartog AG, Moll FL, Mali WPTHM, Hendrikse J. *Prevalence and clinical consequences of carotid artery residual defects following endarterectomy: a prospective CT angiography evaluation study.*

Eur J Vasc Endovasc Surg 2011;42(2):144-52.

**van der Kolk AG**, de Borst GJ, den Hartog AG, Kooi ME, Mali WP, Hendrikse J. *Hyperintense carotid plaque on T<sub>1</sub>-weighted turbo-field echo MRI in symptomatic patients with low-grade carotid stenosis and carotid occlusion.*

Cerebrovasc Dis 2010; 30(3): 221-9.

### NON-PEER REVIEWED PUBLICATIONS

**van der Kolk AG**, Hendrikse J, Zwanenburg JJM. *7.0 Tesla MRI van het brein: modeverschijnsel of toekomstperspectief?*  
Neuropraxis 2013;17(2):35-47

Geurts M, **van der Kolk AG**, Vergouwen MDI. *Uw diagnose: 'Crescendo Transient Aura Attacks'.*  
Tijdschr Neurol en Neurochir 2012;113:133-4.

### BOOK CHAPTERS

Zwanenburg JJM, **van der Kolk AG**, Luijten PR. *Ultra-high-field MR imaging: research tool or clinical need?*  
PET Clinics 2013;8(3):311-328.

**van der Kolk AG**, Hendrikse J, Luijten PR. *Ultrahigh-field magnetic resonance imaging: the clinical potential for anatomy, pathogenesis, diagnosis and treatment planning in brain disease.*  
Neuroimaging Clin N Am 2012;22(2):343-62.

### SUBMITTED MANUSCRIPTS

Brundel M, **van der Kolk AG**, Heringa SM, Luijten PR, Kappelle LJ, Hendrikse J, Biessels GJ. *Cerebral microbleeds at ultra-high field 7T MRI are not related to cognition in patients with a TIA or ischemic stroke.*

Nobel JM, **van der Kolk AG**, Zwanenburg JJM, Visser F, Luijten PR, Hendrikse J. *Clinical value of fluid-attenuated inversion recovery (FLAIR) at 7.0 tesla MRI: A comparison with clinical FLAIR imaging in patients with cerebrovascular disease.*

Suchá D, **van der Kolk AG**, Brundel M, Biessels GJ, Luijten PR, Hendrikse J. *Blood-brain-barrier leakage on 7.0 tesla MRI in patients after transient ischemic attack and stroke.*

Dieleman N, **van der Kolk AG**, van Veluw SJ, Frijns CJM, Harteveld AA, Luijten PR, Hendrikse J. *Combining intracranial vessel wall MRI and (micro)infarct assessment to differentiate between ischemic stroke etiologies in young adult stroke patients using 7.0 tesla.*

Harteveld AA, De Cocker LJJ, Dieleman N, **van der Kolk AG**, Zwanenburg JJM, Robe PAJ, Luijten PR, Hendrikse J. *High-resolution contrast-enhanced time-of-flight magnetic resonance angiography of intracranial perforators at 7.0 tesla.*

de Rotte AAJ, **van der Kolk AG**, Rutgers D, Zelissen PMJ, Visser F, Luijten PR, Hendrikse J. *Feasibility of high-resolution pituitary MRI at 7.0 tesla.*

**van der Kolk AG**, Ansems J, Kroeze H, van den Berg CAT, de Borst GJ, Luijten PR, Webb AG, Renema WKJ, Klomp DWJ. *No safety risk in radiofrequency heating of 20 metallic peripheral arterial stents embedded within tissue for MRI studies at 7 tesla.*

**van der Kolk AG**, Zwanenburg JJM, Denswil NP, Vink A, Spliet WGM, Daemen MJAP, Visser F, Klomp DWJ, Luijten PR, Hendrikse J. *Imaging the intracranial atherosclerotic vessel wall using 7.0 tesla MRI: initial comparison with histopathology.*

### **CONFERENCE PRESENTATIONS (FIRST AUTHOR ONLY)**

**van der Kolk AG**, Zwanenburg JJM, Brundel M, et al. *Natural course of intracranial vessel wall lesions in stroke- and TIA patients at 7.0 tesla MRI.*

Oral presentation at the 21st ISMRM Annual Meeting & Exhibition 2013, Salt Lake City, UT, USA. ISMRM magna cum laude merit award

**van der Kolk AG**, Zwanenburg JJM, Denswil NP, et al. *Ultrahigh-resolution 0.11 x 0.11 mm MR imaging of the intracranial atherosclerotic vessel wall at 7.0 tesla.*

Poster presentation at the 21st ISMRM Annual Meeting & Exhibition 2013, Salt Lake City, UT, USA

**van der Kolk AG**, Hendrikse J, Brundel M, et al. *Multisequence whole-brain intracranial vessel wall imaging at 7.0 tesla MRI.*

Poster presentation at the 21st ISMRM Annual Meeting & Exhibition 2013, Salt Lake City, UT, USA

**van der Kolk AG**. *MR imaging of intracranial atherosclerosis.*

Invited lecture at the 21st European Stroke Conference 2012, Lisbon, Portugal

**van der Kolk AG**, Nobel JM, Zwanenburg JJM, et al. *Clinical value of fluid-attenuated inversion recovery (FLAIR) at 7.0 tesla MRI: a comparison with 1.5 tesla FLAIR imaging in patients with cerebrovascular disease.*

Poster presentation at the 20th ISMRM Annual Meeting & Exhibition 2012, Melbourne, Australia

**van der Kolk AG, Zwanenburg JJM, Visser F, et al. *Clinical applications of ultrahigh-field MR imaging in brain disease.***

Printed Education Exhibit at the 50th Annual Meeting & The Foundation of the ASNR Symposium 2012, New York, USA

**van der Kolk AG. *7 tesla MRI of the brain.***

*Invited lecture at the 1<sup>st</sup> Dutch 7<sup>+</sup> Tesla Day (VISTA++) 2011, Leiden, the Netherlands*

**van der Kolk AG, Zwanenburg JJM, Brundel M, et al. *Multisequence 7T MRI of the intracranial vessel wall.***

Poster presentation at the 5th International Conference on Intracranial Atherosclerosis (ICAS) 2011, Valladolid, Spain

**van der Kolk AG, Zwanenburg JJM, Brundel M, et al. *Intracranial vessel wall imaging (with MPR-TSE) at 7.0 tesla (MRI) in ischemic stroke and TIA patients.***

Oral presentation at the 5th International Conference on Intracranial Atherosclerosis (ICAS) 2011, Valladolid, Spain

- Oral presentation at the 16th national conference of the Radiological Society of the Netherlands 2011, Maastricht, the Netherlands
- Poster presentation at the 20th European Stroke Conference (ESC) 2011, Hamburg, Germany
- Poster presentation at the 19th ISMRM Annual Meeting & Exhibition 2011, Montreal, Canada
- Poster presentation at the 3rd Annual Meeting of the ISMRM Benelux Chapter 2011, Hoeven, the Netherlands

**van der Kolk AG, Zwanenburg JJM, Visser F, et al. *Future clinical applications of high resolution anatomical imaging of the brain at 7.0 tesla MRI.***

- Oral educational presentation at the 16th national conference of the Radiological Society of the Netherlands 2011, Maastricht, the Netherlands
- Educational poster presentation at the 19th ISMRM Annual Meeting & Exhibition 2011, Montreal, Canada

**van der Kolk AG, de Borst GJ, Jongen LM, et al. *Prevalence and clinical consequences of carotid artery residual defects following endarterectomy: a prospective CT angiography evaluation study.***

Oral presentation at the 15th national conference of the Radiological Society of the Netherlands 2010, Veldhoven, the Netherlands

**van der Kolk AG, Zwanenburg JJM, Visser F, et al. *Intracranial vessel wall imaging at 7.0 tesla MRI.***

Oral presentation at the 15<sup>th</sup> national conference of the Radiological Society of the Netherlands 2010, Veldhoven, the Netherlands

**van der Kolk AG, de Borst GJ, den Hartog AG, et al. *Hyperintense carotid plaque on T1-weighted turbo-field echo MRI in symptomatic patients with low-grade carotid stenosis and carotid occlusion.***

- Poster presentation at the 18th Annual Meeting & Exhibition 2010, Stockholm, Sweden
- Oral presentation at the 2nd Annual Meeting of the ISMRM Benelux Chapter 2010, Utrecht, the Netherlands
- Oral presentation at the 14th national conference of the Radiological Society of the Netherlands, Amsterdam, the Netherlands

**van der Kolk AG, Zwanenburg JJM, Biessels GJ, et al. *Ultra-high field MRI at 7.0 tesla in patients with ischemic or hemorrhagic stroke: a preliminary study.***

Poster presentation at the 18<sup>th</sup> Annual Meeting & Exhibition 2010, Stockholm, Sweden





**DANKWOORD**

---



Eigenlijk is het dankwoord het belangrijkste onderdeel van het proefschrift; niet zozeer omdat het goed is om de mensen die je op wat voor manier dan ook hebben bijgestaan, te bedanken, maar vooral omdat de kans groot is dat zeker de helft van de mensen die jouw proefschrift in handen krijgen (misschien jij wel...), niets anders zullen lezen dan dit dankwoord. Geef toe: je bladert éérst door naar het dankwoord ("*sta ik erin? en wie nog meer dan?*") voordat je zelfs maar aandacht aan het omslag besteedt ("*getuigt wel/niet van veel creativiteit*"), het aantal hoofdstukken ("*best veel, zou mij dat lukken?*"), het aantal pagina's ("*dun boekje hoor, niet echt een schrijver, altijd al gedacht...*"), hoeveel artikelen er in de 'List of Publications' staan ("*12... uitslover, less is more, sukkel!*"), en ook als je geen affiniteit hebt met het onderwerp blader je er toch even doorheen om te kijken of er leuke plaatjes in staan (uiteraard in deze volgorde). Optimistisch als ik ben denk ik niet dat dit een gebrek aan interesse bij jou is, maar voortkomt uit een drang naar bevestiging dat je ertoe doet, die mij – ik geef het direct toe – niet vreemd is.

Maar ja, nu ik dus aan het dankwoord ben begonnen, blijkt dat nog lang niet mee te vallen... Als ervaringsdeskundige weet ik dus waar je als eerste naar kijkt: word ik überhaupt genoemd? En zo ja, op welke manier dan? In hoeverre wordt er over andere mensen die ik ken, of niet ken ("*wie zou dat zijn?*") met meer of minder lovende woorden gesproken? Hier zit mij als schrijver dan toch iets dwars: want als ik al schrijvend nou eens veel meer, of meer bijzonders, over jou (of de ander) zeg dan over de ander (of jou); vind jij (of de ander) dat dan erg? Zou jij (of de ander) denken dat ik daar iets mee bedoel? Voor ik het weet ga ik mijn woorden op een goudschaaltje wegen, en je weet dat dat niet mijn sterkste punt is... weg spontaniteit! Dat is dus niet de manier waarop ik dit dankwoord vorm wil geven...

Een oplossing zou zijn om niemand bij naam te noemen. Wat een rust: ik kan niemand per ongeluk vergeten, en ik stuit niemand onbedoeld tegen de borst... Alleen gaat dat ook niet echt werken, want jij had verwacht in ieder geval je naam te zien, en legt nu met een teleurgesteld gezicht mijn proefschrift terzijde (of gooit het weg, maar daar denk ik liever niet over na). Een andere oplossing is om voor iedereen een apart dankwoord te schrijven, zodat iedereen een persoonlijk proefschrift met eigen dankwoord krijgt. Hoewel het idee me lange tijd heeft aangesproken (je kent mij, tijd en geld spelen geen rol, en het vooruitzicht om jullie elkaar de exemplaren uit handen te zien rukken uit nieuwsgierigheid naar elkaars persoonlijke dankwoord sprak me erg aan), gaat me dat toch te ver. De enige oplossing die overblijft zie je op de volgende pagina. Het is even zoeken, maar je staat er vast tussen...

Dankjewel voor het er zijn (op wat voor manier dan ook) tijdens mijn promotietijd.







# **BIOGRAPHY**

---



The author of this thesis, Anja Gwendolyn van der Kolk, was born November 4th, 1984 in Wageningen, the Netherlands. Following Montessori primary school in Rhenen and three years at the 'IVO-Montessorischool' in Oosterbeek, she graduated from high school in 2002 at the 'Regionale Scholengemeenschap Pantarijn' in Wageningen. She then began her medical training at Utrecht University, and obtained her medical degree in 2008, after which she accepted a PhD position within the department of Radiology of the University Medical Center (UMCU) in Utrecht. She



worked there under the supervision of Dr. Jeroen Hendrikse, Dr. Jaco Zwanenburg, Prof. Willem Mali and Prof. Peter Luijten. Whilst at the UMCU she held a seat in the PhD Student Council Imago (part of Utrecht Graduate School of Life Sciences); she also coordinated scientific radiological internships for medical students, and chaired the ISMRM Benelux Organizing Committee 2012. In 2012 she worked on dynamic contrast-enhanced 7T MRI for two months with Dr. Manus Donahue, as a visiting research fellow at Vanderbilt University Institute of Imaging Science (VUIIS) at Vanderbilt University in Nashville, Tennessee, United States. In May 2013 she started her residency in Radiology at Gelre Ziekenhuizen Apeldoorn in the Netherlands, under the supervision of Dr. Jan Willem Gratama. She is currently chief resident in Gelre Ziekenhuizen, and at the same time holds a position at the UMCU as co-supervisor (together with Dr. Jeroen Hendrikse) of PhD students Anita Harteveld and Nikki Dieleman, continuing the long-term research project she initiated on intracranial atherosclerosis. She lives in Arnhem with her partner, Arno van Schuijlenborgh.

